Precision measurement of the CKM parameter sin(2β) with the LHCb experiment

Dissertation zur Erlangung des akademischen Grades
Dr. rer. nat.

vorgelegt von
Christophe Arnold Augustin Cauet
geboren am 13.02.1984
in Dortmund

Fakultät Physik
Technische Universität Dortmund

Dortmund, im August 2015

Der Fakultät Physik der Technischen Universität Dortmund zur Erlangung des akademischen Grades eines Doktors der Naturwissenschaften vorgelegte Dissertation.

Datum der mündlichen Prüfung: 16. Oktober 2015

1. Gutachter: Prof. Dr. Bernhard Spaan
2. Gutachter: Prof. Dr. Kevin Kröninger
Vorsitzender der Prüfungskommission: Prof. Dr. Jan Kierfeld
Vertreter der wissenschaftlichen Mitarbeiter: Dr. Johannes Erdmann

Vorsitzender des Promotionsausschusses: Prof. Dr. Thomas Weis

Abstract

This thesis presents a decay-time dependent measurement of CP violation in the decay of B^0 and $\overline{B}^0$ mesons into their common $J/\psi K^0_S$ final state. The CP observables $S_{J/\psi K^0_S}$ and $C_{J/\psi K^0_S}$ allow access to the magnitude of the symmetry violation in the interference between the B meson decay and mixing amplitudes and can directly be related to the CKM angle β. Using a dataset of selected signal $B^0 \to J/\psi K^0_S$ candidates corresponding to an integrated luminosity of $3.0\,\text{fb}^{-1}$ collected at centre-of-mass energies of 7 and 8 TeV by the LHCb experiment, the CP observables are measured to be

$$\begin{aligned} S_{J/\psi K^0_S} &= \quad 0.731 \pm 0.035\,(\text{stat}) \pm 0.020\,(\text{syst})\,, \text{ and} \\ C_{J/\psi K^0_S} &= -0.038 \pm 0.032\,(\text{stat}) \pm 0.005\,(\text{syst})\,, \end{aligned}$$

resulting in the worlds most precise measurement of these quantities at a hadron collider. With the parameter $C_{J/\psi K^0_S}$ fixed to zero, $S_{J/\psi K^0_S}$ equals $\sin(2\beta) = 0.746 \pm 0.030\,(\text{stat})$. The results have a similar precision as previous measurements at the B factories BaBar and Belle and are consistent with these and with expectations from measurements of other CKM matrix parameters.

Zusammenfassung

Die vorliegende Dissertation beschreibt eine zerfallszeitabhängige Messung von CP-Verletzung im Zerfall von B^0- und $\overline{B}^0$-Mesonen in ihren gemeinsamen Endzustand $J/\psi K^0_S$. Die Größe der Symmetrieverletzung in der Interferenz der Zerfalls- und Mischungs-Amplituden der B-Mesonen lässt sich durch die CP-Observablen $S_{J/\psi K^0_S}$ und $C_{J/\psi K^0_S}$ ausdrücken und mit dem CKM-Winkel β in Bezug setzen. Die Messung wurde auf einem Datensatz von selektierten $B^0 \to J/\psi K^0_S$ Signal-Kandidaten durchgeführt, der einer integrierten Luminosität von $3.0\,\text{fb}^{-1}$ entspricht und bei Schwerpunktsenergien von 7 und 8 TeV am LHCb-Experiment aufgenommen wurde. Mit

$$\begin{aligned} S_{J/\psi K^0_S} &= \quad 0.731 \pm 0.035\,(\text{stat}) \pm 0.020\,(\text{syst}) \text{ und} \\ C_{J/\psi K^0_S} &= -0.038 \pm 0.032\,(\text{stat}) \pm 0.005\,(\text{syst})\,, \end{aligned}$$

wurden die CP-Observablen mit einer Genauigkeit gemessen, die weltweit bisher an keinem anderen hadronischen Beschleuniger erreicht werden konnte. Unter der Annahme von $C_{J/\psi K^0_S} = 0$ folgt $S_{J/\psi K^0_S} = \sin(2\beta) = 0.746 \pm 0.030\,(\text{stat})$. Die Ergebnisse sind von ähnlicher Präzision wie bisherige Messungen an den B-Fabriken BaBar und Belle und sind bestens vereinbar mit diesen und Erwartungen aus Messungen von anderen CKM-Matrix-Parametern.

Contents

1 Introduction **1**

2 *CP* violation in the *B* meson system **5**
2.1 The Standard Model of Particle Physics 5
2.2 Flavour physics 6
2.2.1 The CKM quark mixing matrix 7
2.2.2 B meson decay 9
2.2.3 Oscillations of neutral B mesons 10
2.2.4 Time evolution of meson states 11
2.2.5 Classification of CP violating effects 12
2.3 CP violation in decays of $B^0 \to J/\psi K^0_S$ 13

3 The LHCb experiment **17**
3.1 The LHC and its experiments 17
3.2 The LHCb detector 19
3.3 Track reconstruction 21
3.3.1 The vertex locator 21
3.3.2 The LHCb tracking detectors 22
3.3.3 Track reconstruction technique and performance 23
3.4 Particle identification 24
3.4.1 The ring-imaging Cherenkov detectors 24
3.4.2 The calorimeter system 25
3.4.3 The muon system 26
3.4.4 Particle identification technique and performance 26
3.5 Trigger 27
3.5.1 The hardware trigger 28
3.5.2 The high level trigger 28
3.6 Software stack 28
3.7 Data taking 29

4 Flavour tagging **31**
4.1 Flavour tagging at BABAR and Belle 32
4.2 Flavour tagging algorithms 33
4.2.1 Opposite-side algorithms 34
4.2.2 Same-side algorithms 37
4.3 Calibration of the flavour tagging output 38
4.3.1 Methodology 39

4.3.2 Opposite-side tagger calibration using $B^+ \to J/\psi K^+$ decays 41
4.3.3 Same-side tagger calibration using $B^0 \to J/\psi K^{*0}$ decays . . 43
4.4 Combination of single tagger outputs 44
4.5 Recent developments and Run II 47

5 The measurement of sin(2β) 49
5.1 Overview of the measurement ingredients 49
5.2 Data preparation 49
5.2.1 Trigger 51
5.2.2 Stripping 54
5.2.3 Offline selection 54
5.2.4 Multiple candidates 59
5.2.5 MC and data samples 60
5.3 Flavour tagging 64
5.3.1 Performance 64
5.4 Backgrounds 65
5.4.1 Physics backgrounds 65
5.4.2 Background tagging asymmetries 66
5.5 Decay time resolution and acceptance 71
5.5.1 Resolution 71
5.5.2 Decay time acceptance 73
5.6 Likelihood fit 78
5.6.1 List of used probability density functions 79
5.6.2 Parametrisation of the fit model 81
5.6.3 Experimenter's bias 87
5.6.4 Fitter validation 87
5.7 Measurement of *CP* violation 88
5.7.1 Constrained parameters 89
5.7.2 Fixed parameters 90
5.7.3 Fit results 90
5.7.4 Kaon regeneration 96
5.8 Studies of systematic effects 96
5.8.1 Cross-checks 96
5.8.2 Systematics 102
5.8.3 Summary of systematic effects 106

6 Conclusion and outlook 109

Appendices

A Supplementary material to the measurement of sin(2β) 113
A.1 Decay time resolution and acceptance 113
A.1.1 Resolution 113

A.2 Measurement of CP violation 114
A.2.1 Tables of fixed parameters 114
A.2.2 Fit results of subordinate parameters 119
A.3 Studies of systematic effects 121

Bibliography **133**

Danksagung **143**

1 Introduction

With the Big Bang theory being the prevailing model to explain the earliest known period of the universe, matter and anti-matter should have been produced in equal quantities. To explain today's observation of a maximal asymmetry between matter and anti-matter with complete absence of anti-matter in the visible universe, the source of the asymmetry needs to be determined.

A possible solution was provided by Sakharov [1]. To achieve a universal baryon asymmetry three conditions have to be fulfilled: 1) the existence of baryon number violating processes, 2) the violation of C and CP conservation in fundamental interactions, and 3) a deviation from the thermal equilibrium during the history of the universe.

The non-equilibrium state is guaranteed due to the inflationary epoch of the universe and baryon number violation processes are known as well [2, 3], thus leaving us to find a source of CP violation large enough to explain the existing matter-antimatter asymmetry.

Discrete global symmetries play an outstanding role in the Standard Model of Particle Physics (SM). Of particular importance are the discrete transformations under charge conjugation C, parity P, and time reversal T. The CPT theorem states that the CPT symmetry holds for any Lorentz invariant, local quantum field theory, whereas the violation of each of the discrete symmetries C, P, or T is still possible [4].

Lee and Yang where the first to question the general assumption that all physical interactions are invariant even under a single transformation by stating a possible P violation in weak interactions [5]. Soon after, this statement was supported by the measurement of P violation in the β^- decay of ^{60}Co [6]. The experiment revealed that the weak interaction only couples to fermions with left-handed chirality or anti-fermions with right-handed chirality, which means that symmetry under the C transformation is violated as well. Still, the interaction seemed to behave invariant under combined CP transformations. But already in 1964, the symmetry violation under CP transformation was observed in the neutral kaon system and consequently established in the SM [7].

However, writing the source of CP violation into the theoretical description of the SM still was a challenge. The triumphant idea came from Makoto Kobayashi and Toshihide Maskawa proposing a third quark generation as a possibility to explain CP violation in the framework of the electroweak theory [8]. The discovery of the b quark [9] provided enough confidence in their theory to start planning the two B factories BaBar and Belle. At the two e^+e^- colliders, PEP-II (Stanford, CA, US) and KEKB (Tsukuba, JP), electrons and positrons were brought to

collisions at asymmetric beam energies. Both machines operated at centre-of-mass energies of exactly the $\Upsilon(4S)$ bottonium resonance at 10.58 GeV, producing $B\overline{B}$ meson pairs at high rates of 10^6 a day [10].

To establish *CP* violation in the SM it was necessary to extend the measurements outside the kaon sector to the heavier B and D meson systems. Predominantly built to study *CP* violation in the B meson system, BABAR and Belle had soon been successful and reported the observation of *CP* violation in decays of B^0 mesons to charmonium final states in 2001 [11, 12].

The 'golden observable' [10] of *CP* violation in the B^0 meson system is the decay-time dependent *CP* asymmetry between the $B^0 \to J/\psi K^0_S$ and $\overline{B}^0 \to J/\psi K^0_S$ decay rates

$$\mathcal{A}_{CP}(t) \equiv \frac{\Gamma(\overline{B}^0(t) \to J/\psi K^0_S) - \Gamma(B^0(t) \to J/\psi K^0_S)}{\Gamma(\overline{B}^0(t) \to J/\psi K^0_S) + \Gamma(B^0(t) \to J/\psi K^0_S)} ,$$

that can be related to the angle β of the Cabibbo-Kobayashi-Maskawa (CKM) quark mixing matrix as the source of *CP* violation in the SM [13]. In recent years, the value of $\sin(2\beta)$ was measured to a precision of below 3 % with a world average of $\sin(2\beta) = 0.682 \pm 0.019$, dominated by the measurements of BABAR and Belle [14]. Taking into account measurements of other parameters that constrain the value of $\sin(2\beta)$ to $0.711^{+0.017}_{-0.041}$ [15], a small discrepancy to the direct measurement is observed.

The presence of this statistically insignificant but visible tension illustrates the principle idea of precision measurements of CKM parameters. Although, the conditions presented by Sakharov are met in the SM, the magnitude of *CP* violation is not large enough to sufficiently explain the baryon asymmetry. Consequently, the source of the *CP* violation has to originate from physics beyond the SM. One way to cope with this, is the direct search for new particles at higher mass scales. However, this has not been very successful until now. Another promising way is to conduct indirect searches. Quantum loop processes may contain contributions from heavy particles even if they take place at far lower energies than necessary to produce those directly, thus allowing to get a peek on physics scales far above the current experimental limits. Therefore, together with precise theory predictions, possible deviations from the SM can appear in precision measurements of SM parameters.

To meet the high demands defined by a precision measurement the experimental setup has to be customised to this very purpose. In case of decay-time dependent measurements, the spatial and time resolution has to be excellent to resolve production and decay vertices, which allow for an efficient and precise reconstruction of particle trajectories and decays. Additionally the particle identification (PID) has to be very efficient, with low mis-identification rates in order to correctly identify final state particles.

The Large Hadron Collider beauty (LHCb) detector located at the Large Hadron Collider (LHC) at the European Organization for Nuclear Research (CERN) was

designed with these requirements in mind and operates very successfully since 2009. Following its predecessors BABAR and Belle, the LHCb experiment aims to study heavy flavour physics by exploiting direct and indirect experimental techniques to their full extent. The physics program includes *CP* violation measurements in B and D meson decays [16–22], the search for (very) rare decays [23], tests of lepton-universality [24, 25], as well as heavy flavour spectroscopy [26, 27].

The analysis presented in this thesis describes the precise determination of the CKM parameter $\sin(2\beta)$ in a measurement of the decay-time dependent *CP* asymmetry $\mathcal{A}_{CP}(t)$ in the decay of B^0 and $\overline{B}^0$ mesons into their common $J/\psi K^0_S$ final state. Flavour tagging algorithms are used to determine the state of the B meson at production and are therefore of critical importance to the measurement of the *CP* asymmetry. The LHCb experiment is the only detector capable of sophisticated flavour tagging in a hadronic environment and sets performance benchmarks for flavour tagged *CP* analyses at hadron colliders.

The measurement is conducted on a dataset collected by the LHCb experiment during the first LHC run period in 2011 and 2012. Based on a dataset corresponding to an integrated luminosity of $3.0\,\text{fb}^{-1}$ collected at a centre-of-mass energy of 7 and 8 TeV the measurement supersedes a previous measurement by LHCb [28] on a subset of the data corresponding to an integrated luminosity of $1.0\,\text{fb}^{-1}$.

The updated analysis makes use of the larger dataset, an optimized selection, and adds an additional flavour tagging algorithm to identify the quark content of the B meson at production. Therewith, the statistical power of the measurement can be increased by almost a factor of 6.

Collaboration

The work presented in this document was only possible to achieve in close collaboration with colleagues from the LHCb collaboration, most notably Frank Meier and Julian Wishahi from the local working group, they are—together with the author—the contact authors of this analysis published as:

> R. Aaij *et al.*, *Measurement of CP violation in* $B^0 \to J/\psi K^0_S$ *decays*, Phys. Rev. Lett. **115** (2015) 031601, DOI: 10.1103/PhysRevLett.115.031601, arXiv:1503.07089 [hep-ex].

Mirco Dorigo and Ulrich Eitschberger from the flavour tagging group provided the flavour tagging calibration measurements (cf. Secs. 4.3.2 and 4.3.3). The calculation of the kaon regeneration (cf. Sec. 5.7.4) was performed by Jeroen van Tilburg from the B to charmonium working group.

Outline

Ch. 2 shortly recapitulates the SM with an emphasis on flavour physics and *CP* violation in the quark sector. The nature of Yukawa interactions and the appearance of the CKM matrix through spontaneous symmetry breaking are summarised.

Then, the time evolution of B mesons including decay and flavour oscillations is outlined. Finally, an overview of the measurement of CP violation in the decay of $B^0 \to J/\psi K^0_S$ is given.

The LHCb detector and its subsystems are briefly described in Ch. 3 with particular attention to the track reconstruction and particle identification techniques. The LHCb trigger system is sketched and the software stack is depicted. Also, the data taking in the first successful years of running is summarised.

Playing an important role in this analysis, the flavour tagging algorithms utilised at LHCb are discussed in more detail in Ch. 4. After a general overview and a comparison to developments at the B factories, the flavour tagging algorithms are explained. Afterwards, the calibration of the flavour tagging output is motivated and described. The chapter closes with an outlook on recent developments.

The main part (Ch. 5) contains the details of the performed measurement. The data taking and preparation is explained as well as studies of potential background contributions. The influence of decay time acceptance and resolution effects is briefly summarised. Before the results are presented, the likelihood function is described. Finally, all studies of systematic effects are collected.

The results are summarised and put into context to the global CKM picture and prospects for Run II and the LHCb detector upgrade are presented.

2 *CP* violation in the B^0 meson system

In this chapter the theoretical background of CP violation in the B^0 meson system is outlined. Starting with the Standard Model of Particle Physics the theoretical framework constructed to explain the observed phenomenology of fundamental particles and their interactions is described. Then an overview off the field of flavour physics is given, including the baseline ideas of quark mixing and CP violation in the B meson system, as well as the *master equations* utilised in the measurement of CP violation in the decay channel $B^0 \to J/\psi K^0_S$.

2.1 The Standard Model of Particle Physics

The Standard Model of Particle Physics (SM) tries to describe the constituents of matter and anti-matter as well as their interactions. The theoretical model has been rigorously tested by experiments and any attempts to falsify even a part of it have been unsuccessful up to date. From the beginning of the 1960s until the discovery of the Higgs boson [29] all experimental evidence has been in support of the SM. Nevertheless, the SM must be part of some bigger universal theory: The absence of a suitable dark matter candidate, a missing predictive model explaining the quark and lepton mass hierarchy and mixing, and the absence of anti-matter/the abundance of matter in the visible universe, are just a selection of questions that are not answered by the SM.

The theoretical framework of the SM is built as a Lorentz invariant quantum field theory describing the dynamics and kinematics of the theory. Based on the gauge group $\mathrm{SU}(3) \otimes \mathrm{SU}(2) \otimes \mathrm{U}(1)$ the SM Lagrangian $\mathcal{L}_{\mathrm{SM}}$ describes all[1] known fundamental forces and their bosonic force mediators, the fermionic particles forming matter, as well as the scalar field that lends masses to the bosons and fermions of the SM through the mechanism of spontaneous symmetry breaking.

The fermionic fields can be expressed by their left-handed doublets of quarks

$$\begin{pmatrix} u \\ d' \end{pmatrix}_{\mathrm{L}} \quad \begin{pmatrix} c \\ s' \end{pmatrix}_{\mathrm{L}} \quad \begin{pmatrix} t \\ b' \end{pmatrix}_{\mathrm{L}}$$

and leptons

$$\begin{pmatrix} \nu_e \\ e \end{pmatrix}_{\mathrm{L}} \quad \begin{pmatrix} \nu_\mu \\ \mu \end{pmatrix}_{\mathrm{L}} \quad \begin{pmatrix} \nu_\tau \\ \tau \end{pmatrix}_{\mathrm{L}}$$

[1] The SM does not describes gravity, which makes it not less attractive from the perspective of high energy particle physics as the strength of the gravitational couplings is several orders of magnitude smaller compared to the other forces.

as well as their right-handed singlet counterparts

$$e_{\mathrm{R}},\ \mu_{\mathrm{R}},\ \tau_{\mathrm{R}},\ u_{\mathrm{R}},\ d_{\mathrm{R}},\ c_{\mathrm{R}},\ s_{\mathrm{R}},\ t_{\mathrm{R}},\ \text{and}\ b_{\mathrm{R}}\,.$$

The SM does not include right-handed neutrinos, yet they might be necessary to explain the observed non-vanishing neutrino masses. To each listed particle, an anti-particle with oppositely signed charge quantum numbers exist, usually denoted with an overbar, e.g. $\overline{q}$.

The fundamental interactions are represented by the electromagnetic (e.m.) force, the weak force, and the strong force. The e.m. and weak interactions can be unified into the so called electro-weak interaction [30], represented by an $\mathrm{SU}(2) \otimes \mathrm{U}(1)$ gauge group. Four corresponding massless gauge bosons are present that can be associated with the SU(2) and U(1) group. After the spontaneous breaking of the symmetry at the electro-weak energy scale the massless photon γ and the massive $W^{\pm}$ and Z^0 bosons emerge.

The photon couples to particles with non-zero e.m. charge, i.e. the charged leptons e, μ, and τ and the quarks. The likewise uncharged Z^0 additionally couples to the uncharged neutrinos. The bosons $W^{\pm}$ act as mediators between the upper and lower fields of the fermionic doublets enabling e.g. the radioactive β decay with a $d \to u e \overline{\nu}_e$ transition through the exchange of a W^-.

Finally, the strong force couples to the colour charge carried solely by quarks and is mediated by gluons. Quarks cannot be observed in unbound states, thus always form composite particles (*hadrons*) as e.g. the proton consists of two u-quarks and one d-quark. In general, particles composed of three quarks (qqq) or three anti-quarks ($\overline{qqq}$) are called *baryons*, particles with a quark and an anti-quark as constituents ($q\overline{q}$) are called *mesons*. Besides these two prevalent bound states, exotic *pentaquark* states composed of four quarks and one anti-quark were experimentally confirmed recently [27].

All visible matter consists entirely of first generation quarks (u and d) and leptons (e), thus no other fermionic particles are mandatory to explain most physical phenomena and moreover it seems non-essential that they exist at all. To shed light into this puzzle the structure and hierarchy of the quark and lepton sector is studied in the field of *flavour physics*.

2.2 Flavour physics

The field of flavour physics includes the description of the weak interaction of quarks and leptons, mixing of neutral meson systems, and in general the time evolution of those states. Inferred by the nature of the Yukawa interactions *CP* violation is possible and present in nature. In this thesis the focus is laid on the quark sector. This introduction follows Refs. [31–33].

2.2.1 The CKM quark mixing matrix

To ensure local $\mathrm{SU}(2)\otimes\mathrm{U}(1)$ gauge invariance of the electroweak Lagrangian while at the same time preserving renormalisability of the theory, the mechanism of spontaneous symmetry breaking is used [34]. While the mechanism also implies new massive vector boson fields as well as the appearance of a massive scalar particle—the Higgs boson—the focus here will lie on the quark sector.

By introducing a complex scalar Higgs field $\phi \equiv \left(\begin{smallmatrix}\phi^+\\ \phi^0\end{smallmatrix}\right)$ an $\mathrm{SU}(2)\otimes\mathrm{U}(1)$ invariant Yukawa Lagrangian $\mathcal{L}_Y$ for the quark sector can be written as,

$$\mathcal{L}_Y^q = -Y_{ij}^{d\prime}\overline{Q_{\mathrm{L}i}}\phi d_{\mathrm{R}j}^{\prime} - Y_{ij}^{u}\overline{Q_{\mathrm{L}i}}\phi^* u_{\mathrm{R}j} + \mathrm{h.c.}\,, \tag{2.1}$$

with Y_{ij}^q denoting the Yukawa couplings, $Q_{\mathrm{L}i}$ being the left-handed quark doublets, and $q_{\mathrm{R}j}$ the right-handed singlets.

By construction still being massless, the charged leptons, quarks, and the $W^\pm$ and Z^0 bosons obtain masses after the spontaneous breaking of the symmetry and substituting the Higgs field by its vacuum expectation value

$$\langle\phi\rangle = \frac{1}{\sqrt{2}}\begin{pmatrix}0\\ v\end{pmatrix}. \tag{2.2}$$

The Yukawa couplings Y_{ij} are not constrained by the theory and thus are completely arbitrary and constitute the majority of the free SM parameters. The coupling matrices are a priori non-diagonal in the weak interaction base, but in general can be diagonalised by bi-unitary transformations. As a consequence of the diagonalisation the quark fields are transformed as well into the mass eigenstates basis allowing for flavour-changing currents through $W^\pm$ boson exchange

$$\frac{-g}{\sqrt{2}}\left(\overline{u},\overline{c},\overline{t}\right)_{\mathrm{L}}\gamma^\mu W_\mu^+ V_{\mathrm{CKM}}\begin{pmatrix}d\\ s\\ b\end{pmatrix}_{\mathrm{L}}, \tag{2.3}$$

with the weak charge g and the transformation matrix denoted V_{CKM} [8, 35]. The CKM matrix elements V_{CKM}^{ij} connect an up-type quark i to a down-type quark j with a probability proportional to $|V_{\mathrm{CKM}}^{ij}|^2$. By definition, the 3×3 CKM matrix is unitary, $V_{\mathrm{CKM}}V_{\mathrm{CKM}}^\dagger = \mathbb{1}$, and complex, with 18 free parameters. Following the unitarity conditions

$$\sum_i V_{ij}V_{ik}^* = \delta_{jk} \;\text{ and }\; \sum_j V_{ij}V_{kj}^* = \delta_{ik}\,, \tag{2.4}$$

and a redefinition of arbitrary quark phases, reduces the number of parameters to three angles and one complex phase. The matrix elements are denoted as

$$\begin{pmatrix}d^\prime\\ s^\prime\\ b^\prime\end{pmatrix}_{\mathrm{L}} = \begin{pmatrix}V_{ud} & V_{us} & V_{ub}\\ V_{cd} & V_{cs} & V_{cb}\\ V_{td} & V_{ts} & V_{tb}\end{pmatrix}\begin{pmatrix}d\\ s\\ b\end{pmatrix}_{\mathrm{L}} = V_{\mathrm{CKM}}\begin{pmatrix}d\\ s\\ b\end{pmatrix}_{\mathrm{L}} \tag{2.5}$$

and can be expressed as a complex rotation matrix with the three angles θ_{12}, θ_{13}, $\theta_{23} \in [0, \pi/2]$ and a phase $\delta \in]-\pi, \pi]$. With the definition of $s_{ij} \equiv \sin\theta_{ij}$ and $c_{ij} \equiv \cos\theta_{ij}$, an exact representation [36] of the CKM matrix can be written as

$$V_{\text{CKM}} = \begin{pmatrix} c_{12}c_{13} & s_{12}c_{13} & s_{13}\mathrm{e}^{-\mathrm{i}\delta} \\ -s_{12}c_{23} - c_{12}s_{23}s_{13}\mathrm{e}^{\mathrm{i}\delta} & c_{12}c_{23} - s_{12}s_{23}s_{13}\mathrm{e}^{\mathrm{i}\delta} & s_{23}c_{13} \\ s_{12}s_{23} - c_{12}c_{23}s_{13}\mathrm{e}^{\mathrm{i}\delta} & -c_{12}s_{23} - s_{12}c_{23}s_{13}\mathrm{e}^{\mathrm{i}\delta} & c_{23}c_{13} \end{pmatrix} . \quad (2.6)$$

where the phase δ is the only source of *CP* violation in the SM. A popular approximation by Wolfenstein [37] takes advantage of the measured hierarchy of the matrix elements, where the diagonal elements are of $\mathcal{O}(1)$, while the off-diagonal elements follow $|V_{ub}|^2 \ll |V_{cb}|^2 \ll |V_{us}|^2 \ll 1$ or in terms of the rotation angles $s_{12} \ll s_{23} \ll s_{12} \ll 1$. Exploiting this hierarchy in terms of an expansion leads to the Wolfenstein parametrisation

$$V_{\text{CKM}} = \begin{pmatrix} 1 - \frac{1}{2}\lambda^2 - \frac{1}{8}\lambda^4 & \lambda & A\lambda^3(\rho - \mathrm{i}\eta) \\ -\lambda + A^2\lambda^5(\frac{1}{2} - \rho - \mathrm{i}\eta) & 1 - \frac{1}{2}\lambda^2 - \frac{1}{8}\lambda^4(1 + 4A^2) & A\lambda^2 \\ A\lambda^3(1 - \rho - \mathrm{i}\eta) + \frac{1}{2}A\lambda^5(\rho + \mathrm{i}\eta) & -A\lambda^2 + A\lambda^4(\frac{1}{2} - \rho - \mathrm{i}\eta) & 1 - \frac{1}{2}A^2\lambda^4 \end{pmatrix} + \mathcal{O}(\lambda^6) , \quad (2.7)$$

written in terms of

$$s_{12} = \lambda, \quad s_{23} = A\lambda^2, \text{ and } s_{13}\mathrm{e}^{\mathrm{i}\delta} = A\lambda^3(\rho + \mathrm{i}\eta) . \quad (2.8)$$

The parameters are measured in the SM as $\lambda \approx 0.23$, $A \approx 0.81$, $\rho \approx 0.13$, and $\eta \approx 0.26$. Given the unitarity relations in Eq. (2.4) the six vanishing combinations can be represented in a triangle in the complex plane. The most prominent (d, b) unitarity triangle arises from

$$V_{ud}V_{ub}^* + V_{cd}V_{cb}^* + V_{td}V_{tb}^* = 0 \quad (2.9)$$

where normalising each side of the triangle by $V_{cd}V_{cb}^*$ yields vertices at $(0, 0)$ and $(1, 0)$ and an apex at $(\overline{\rho}, \overline{\eta})$. The area of all unitarity triangles is of equal size and can be expressed as half of the Jarlskog invariant $J = \pm \operatorname{Im} V_{ik}V_{jl}V_{il}^*V_{jk}^*$ with $i \neq j$ and $l \neq k$. It is a measure of *CP* violation in the SM and can be determined to be $|J| = \lambda^6 A^2 \eta \approx 3 \cdot 10^{-5}$.

The angles and the sides of the triangle can be expressed in terms of the matrix elements as

$$\alpha = \arg\left(-\frac{V_{td}V_{tb}^*}{V_{ud}V_{ub}^*}\right) , \ \beta = \arg\left(-\frac{V_{cd}V_{cb}^*}{V_{td}V_{tb}^*}\right) , \ \gamma = \arg\left(-\frac{V_{ud}V_{ub}^*}{V_{cd}V_{cb}^*}\right) , \quad (2.10)$$

and

$$R_t = \left|\frac{V_{td}V_{tb}^*}{V_{cd}V_{cb}^*}\right| , \quad R_u = \left|\frac{V_{ud}V_{ub}^*}{V_{cd}V_{cb}^*}\right| , \quad R_c = \left|\frac{V_{cd}V_{cb}^*}{V_{cd}V_{cb}^*}\right| , \quad (2.11)$$

which simplifies to

$$R_t e^{-i\beta} + R_u e^{-i\gamma} = \mathbb{1}\,. \tag{2.12}$$

Considering various measurements of parameters of the (u, d) unitarity triangle allows to constraint the apex in the $(\overline{\rho}, \overline{\eta})$-plane [38, 39] as shown in Fig. 2.1.

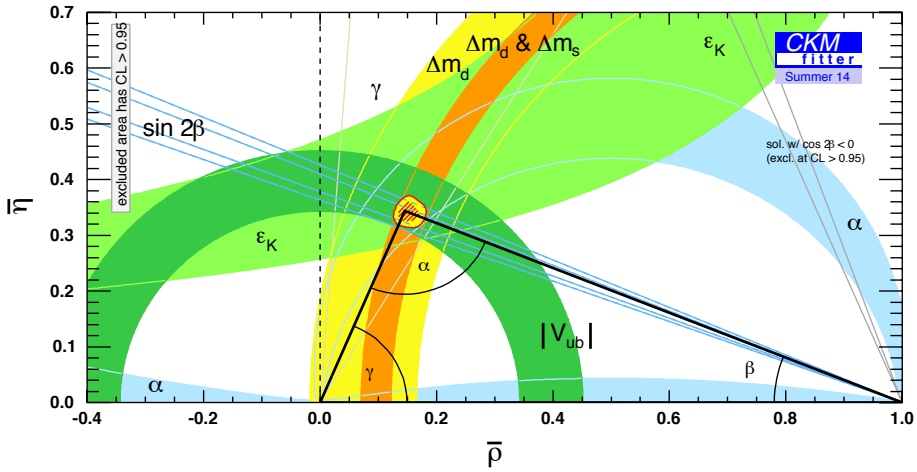

Figure 2.1 – Constraints on the (d, b) unitarity triangle in the $(\overline{\rho}, \overline{\eta})$-plane from a global fit incorporating all measured CKM parameters [38]. Regions outside the coloured areas have $1 - p > 95.45\,\%$. The red hashed region of the global combination corresponds to 68 % CLs.

2.2.2 *B* meson decay

The decay of a meson state P or its CP conjugate state $\overline{P}$ into a multi-particle final state f or its CP conjugate state $\overline{f}$ can be expressed by the decay amplitudes

$$\begin{aligned} A_f &= \langle f|H|P\rangle, & \overline{A}_f &= \langle f|H|\overline{P}\rangle, \\ A_{\overline{f}} &= \langle \overline{f}|H|P\rangle, \text{ and } & \overline{A}_{\overline{f}} &= \langle \overline{f}|H|\overline{P}\rangle, \end{aligned} \tag{2.13}$$

where H is the Hamiltonian governing the weak interaction.

Under the premise of $(CP)^2 = \mathbb{1}$ the initial and final states transform under the CP operation as

$$\begin{aligned} CP|P\rangle &= e^{+i\zeta_M}|\overline{P}\rangle, & CP|f\rangle &= e^{+i\zeta_f}|\overline{f}\rangle, \\ CP|\overline{P}\rangle &= e^{-i\zeta_M}|P\rangle, \text{ and } & CP|\overline{f}\rangle &= e^{-i\zeta_f}|f\rangle, \end{aligned} \tag{2.14}$$

introducing phases ζ_M and ζ_f. If the CP symmetry is conserved $\overline{A}_{\overline{f}} = e^{i(\zeta_f - \zeta_M)} A_f$.

2.2.3 Oscillations of neutral *B* mesons

To understand the oscillation of a neutral meson state P^0 into its $\overline{P}^0$ *CP* conjugate state and vice versa, the time evolution of the meson states has to be studied. Given a pure P^0 or $\overline{P}^0$ initial state at $t = 0$, it will evolve in time acquiring components that describe all possible final states $f_1, f_2, \ldots$,

$$\big|\Psi(t)\big\rangle = \psi_1(t)\big|P^0\big\rangle + \psi_2(t)\big|\overline{P}^0\big\rangle + c_1(t)\big|f_1\big\rangle + c_2(t)\big|f_2\big\rangle + \ldots \,. \tag{2.15}$$

As only the parameters $\psi_1(t)$ and $\psi_2(t)$ are of interest, this time evolution can be described by a Schrödinger-like equation,

$$i\frac{\mathrm{d}}{\mathrm{d}t}\begin{pmatrix}\psi_1\\ \psi_2\end{pmatrix} = H\begin{pmatrix}\psi_1\\ \psi_2\end{pmatrix} = \begin{pmatrix}m_{11} - \frac{\mathrm{i}}{2}\Gamma_{11} & m_{12} - \frac{\mathrm{i}}{2}\Gamma_{12}\\ m_{21} - \frac{\mathrm{i}}{2}\Gamma_{21} & m_{22} - \frac{\mathrm{i}}{2}\Gamma_{22}\end{pmatrix}\begin{pmatrix}\psi_1\\ \psi_2\end{pmatrix}, \tag{2.16}$$

following the Weisskopf-Wigner approximation [40, 41] with two Hermitian 2×2 matrices M and Γ, where the Hamiltonian

$$H = M - \frac{\mathrm{i}}{2}\Gamma \tag{2.17}$$

is not Hermitian, as otherwise the meson states would just oscillate without decaying.

Assuming *CPT* invariance, $m_{11} = m_{22} = m$, $m_{21} = m_{12}^*$, $\Gamma_{11} = \Gamma_{22} = \Gamma$, and $\Gamma_{21} = \Gamma_{12}^*$. Diagonalising the Hamiltonian yields eigenstates with well-defined masses

$$\begin{aligned}\big|P_L^0\big\rangle &= p\big|P^0\big\rangle + q\big|\overline{P}^0\big\rangle\,, \text{ and}\\ \big|P_H^0\big\rangle &= p\big|P^0\big\rangle - q\big|\overline{P}^0\big\rangle\,,\end{aligned} \tag{2.18}$$

with $|q|^2 + |p|^2 = 1$, where P_L marks the light and P_H the heavy eigenstate. The correspondent eigenvalues are

$$\begin{aligned}\mu_H &= m_H - \frac{\mathrm{i}}{2}\Gamma_H\,, \text{ and}\\ \mu_L &= m_L - \frac{\mathrm{i}}{2}\Gamma_L\,.\end{aligned} \tag{2.19}$$

with the definitions of the average mass and decay width

$$m = \frac{m_H + m_L}{2}\,, \text{ and } \Gamma = \frac{\Gamma_H + \Gamma_L}{2}\,, \tag{2.20}$$

and the mass and decay width differences

$$\Delta m = m_H - m_L\,, \text{ and } \Delta\Gamma = \Gamma_H - \Gamma_L\,. \tag{2.21}$$

The mass difference Δm of the two mass eigenstates is by definition positive while the sign of $\Delta\Gamma$ has to be determined experimentally.

2.2.4 Time evolution of meson states

After an outline of the decay and the oscillation of B mesons and the CKM mechanism in the SM the time evolution and differential decay rates are defined in the following. The time evolution of a physical state produced as $t = 0$ either as a pure $\left|P^0\right\rangle$ or $\left|\overline{P}^0\right\rangle$ state is now described by

$$\begin{aligned} \left|P^0_{\text{phys}}(t)\right\rangle &= g_+(t)\left|P^0\right\rangle - \frac{q}{p} g_-(t)\left|\overline{P}^0\right\rangle, \text{ and} \\ \left|\overline{P}^0_{\text{phys}}(t)\right\rangle &= g_+(t)\left|\overline{P}^0\right\rangle - \frac{p}{q} g_-(t)\left|P^0\right\rangle, \end{aligned} \tag{2.22}$$

where the coefficients $g_\pm$ are defined as

$$g_\pm(t) \equiv \frac{1}{2}\left[\mathrm{e}^{-\mathrm{i}\mu_H t} \pm \mathrm{e}^{-\mathrm{i}\mu_L t}\right] = \frac{1}{2}\left[\mathrm{e}^{-\mathrm{i}m_H t}\mathrm{e}^{-\frac{1}{2}\Gamma_H t} \pm \mathrm{e}^{-\mathrm{i}m_L t}\mathrm{e}^{-\frac{1}{2}\Gamma_L t}\right]. \tag{2.23}$$

The decay rate of a meson produced at $t = 0$ to a final state f at time t is given by the matrix element

$$\Gamma\left(P(t) \to f\right) = \left|\left\langle f\middle|T\middle|P\right\rangle\right|^2, \tag{2.24}$$

which yields the four differential decay rates

$$\begin{aligned} &\frac{\Gamma(P(t) \to f)}{\mathrm{e}^{-\Gamma t}} = \frac{1}{2}\left|A_f\right|^2\left(1 + \left|\lambda_f\right|^2\right) \\ &\left[\cosh\!\left(\frac{\Delta\Gamma t}{2}\right) + D_f \sinh\left(\frac{\Delta\Gamma t}{2}\right) + C_f \cos(\Delta m t) - S_f \sin(\Delta m t)\right], \\ &\frac{\Gamma(P(t) \to \overline{f})}{\mathrm{e}^{-\Gamma t}} = \frac{1}{2}\left|\overline{A}_{\overline{f}}\right|^2\left(1 + \left|\overline{\lambda}_{\overline{f}}\right|^2\right)\left|\frac{q}{p}\right|^2 \\ &\left[\cosh\!\left(\frac{\Delta\Gamma t}{2}\right) + D_{\overline{f}} \sinh\left(\frac{\Delta\Gamma t}{2}\right) + C_{\overline{f}} \cos(\Delta m t) - S_{\overline{f}} \sin(\Delta m t)\right], \\ &\frac{\Gamma(\overline{P}(t) \to f)}{\mathrm{e}^{-\Gamma t}} = \frac{1}{2}\left|A_f\right|^2\left(1 + \left|\lambda_f\right|^2\right)\left|\frac{p}{q}\right|^2 \\ &\left[\cosh\!\left(\frac{\Delta\Gamma t}{2}\right) + D_f \sinh\left(\frac{\Delta\Gamma t}{2}\right) - C_f \cos(\Delta m t) + S_f \sin(\Delta m t)\right], \\ &\frac{\Gamma(\overline{P}(t) \to \overline{f})}{\mathrm{e}^{-\Gamma t}} = \frac{1}{2}\left|\overline{A}_{\overline{f}}\right|^2\left(1 + \left|\overline{\lambda}_{\overline{f}}\right|^2\right) \\ &\left[\cosh\!\left(\frac{\Delta\Gamma t}{2}\right) + D_{\overline{f}} \sinh\left(\frac{\Delta\Gamma t}{2}\right) - C_{\overline{f}} \cos(\Delta m t) + S_{\overline{f}} \sin(\Delta m t)\right], \end{aligned} \tag{2.25}$$

where the definitions

$$\lambda_f \equiv \frac{1}{\overline{\lambda}_f} = \frac{q}{p}\frac{\overline{A}_f}{A_f}, \text{ and } \overline{\lambda}_{\overline{f}} \equiv \frac{1}{\lambda_{\overline{f}}} = \frac{p}{q}\frac{A_{\overline{f}}}{\overline{A}_{\overline{f}}} \tag{2.26}$$

are used.

The *CP* coefficients D_i, C_i, and S_i have to satisfy $D_i^2 + C_i^2 + S_i^2 = 1$ and are defined as

$$\begin{aligned} D_f &= \frac{2\,\mathrm{Re}\,\lambda_f}{1+\left|\lambda_f\right|^2}, \quad C_f = \frac{1-\left|\lambda_f\right|^2}{1+\left|\lambda_f\right|^2}, \quad S_f = \frac{2\,\mathrm{Im}\,\lambda_f}{1+\left|\lambda_f\right|^2}\,, \text{ and} \\ D_{\overline{f}} &= \frac{2\,\mathrm{Re}\,\overline{\lambda}_{\overline{f}}}{1+\left|\overline{\lambda}_{\overline{f}}\right|^2}, \quad C_{\overline{f}} = \frac{1-\left|\overline{\lambda}_{\overline{f}}\right|^2}{1+\left|\overline{\lambda}_{\overline{f}}\right|^2}, \quad S_{\overline{f}} = \frac{2\,\mathrm{Im}\,\overline{\lambda}_{\overline{f}}}{1+\left|\overline{\lambda}_{\overline{f}}\right|^2}\,. \end{aligned} \tag{2.27}$$

2.2.5 Classification of *CP* violating effects

While a single phase in the CKM quark mixing matrix is the only source of *CP* violation in the SM, *CP* violation appears in different manifestations.

Direct *CP* violation

CP violation in the decay—also called direct *CP* violation—occurs if the decay amplitudes of a meson into a final state differ from the *CP* conjugate decay

$$\frac{\left|\overline{A}_{\overline{f}}\right|}{\left|A_f\right|} \neq 1\,. \tag{2.28}$$

This is possible if two different *weak* phases φ_i and *strong* phases δ_i contribute to the decay amplitude, as only relative phase differences are physically meaningful and are phase-convention independent. The *CP*-odd weak phases under consideration arise from complex couplings in the Lagrangian, here the phases of the CKM matrix elements, whereas strong phases result from strong or electromagnetic final-state interactions. Strong phases are *CP*-even and thus equal for *CP* conjugate states.

Assuming a meson decay with two contributing amplitudes A_1 and A_2, with only the weak phases changing sign under *CP* transformation, the behaviour of the amplitudes under *CP* transformation

$$\begin{aligned} A_f &= A_1 \mathrm{e}^{i(\delta_1+\varphi_1)} + A_2 \mathrm{e}^{i(\delta_2+\varphi_2)}\,, \text{ and} \\ \overline{A}_{\overline{f}} &= A_1 \mathrm{e}^{i(\delta_1-\varphi_1)} + A_2 \mathrm{e}^{i(\delta_2-\varphi_2)}\,, \end{aligned} \tag{2.29}$$

implies a *CP* non-conservation as defined in Eq. (2.28). This is the only possible source of *CP* violation in charged meson systems and all baryon systems.

CP violation in mixing

The second class of *CP* violation is denoted *CP* violation in the mixing. It occurs if

$$\left|\frac{q}{p}\right| \neq 1\,. \tag{2.30}$$

A potential CP violation in the mixing of $B^0 - \overline{B}^0$ mesons was studied at the B factories by measuring $|q/p| - 1$. The final B factory average shows no significant deviation from zero: $|q/p| - 1 = (0.3 \pm 2.8) \cdot 10^{-3}$ [10]. The recent measurement of the semileptonic CP asymmetry a^d_{sl} by the LHCb collaboration confirms the quoted result. The measurement yields $a^d_{\mathrm{sl}} = (-0.02 \pm 0.19\,(\mathrm{stat}) \pm 0.30\,(\mathrm{syst}))\%$ [42] that can be expressed as

$$\left|\frac{q}{p}\right| - 1 = (0.1 \pm 0.9\,(\mathrm{stat}) \pm 1.4\,(\mathrm{syst})) \times 10^{-3}\,, \tag{2.31}$$

by employing the identity relation

$$\left|\frac{q}{p}\right| \equiv \left(\frac{1 - a^d_{\mathrm{sl}}}{1 + a^d_{\mathrm{sl}}}\right)^{\frac{1}{4}}\,. \tag{2.32}$$

CP violation in the interference

The third kind of CP violation only occurs in decays where both CP conjugate initial states P^0 and $\overline{P}^0$ decay into a common final state f. Then an interference between a decay without mixing, $P^0 \to f$, and a decay with mixing, $P^0 \to \overline{P}^0 \to f$, can lead to CP violation in the interference between both amplitudes of:

$$\mathrm{Im}\,\lambda_f \neq 0\,. \tag{2.33}$$

As can be seen in the definition of λ_f given in Eq. (2.26) this type of CP violation even occurs if no direct CP violation or CP violation in mixing is present.

2.3 *CP* violation in decays of $B^0 \to J/\psi K^0_S$

The decay mode $B^0 \to J/\psi K^0_S$ is well known as the gold-plated channel to measure CP violation in B^0 decays. With negligible contributions from doubly Cabibbo-suppressed modes, a $\overline{b} \to \overline{c}c\overline{s}$ transition dominated by a single weak phase, and an easy to reconstruct final state the analysis of $B^0 \to J/\psi K^0_S$ decays is a unique way to test the SM quark flavour sector [10].

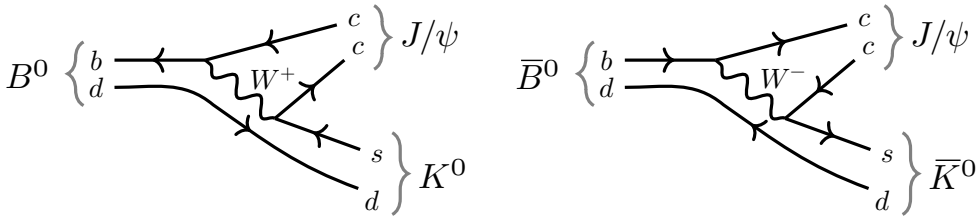

Figure 2.2 – (left) Feynman diagrams for the decays of $B^0 \to J/\psi K^0$ and (right) $\overline{B}^0 \to J/\psi \overline{K}^0$. The neutral kaon is reconstructed in the $\pi\pi$ final state.

The decay is characterized by a B^0 or $\overline{B}^0$ meson decaying into intermediate J/ψ and K^0 mesons. To take advantage of the superior detection efficiency for charged

particles the subsequent $J/\psi \to \mu^+\mu^-$ decay mode is chosen, as well as the decay of the K^0 into two oppositely charged pions. The decay $K^0 \to \pi^+\pi^-$ is mediated by the mass eigenstates K^0_S and K^0_L of the neutral kaon. Besides second-order effects discussed in Sec. 5.7.4, the *CP* violating decay of the long lived eigenstate K^0_L into two pions is neglected. Thus, the two pion final state used in this analysis with an invariant mass that matches the K^0 mass is denoted as a K^0_S. Fig. 2.2 illustrates the Feynman diagrams of the decays of B^0 and $\overline{B}^0$ into the J/ψ K^0_S final state.

The $\mu^+\mu^-\pi^+\pi^-$ final state is common to both initial B mesons, hence can be reached either directly or after mixing of the B meson states and the decay time dependent *CP* asymmetry, $\mathcal{A}_{CP}(t)$, can be defined using Eq. (2.25) as

$$\begin{aligned}\mathcal{A}_{CP}(t) &\equiv \frac{\Gamma(\overline{B}^0(t) \to J/\psi K^0_S) - \Gamma(B^0(t) \to J/\psi K^0_S)}{\Gamma(\overline{B}^0(t) \to J/\psi K^0_S) + \Gamma(B^0(t) \to J/\psi K^0_S)} \\ &= \frac{S_{J/\psi K^0_S} \sin(\Delta m_d t) - C_{J/\psi K^0_S} \cos(\Delta m_d t)}{\cosh(\frac{\Delta\Gamma t}{2}) + D_{J/\psi K^0_S} \sinh(\frac{\Delta\Gamma t}{2})}\,,\end{aligned} \tag{2.34}$$

where B^0 and $\overline{B}^0$ denote the meson production flavour at $t = 0$.

Considering the vanishing decay width difference of the two mass eigenstates, $\Delta\Gamma_d/\Gamma_d = 0.001 \pm 0.010$ [14], the *CP* asymmetry further simplifies to

$$\mathcal{A}_{CP}(t) = S_{J/\psi K^0_S} \sin(\Delta m_d t) - C_{J/\psi K^0_S} \cos(\Delta m_d t)\,. \tag{2.35}$$

The *CP* coefficients introduced in Eq. (2.27) can be approximated to a high precision to be

$$C_{J/\psi K^0_S} = 0\,, \text{ and } S_{J/\psi K^0_S} = \sin(2\beta)\,, \tag{2.36}$$

as direct *CP* violation is expected to be small $|\overline{A}_{J/\psi K^0_S}/A_{J/\psi K^0_S}| \approx 1$, and *CP* violation in mixing is experimentally excluded $|q/p| = 1$. Thus, eventually the *CP* asymmetry reduces to

$$\mathcal{A}_{CP}(t) \approx \sin(2\beta)\sin(\Delta m_d t)\,, \tag{2.37}$$

with $\Delta m_d = 0.510\,\hbar\,\mathrm{ps}^{-1}$ [33].

In principle, the *CP* violating phase 2β can be enhanced by an additional phase $\Delta\phi$ from loop-suppressed penguin diagrams

$$S_{J/\psi K^0_S} = \sin(2\beta + \Delta\phi)\,. \tag{2.38}$$

An elaborated description can e.g. be found in Ref. [43]. In order to distinguish between new *CP* violating phases from Beyond Standard Model (BSM) processes and a phase shift from suppressed penguin contributions, the size of $\Delta\phi$ can be controlled with the help of the U-spin symmetry [44]. As a subgroup of the flavour SU(3), the U-spin symmetry represents the interchange of all down and strange quarks. Thus, the decay of $B^0 \to J/\psi K^0_S$ is linked to the decay of $B^0_s \to J/\psi K^0_S$ via U-spin symmetry. This allows—only theoretically limited by

U-spin breaking corrections—to constraint the penguin contributions on $\sin(2\beta)$ [45] and provides additional motivation to measure CP violation in $B^0_s \to J/\psi K^0_S$ [16]. Calculations based on an operator product expansion constraint the phase from penguin contributions to [46]

$$|\Delta\phi| \leq 0.68^\circ\,, \tag{2.39}$$

therefore, still lying below current experimental limits, but in the reach of future measurements.

The current world average, [14]

$$\sin(2\beta) = 0.679 \pm 0.020\,,$$

is dominated by measurements by BABAR and Belle in the $B^0 \to J/\psi K^0_S$ channel where both the e^+e^- and $\mu^+\mu^-$ final states of the J/ψ as well as the $\pi^+\pi^-$ and $\pi^0\pi^0$ final states of the K^0_S are studied. The Belle collaboration [47] reports

$$\begin{aligned} S^{\text{Belle}}_{J/\psi K^0_S} &= 0.670 \pm 0.029\,(\text{stat}) \pm 0.013\,(\text{syst})\,, \text{ and} \\ C^{\text{Belle}}_{J/\psi K^0_S} &= 0.015 \pm 0.021\,(\text{stat}) \pm {}^{0.023}_{0.045}\,(\text{syst})\,, \end{aligned}$$

while the BABAR measurement [48] yields

$$\begin{aligned} S^{\text{BABAR}}_{J/\psi K^0_S} &= 0.657 \pm 0.036\,(\text{stat}) \pm 0.012\,(\text{syst})\,, \text{ and} \\ C^{\text{BABAR}}_{J/\psi K^0_S} &= 0.026 \pm 0.025\,(\text{stat}) \pm 0.016\,(\text{syst})\,. \end{aligned}$$

A first measurement of $\sin(2\beta)$ was performed by the LHCb collaboration using a data sample corresponding to an integrated luminosity of $1\,\text{fb}^{-1}$ collected during Run I in 2011. The analysis comprised 8000 flavour-tagged $B^0 \to J/\psi K^0_S$ candidates, reconstructed in the $\mu^+\mu^-\pi^+\pi^-$ final state. The reported results [28] are

$$\begin{aligned} S_{J/\psi K^0_S} &= 0.73 \pm 0.07\,(\text{stat}) \pm 0.04\,(\text{syst})\,, \text{ and} \\ C_{J/\psi K^0_S} &= 0.03 \pm 0.09\,(\text{stat}) \pm 0.01\,(\text{syst})\,. \end{aligned}$$

Beside the direct measurement, the value of $\sin(2\beta)$ can be estimated by a global fit to the CKM parameter space. As this fit can be performed with and without considering the respective parameters, a χ^2 pull can be computed for each quantity. For $\sin(2\beta)$ a small tension of $\Delta\chi^2 = 1.74$ is observed. With higher order effects being small, this can either be a statistical artefact or the influence of potential BSM effects.

3 The LHCb experiment

The LHCb collaboration operates a particle detector at the LHC located at CERN in the Geneva area. Its physics scope covers precision measurements of CP violation in B and D meson systems, the search for very rare decays, as well as other areas of flavour physics as lepton-number violation studies and heavy flavour spectroscopy.

In the next sections the experimental conditions at the LHC and the design of the LHCb detector are outlined.

3.1 The LHC and its experiments

With a circumference of 26.7 km the LHC is the largest man-made particle accelerator. Using a 'two-in-one' super-conducting magnet design, two counter-rotating beams of protons (or ions) are brought to collision at four interaction points, home of the large LHC experiments ALICE, ATLAS, CMS, and LHCb. The collider's centre-of-mass energy of $\sqrt{s} = 14\,\text{TeV}$ and its peak luminosity of $L = 10^{34}\,\text{cm}^{-2}\,\text{s}^{-1}$ provide LHC's experiments with high event rates that are necessary in their searches for physics beyond the SM.

Following approval in 1994, the LHC re-used the existing Large Electron–Positron Collider (LEP) tunnel and most of its infrastructure after LEP shut down in 2000. The LHC—and former LEP—tunnel has an internal diameter of 3.7 m and is built up of eight straight and eight arc sections, which form a circle with an effective radius of 2.8 km. It is located north-west of Geneva, Switzerland at a depth between 45 m and 170 m below the surface. The storage ring consists of superconducting NbTi magnets kept at an operating temperature of 1.9 K by superfluid helium. A superconducting radio frequency cavity system captures, accelerates, and stores the two proton beams.

At design luminosity, 2808 bunches with a bunch spacing of 25 ns are stored in each proton beam. The LHC relies on a supply chain of smaller accelerators providing the initial proton bunches. Fig. 3.1 depicts the CERN accelerator complex. A bottle of hydrogen gas is the source of the protons, that are then subsequently accelerated to higher energies by the Linear Accelerator 2 (LINAC2), the Proton Synchrotron Booster (BOOSTER), the Proton Synchrotron (PS), and the Super Proton Synchrotron (SPS), before being injected into the LHC at an energy of 450 GeV. The transfer lines TI2 and TI8 are used to inject the proton bunches in both beam directions. As soon as the nominal number of proton bunches is reached, the beam energies are increased up to 7 TeV for each beam. The average LHC turnaround time, i.e. the time it takes to run through the whole accelerator chain until a stable beam is achieved, adds up to seven hours. Mainly due to beam

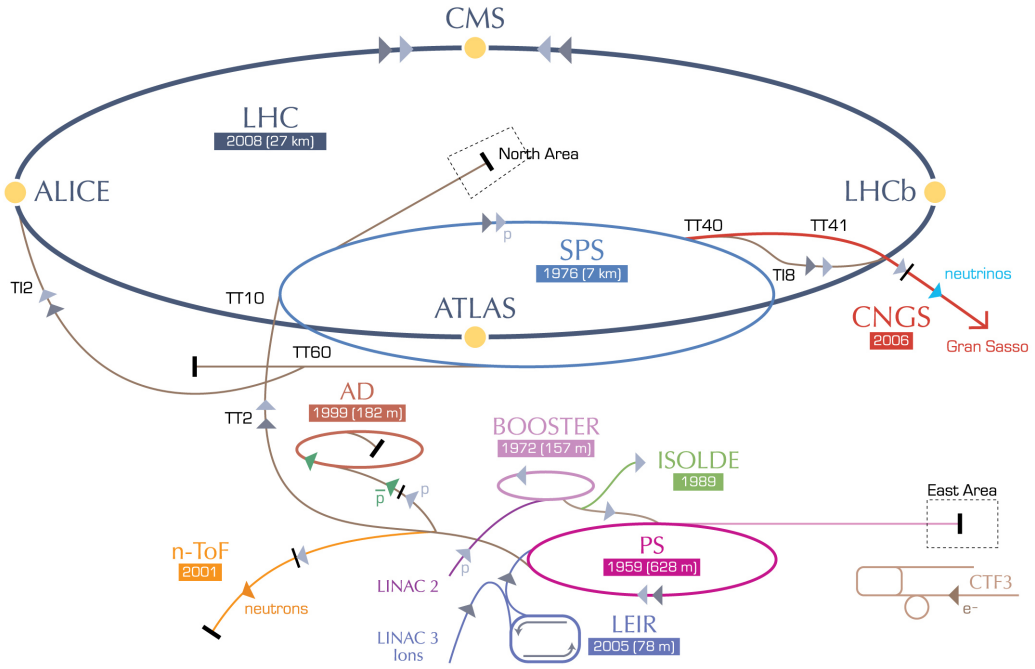

Figure 3.1 – The CERN accelerator complex [50]. Starting from the LINAC2, protons are accelerated through the BOOSTER, the PS and finally the SPS before being injected into the LHC. If one or both beams consist of heavy ions, the LINAC3 and the LEIR are used to accelerate the ions and inject them into the PS.

loss from pp collisions the beam intensities and the instantaneous luminosity decay. Starting from a peak luminosity of $L = 10^{34}\,\mathrm{cm}^{-2}\,\mathrm{s}^{-1}$ a luminosity lifetime of 15 hours is estimated. To prevent uncontrolled beam losses and to protect the LHC infrastructure and the LHC experiments a beam dump system is installed. The fully automated system monitors the beam condition and is able to extract the beam from the LHC using kicker magnets in case of a failure. The beam dump system is also used regularly to extract the beam after a successful run. For more information on the LHC and resident experiments, see e.g. Ref. [49].

Shortly after the first successful circulation of two proton beams in September 2008, a fault occurred in the electrical bus connection between two magnets, leading to a large helium leak and serious damage to several of LHC's magnets and infrastructure. After the incident, the management decided to reduce the beam energy and intensity. Thus, in the years 2010 and 2011 the LHC centre-of-mass energy was $\sqrt{s} = 7\,\mathrm{TeV}$ with a bunch spacing of 50 ns delivering a peak instantaneous luminosity of $2.4 \cdot 10^{33}\,\mathrm{cm}^{-2}\,\mathrm{s}^{-1}$. An increase of the beam energy to $\sqrt{s} = 8\,\mathrm{TeV}$ lead to a peak instantaneous luminosity of $7.7 \cdot 10^{33}\,\mathrm{cm}^{-2}\,\mathrm{s}^{-1}$ in 2012 [51].

The LHC is not only capable of colliding protons but also lead ions in Pb-Pb as well as in p-Pb and Pb-p collisions. For this purpose the ALICE ('A Large

Ion Collider Experiment') detector [52] is specifically designed to study QCD interactions and the quark-gluon plasma produced in the LHC ion runs, where the detector has to cope with very large particle multiplicities. In the case of a heavy ion run, the Linear Accelerator 3 (LINAC3) and the Low Energy Ion Ring (LEIR) mark the starting point of the accelerator chain, before injecting the lead ions into the PS.

In total, seven experiments are located at the four interaction regions of the LHC. The two multi-purpose detectors ATLAS ('A Toroidal LHC Apparatus') [53] and CMS ('Compact Muon Solenoid') [54] are installed at opposite sides of the storage ring. Both experiments cover a great variety of physics activities: the search for scalar particles, particles predicted by super-symmetric models, dark matter candidates, and evidence for extra spacial dimensions. Around the interaction regions of the CMS experiment, the TOTEM ('Total Elastic and Diffractive Cross Section Measurement') detectors [55] are located. Together with the Large Hadron Collider forward (LHCf) experiment [56], located on both sides of the ATLAS interaction region, the detectors are designated to address the study of the 'forward' region of the collisions at very small angles to the beam direction. The seventh experiment MoEDAL ('Monopole and Exotics Detector at the LHC') [57] extends the LHC physics program to the direct search for magnetic monopoles. Still missing in this list is the LHCb experiment, which will be explained in more detail in the next section.

3.2 The LHCb detector

The LHCb detector [58] is a unique precision instrument solely designed to study *CP* violation and rare decays of beauty and charm hadrons (Fig. 3.2). It is constructed as a single-arm spectrometer covering an angular range from approximately 10 mrad to 300 mrad (250 mrad) in the horizontal (vertical) plane. The detector layout exploits the characteristics of the heavy flavour production in pp collisions at the LHC. The production of heavy quarks in an hadronic environment is dominated by quark pair production in gluon-gluon fusion $gg \to b\bar{b}/c\bar{c}$ and quark-antiquark annihilation $q\bar{q} \to b\bar{b}/c\bar{c}$.

The heavy quark production cross-sections depend on the centre-of-mass energy $\sqrt{s}$ of the pp collision. As illustrated in Fig. 3.3 the $b\bar{b}$ pair cross-section behaves approximately linearly with $\sqrt{s}$ and lies roughly in the order of 300 µb for $\sqrt{s} =$ 7 TeV. At LHC energies the partons involved in the collisions are likely to carry very different momenta, leading to a strong boost of the produced quark pair in direction of the beam axis. Thus, the produced quarks have a high probability of being produced at a small azimuthal angle $\theta_{1,2}$ with respect to the beam axis. Fig. 3.4 illustrates the the correlation of the two quark angles θ_1 and θ_2. The red shaded region marks the LHCb detector acceptance in which around 25 % of all $b\bar{b}$ quark pairs are produced.

The acceptance is depicted as well in Fig. 3.4 as a function of the quark pseu-

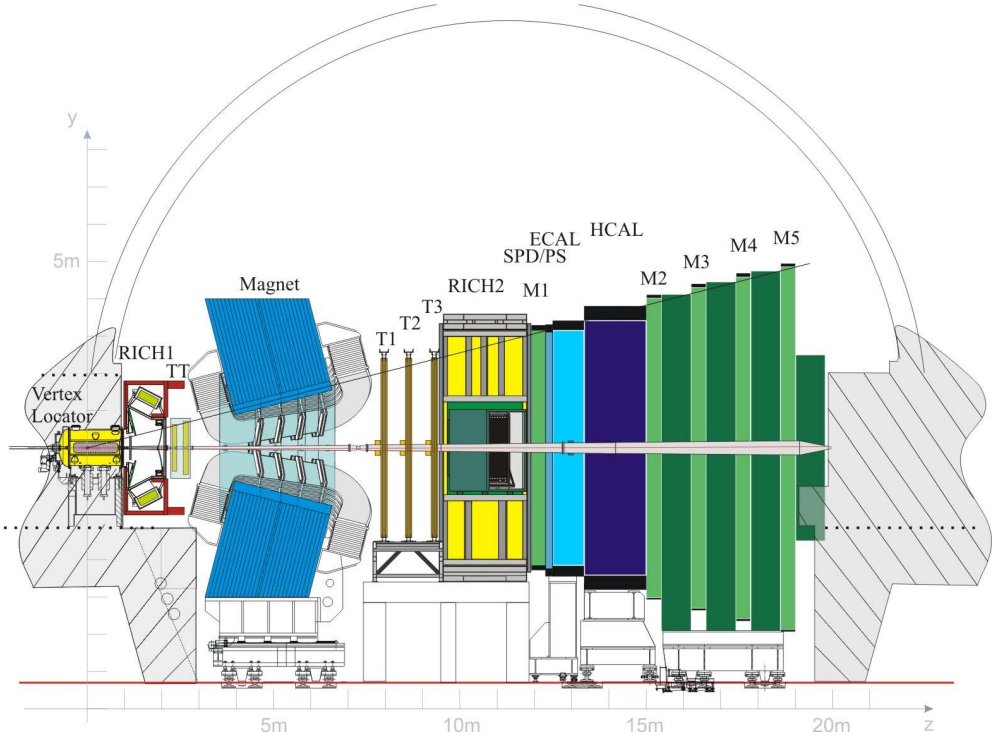

Figure 3.2 – Schematic cross section of the LHCb detector in the (y, z) plane at $x = 0$. The pp interaction region is located at the coordinates $(0, 0, 0)$ on the left side of the figure. The beam pipe crosses the detector at $(0, 0, z)$. The main interaction region is surrounded by the VELO, following the RICH1 and the TT. On the right side of the magnet the three tracking stations (T1-3) consisting of the IT and the OT are installed. Further on, the RICH2, the calorimeter system (SPD, PS, ECAL, and HCAL), and the muon system (M1-5) is located. [58]

dorapidity $\eta = -\ln(\tan(\theta/2))$. Here the LHCb acceptance region ($1.8 < \eta < 4.9$) can be identified by the red rectangle while the acceptance of the general-purpose detectors (GPDs), ATLAS and CMS, is marked by the yellow rectangle.

After production each b quark hadronises independently forming a b hadron, most likely by bounding to a light quark forming a B^+ or a B^0 (40 % each), to heavier quarks as in B_s^0 (11 %) or even b baryons as Λ_b^0 (9 %). The numbers in parenthesis denote the fraction of the total production in percent [33].

At this point, flavour conjugate states are implied as the production is in principle symmetric in quark flavour. However, as the pp collision defines an initial state with positive charge, non-zero baryon number, and in absence of any valence anti-quarks, different production rates are expected [61–63]. As this influences the flavour-sensitive CP violation measurement, the production asymmetry is studied in greater detail in Sec. 5.6.2.

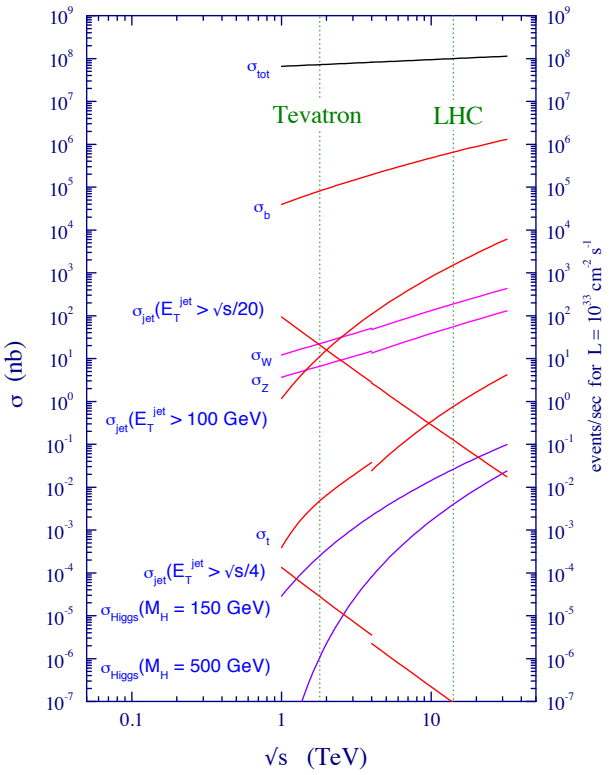

Figure 3.3 – Production cross-sections as a function of the proton-proton collision centre-of-mass energy. The green dashed lines mark the centre-of-mass energies of the Tevatron collider and the LHC. [59]

3.3 Track reconstruction

The reconstruction of charged tracks is based on information from a set of tracking detectors located around a spectrometer magnet with an integrated field of 4 Tm. The tracking system consists of the vertex locator (VELO), the tracker Turicensis (TT), the inner tracker (IT) and the outer tracker (OT). Silicon microstrips are used in the first three, while the latter is constructed as a drift-time detector.

3.3.1 The vertex locator

Surrounding the *pp* interaction region the VELO's main purpose is the precise position measurement of traversing charged particles to reconstruct the primary vertex (PV) and displaced secondary vertices (SVs). To achieve the best possible spatial resolution the sensors must be positioned close to the beam trajectory. In common designs, the sensitive region of the inner tracking layers as installed in the ATLAS and CMS experiments has a minimal distance of 4 to 5 cm to the interaction region. To allow the sensors to be as close as 8 mm to the interaction region and still prevent damage during beam injection, the VELO modules are

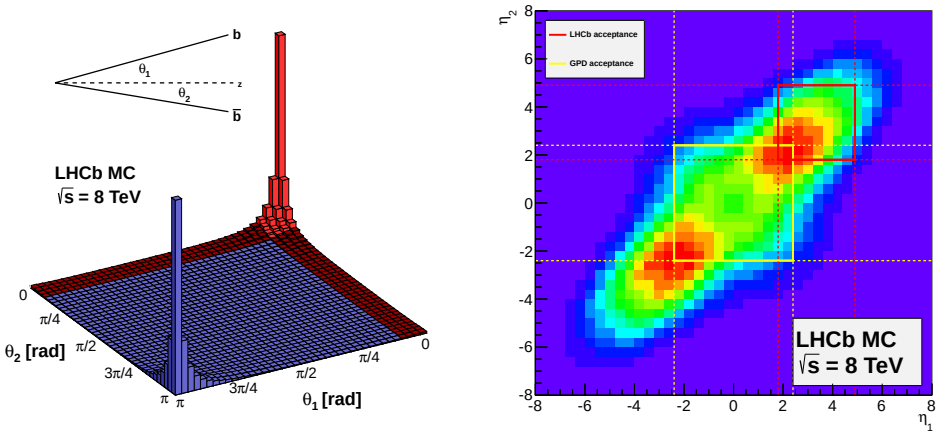

Figure 3.4 – Plots of the $b\bar{b}$ quark pair production numbers (in arbitrary units) at a centre-of-mass energy of $\sqrt{s} = 8\,\text{TeV}$ as a function of (left) the azimuthal angles $\theta_{1,2}$ and (right) the pseudorapidity (η). (Left) The red shaded region or (right) the red rectangle mark the LHCb detector acceptance. [60]

split in two halves and can be retracted until stable beams are present. Each single module consists of two half-disk shaped silicon microstrip sensor modules covering either the radial dimensions (R sensor) or the angular dimension (Φ sensor) as can be seen in the schematic visualisation in Fig. 3.5. The VELO covers the total LHCb acceptance region, such that all tracks within the acceptance cross at least three VELO stations. Fig. 3.6 shows the cross section of the VELO in the (x, z) plane at $y = 0$ with all modules visible.

3.3.2 The LHCb tracking detectors

The TT as well as the IT make use of silicon microstrip sensors to track particle trajectories. The TT station is located upstream of the magnet (just like the VELO) and is 150 cm wide and 130 cm high. The three IT stations are on the downstream side of the magnet (opposite to the interaction region) and cover a central region around the beam pipe that is 120 cm wide and 40 cm high. Each of the stations has four detector layers, where the strips in the two inner layer are rotated $\pm 5°$ to allow for two-dimensional positioning.

The outer region of the three downstream tracking stations, called OT, consists of drift-time detectors constructed from an array of gas-filled straw-tube modules. Again, each station is composed of four layers tilted to each other in the vertical plane to allow for two-dimensional resolution. The large detector spans an active area of $6 \times 5\,\text{m}^2$. With drift times smaller than 50 ns and a drift-coordinate resolution of 20 µm the OT allows for tracking in the low occupancy region around the IT.

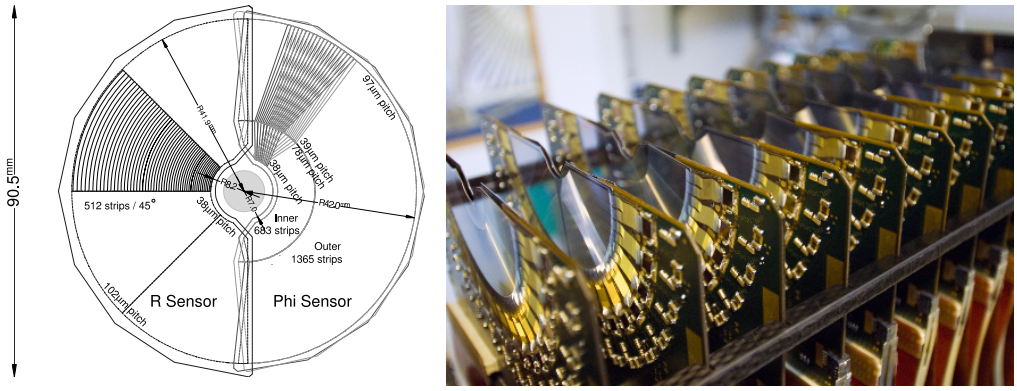

Figure 3.5 – (Left) Schematic representation of the R and Φ sensor for one of the VELO modules [58]. (Right) Picture of the VELO during assembly [64].

3.3.3 Track reconstruction technique and performance

The reconstruction of trajectories employs all available tracking information from VELO, TT, IT, and OT [65]. Each track is classified by the position of associated hits in the different subsystems (Fig. 3.7). *T tracks* only have hits in the IT and OT, *VELO tracks* only have hits in the VELO, *upstream tracks* only have hits in the VELO and TT. Tracks leaving hits in all tracking systems are called *long tracks*, while tracks with hits in each system except the VELO are called *downstream tracks*. Starting from hits in the VELO and with the knowledge of the magnetic field map, tracks are reconstructed using extrapolations of the straight track sections in the VELO to the downstream tracking stations (IT/OT). If TT hits are present they are considered as well. The reconstruction of downstream tracks starts from hits in in the downstream tracking stations that are then extrapolation through the magnet and combined with hits in the TT. Other track types are reconstructed in similar ways.

Obviously long tracks carry the most precise information and are preferred. Nevertheless, other types of reconstructed tracks are useful too. VELO tracks are employed to improve the identification of PV positions, T and upstream tracks can be utilised to enhance the ring-imaging Cherenkov detector (RICH) performance, and downstream tracks increase the number of reconstructed K^0_S and other long lived particles that may decay outside the VELO acceptance.

The average reconstruction efficiency of tracks inside the detector acceptance and in the momentum range between $5 - 200\,\text{GeV}$ is better than 95 %. The track uncertainty is below 0.5 % for muons and below 1.5 % for pions and kaons. The high quality of the tracking algorithms has a direct effect on the momentum resolution ($\Delta p/p = 0.4 - 0.6\,\%$), the invariant mass resolution ($12 - 25\,\text{MeV}/c^2$ for $B^0 \to J/\psi X$ decays), the impact parameter resolution ($20\,\mu\text{m}$), and finally provides an excellent decay time resolution of around 45 ps [66].

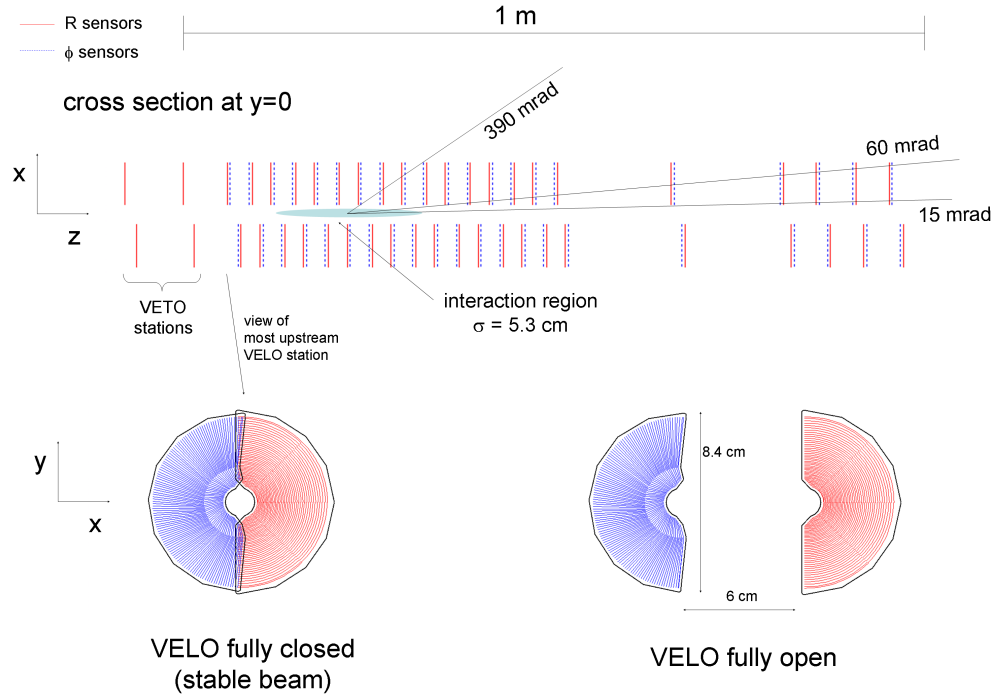

Figure 3.6 – (Top) Cross section of the closed VELO in the (x, z)-plane at $y = 0$. (Bottom) Single VELO layer in the (x, y)-plane with one R and one Φ sensor disc in open and closed state. [58].

3.4 Particle identification

The LHCb PID system consists of two RICH detectors, up- and downstream of the magnet, the calorimeter system, and the muon system. Based on the information from the PID systems a likelihood for a given particle hypothesis is determined.

3.4.1 The ring-imaging Cherenkov detectors

Exploiting the radiation emitted by a charged particle moving through a medium at a speed greater than the speed of light, the two RICH detectors are used to distinguish between pions, kaons, and protons. As illustrated in Fig. 3.8 the cherenkov angle Θ_C shows a strong momentum dependence and therefore different radiators are used to get a particle hypothesis for low- and high-momentum particles. The detectors make use of a system of flat and spherical mirrors to reflect the emitted light to hybrid photon detectors.

RICH1 is located upstream of the magnet in between the VELO and the TT, it contains aerogel and C_4F_{10} gas radiators, and provides PID for particles with low momenta from 1 to 60 GeV/c. RICH2 is located after the last tracking station,

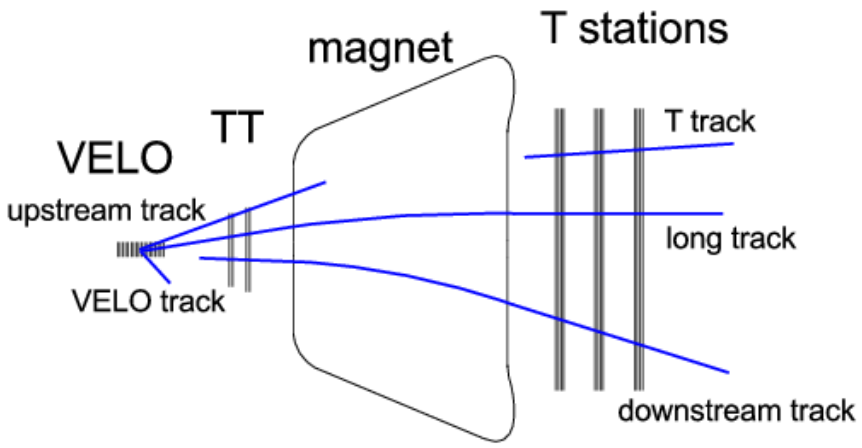

Figure 3.7 – Illustration of the LHCb tracking subsystems and track type definitions [65].

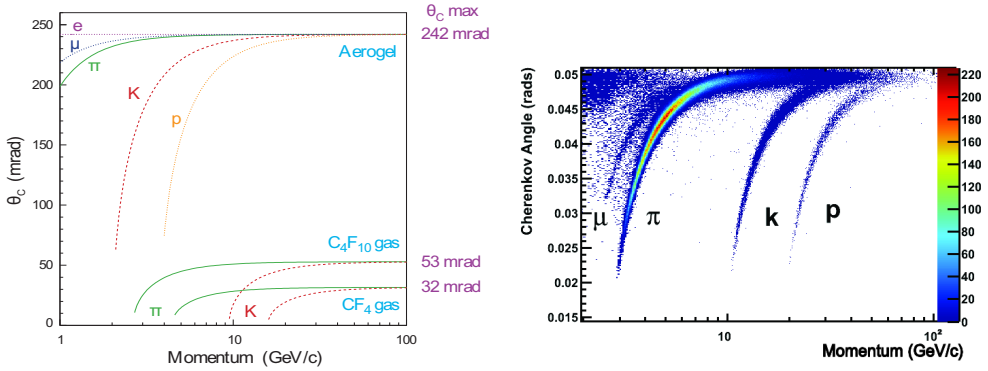

Figure 3.8 – Momentum dependence of the cherenkov angle Θ_C for (left) all RICH radiators [58] and (right) for the C_4F_{10} radiator only [67].

it uses CF_{10} gas as a radiator and allows PID for particles in the range from 15 to $\geq$100 GeV/c.

3.4.2 The calorimeter system

The LHCb calorimeter system is used for trigger (Sec. 3.5) and PID, as well as for the reconstruction of photons, electrons and neutral pions. It consists of an electromagnetic calorimeter (ECAL)—including the scintillator pad detector (SPD) and the preshower detector (PS)—followed by a hadron calorimeter (HCAL). All the calorimeter sub-systems make use of the scintillation light originating from traversing charged particles that is collected and transmitted by fibres to photomultipliers.

First, the SPD selects charged particles, secondly the PS provides separation of charged pions and electrons. Finally the ECAL measures the energy deposition and

position of electromagnetic showers. The HCAL is a massive $8.4 \times 6.8\,\mathrm{m}^2$, 500 t detector, build-up from alternating iron plates and scintillating tiles, providing energy measurements of hadronic showers.

3.4.3 The muon system

The muon system consists of five stations of multi-wire proportional chambers, provides muon PID and serves as a high transverse momentum (p_T) trigger. The system is located in front of (M1) and behind (M2-M5) the calorimeter system. It is especially important for charmonium final states, as in the analysis of $B^0 \to J/\psi K^0_\mathrm{S}$ decays described in this thesis.

3.4.4 Particle identification technique and performance

Combining the information from both RICH detectors, the calorimeter system, and the muon system a likelihood is calculated to assign PID probabilities to each particle reconstructed in the detector.

Calorimeter PID The calorimeter system's scope is to discriminate between photons, electrons, and neutral pions. Trajectories of reconstructed tracks are extrapolated to the calorimeter system to be associated with charged clusters. ECAL clusters without associated track are treated as photon or π^0 candidates where the shape of the cluster is used to separate the two particle types. Potential Bremsstrahlung photons are recombined with electron tracks downstream of the magnet. Also converted photons—e^+e^- pairs from photon interactions with the detector material—are taken into account.

RICH PID The hadron identification is mainly accomplished by the RICH system. The general principle of the RICH PID of charged particles incorporates the track momentum provided by the tracking system and the opening angle of the cherenkov radiation observed in the RICH as a measure for the particle velocity. As shown in Fig. 3.8 the different particle species show a different behaviour in the momentum-cherenkov-angle plane that can be exploited to identify the particle. Assigning different particle hypotheses the probability of a particle to be of a certain kind are matched using global pattern-recognition.

Muon PID Muon candidates are identified by extrapolating tracks into the muon stations and then looking for a sufficient number of hits in a field of interest depending on the muon momentum. As a rule of thumb it can be assumed that a 6 GeV muon will traverse the full muon system, while a 3 GeV muon candidate will usually be stopped in the third muon chamber.

The global PID likelihood then incorporates the likelihoods of the calorimeter, the RICH, and the muon systems under a certain particle hypothesis. Finally, the likelihood values are calculated relative to the pion hypothesis such that the separation can always be expressed as a decision between two particle types, as

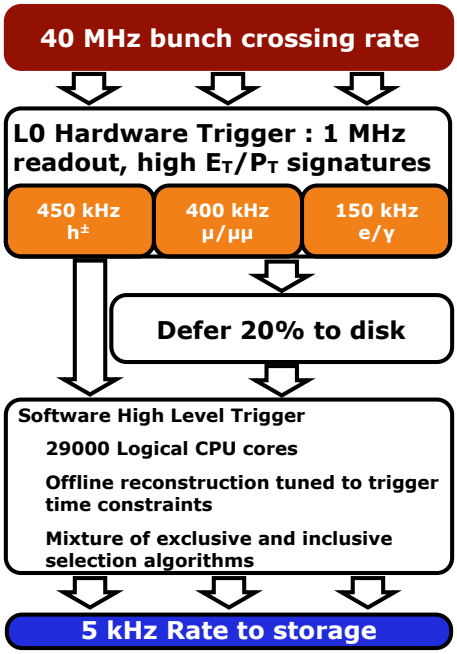

Figure 3.9 – The LHCb Run I trigger scheme. [71]

e.g. the kaon vs. pion probability is given by the likelihood difference $\Delta \ln \mathcal{L}_{K\pi} \equiv \ln \mathcal{L}_K - \ln \mathcal{L}_\pi$ or for proton-kaon separation $\Delta \ln \mathcal{L}_{pK} \equiv \Delta \ln \mathcal{L}_{p\pi} - \Delta \ln \mathcal{L}_{K\pi}$.

The PID is a crucial ingredient to all major analyses based on LHCb data. Thus, the performance of the PID algorithms is optimised for a high identification efficiency and small mis-identification rates. The electron PID efficiency is $\sim 90\,\%$ with an $e-$hadron mis-id probability of $\sim 5\,\%$, kaon PID efficiency is $\sim 95\,\%$ with a $\pi - K$ mis-id probability of $\sim 5\,\%$, and finally the muon PID efficiency is $\sim 97\,\%$ with a $\pi - \mu$ mis-id probability of $\sim 1 - 3\,\%$ [66, 68].

3.5 Trigger

To cope with up to 40 MHz event rate and high particle multiplicities an efficient online event selection (trigger) system is necessary. The LHCb trigger system consists of a hardware trigger (L0) and the HLT (high level trigger) software trigger. The L0 uses custom made electronics located in direct proximity of the readout electronics to provide a fast trigger decision in real-time with the bunch crossing-frequency. The HLT operates asynchronously on a processor farm.

Fig. 3.9 shows an overview of the LHCb trigger schematics. The L0 is described in Sec. 3.5.1 while more information on the HLT can be found in Sec. 3.5.2. Details on the LHCb trigger system and its performance during Run I can be found in Refs. [69, 70].

3.5.1 The hardware trigger

The L0 trigger incorporates information from the VELO pile-up system, the calorimeters, and the muon system to provide a decision in under 4 µs after the bunch crossing. This reduces the read-out rate from the LHC bunch crossing rate of up to 40 MHz to 1 MHz at which the full detector can be read out. The L0 triggers on the highest transverse energy calorimeter clusters and the two muons with the highest p_{T} in the muon system. Additionally global event properties as the number of primary pp interactions estimated by the VELO pile-up system and the number of SPD hits are used to reject events with large combinatorics.

3.5.2 The high level trigger

To further reduce the data rate, the HLT software trigger handles all events that pass the L0. The HLT itself is further split into two stages, the HLT1 and the HLT2. The first stage performs a partial event reconstruction using track information from the VELO, the muon system, and the main tracking stations to accept events with high p_{T} tracks. The second HLT stage then performs a full event reconstruction on the events that passed HLT1. Both HLT stages further reduce the event rate to $3 - 5$ kHz before the data is written to permanent storage.

The HLT excels in its flexibility and performance, especially regarding the selection of (di-)muon events. As the LHC delivers stable physics beams in about 30 % of the time, local storage on the computing nodes is used to 'defer' around 20 % of the L0-passed events to process them during periods without stable beams [72].

3.6 Software stack

The LHCb core software framework Gaudi [73] is used for data processing and supports interfaces to all other software packages. The track reconstruction is performed by Brunel [74] while Moore [75] runs the HLT1 and HLT2 trigger algorithms. Both packages differentiate between data and simulation. The generation of simulated events is managed by the Gauss [76] project in consecutive steps: at first Pythia [77] is used as event generator, then the decay of particles is simulated with EvtGen [78] where radiative corrections are handled by Photos [79]. The transit of particle through the detector and the interaction with matter is simulated with Geant4 [80]. The detector response is finally described by Boole [81] including simulations of electronics noise, detector cross-talk, and spill-over effects. The DaVinci [82] package provides an analysis framework to apply selections and—if available—access Monte Carlo (MC) informations on reconstructed particle tracks.

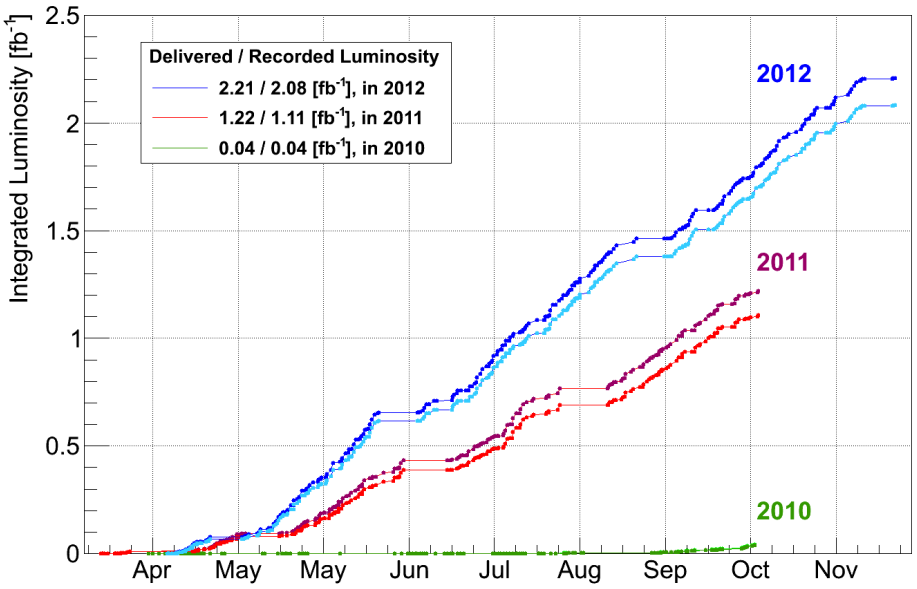

Figure 3.10 – History of delivered and recorded integrated luminosity over the time period of Run I [83].

3.7 Data taking

Over the Run I period from 2010 to 2012 a total integrated luminosity of $3.47\,\text{fb}^{-1}$ was delivered to the LHCb detector by the LHC in pp collisions. The overall data taking efficiency achieved by the experiment was around 93 % for the full run period leading to a recorded integrated luminosity of $3.22\,\text{fb}^{-1}$ in Run I. The main sources of efficiency loss can be found in detector dead time, the data acquisition system, VELO safety measures, and control of the high voltage systems. A detailed overview of the data taking history including delivered and recorded integrated luminosity is depicted in Fig. 3.10.

4 Flavour tagging

The time-dependent measurement of the CP asymmetry $\mathcal{A}_{CP}(t)$ requires the knowledge of the reconstructed B meson's flavour at production, i.e. whether it contained a b or a $\overline{b}$ quark. The method and algorithms used to infer this information from all available event properties are named flavour tagging.

Each tagging algorithm provides a tag d and a probability estimate η that the assigned tag is wrong, also called mistag estimate. The tag is $d = +1$ for an initial B^0, $d = -1$ for an initial $\overline{B}^0$, and $d = 0$ if the tagging algorithms were not able to determine a decision. The mistag estimate interval is given by $[0, 0.5[$, where mistags $\eta' > 0.5$ are evaluated as $\eta = 1 - \eta'$ and the corresponding tag's sign is reversed. If the algorithm is not able to determine a decision, the mistag is set $\eta = 0.5$.

The performance of the flavour tagging algorithms can be assigned using control samples of B mesons whose final state determines the B flavour at decay time (i.e. are flavour-specific), e.g. $B^+ \to J/\psi K^+$ where the charge of the kaon allows to infer the charge of the initial B.

Given the numbers of all rightly tagged B candidates N_{R}, all wrongly tagged candidates N_{W}, and all untagged candidates N_{U}, the tagging efficiency $\varepsilon_{\mathrm{tag}}$ can be assigned

$$\varepsilon_{\mathrm{tag}} = \frac{N_{\mathrm{R}} + N_{\mathrm{W}}}{N_{\mathrm{R}} + N_{\mathrm{W}} + N_{\mathrm{U}}} \,. \tag{4.1}$$

In addition to the mistag estimate, the true underlying fraction of wrongly tagged candidates ω is given by

$$\omega = \frac{N_{\mathrm{W}}}{N_{\mathrm{R}} + N_{\mathrm{W}}} \,. \tag{4.2}$$

The statistically relevant figure of merit for time-dependent measurements of CP violation, the 'effective tagging efficiency'

$$\varepsilon_{\mathrm{eff}} = \varepsilon_{\mathrm{tag}}(1 - 2\omega)^2 = \varepsilon_{\mathrm{tag}} D^2 \,, \tag{4.3}$$

represents the fraction of candidates necessary to reach the same statistical power if the tagging would be perfect, and hence should be maximized to achieve the best performance. The quantity D is called dilution, taking a value of 1 in case of perfect tagging, and 0 in case of random tagging. As described e.g. in Ref. [10, Ch. 10.3] the dilution can be directly translated to the amplitude of the measured CP asymmetry.

In the following sections more details on flavour tagging are provided. A short introduction of the utilized algorithms and a comparison to the flavour tagging

used at lepton colliders is given in Sec. 4.1. In Sec. 4.2 the two different classes of flavour tagging algorithms used at LHCb are presented, while the calibration of the tagging algorithm outputs is described in Sec. 4.3. The combination of the different algorithms' responses into a single decision is outlined in Sec. 4.4. Recent developments are discussed in Sec. 4.5.

More details on the flavour tagging employed by the LHCb collaboration can be found in [84, 85].

4.1 Flavour tagging at BaBar and Belle

Due to the different nature of the experimental setup, the tagging method used at LHCb differs from methods used at the B factories. As described in Sec. 3.2, the b hadron production is dominated by gluon-gluon fusion over a large range of q^2 in contrast to the production at the $\Upsilon(4S)$ $b\bar{b}$ resonance as it was the case at the B factories. The following section gives a résumé of the flavour tagging methods employed by the BaBar and Belle collaborations outlined in Ref. [10, Ch. 8].

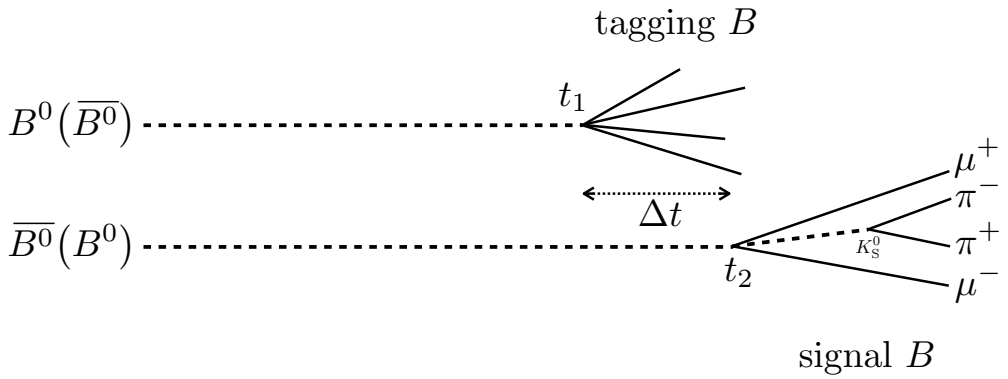

Figure 4.1 – Illustration of the measurement of $\sin(2\beta)$ as conducted by the B factories.

Fig. 4.1 illustrates the basic principles of a CP violation measurement at the B factories. The produced $B^0\overline{B}^0$ pair's wave function is in a P-wave entangled state, until one of the mesons decays. From this point in time (t_1) the second B meson propagates further through the detector, oscillates to its antimatter state, and finally decays at t_2. The CP asymmetry $\mathcal{A}_{CP}(t)$ will therefore be a function of the decay time difference Δt. This has two implications: First, the decay time difference will always be computed relative to the *tagging* B meson decay and thus might be negative if the signal B meson decays first. Secondly, if the tagging B meson decays into a flavour-specific final state, this specifies the signal B meson's flavour at $\Delta t = 0$.

As a result of the production mechanism, the fully reconstructed signal decay leaves all remaining tracks to originate from the tagging B. This allows to classify the decay of the tagging meson according to the signature of the final state particles.

Specialised taggers then identify decays based on their specific signature. In a second stage, all results provided by the single taggers are combined into a final tagging decision.

The lepton taggers deduce a tag from the charge of electrons and muons from $b \to c l^- \overline{\nu}$ transitions in semileptonic B decays. Likewise, second order transitions from $b \to W^- c (\to s l^+ \nu)$ can be used, but have to be handled differently as their charge is opposite compared to primary leptons. Charged kaon candidates from the $b \to c \to s$ decay chain reflect the charge of the tagging meson. Here as well, kaons from second order transitions carry the opposite charge. Charged pions from charm decays work as tagging particles either directly or in events with both a pion and a charged kaon, the correlation of the particles can be utilised to improve the tag decision. Selecting high momentum particles, e.g. fast pions from $\overline{B}^0 \to D^{*+} \pi^-$, is on its own another source of tagging information and might additionally be correlated with slow particles to enhance the tagging result. Finally the flavour of Λ baryons from decays of the tagging B meson can be exploited.

The BaBar experiment uses artificial neural networks (ANNs) for each single tagger to provide several intermediate tagging decisions that are subsequently combined using another ANN to gain a joined tagging decision. The effective tagging efficiency of the final BaBar tagging algorithm is estimated on data to be $\varepsilon_{\text{eff}} = (33.1 \pm 0.3)\,\%$. In Belle analyses the flavour tagging approach is similar. Instead of ANNs multi-dimensional look-up tables are used. At first, information from charged tracks are looked-up to sort them into the signature categories. Next, the results are used on an per-event level to provide the final tagging decision. Using this approach an effective tagging efficiency of $\varepsilon_{\text{eff}} = (30.1 \pm 0.4)\,\%$ is achieved.

4.2 Flavour tagging algorithms

At LHCb several tagging algorithms, each specialized on different characteristics of the underlying event, are used in order to determine the B meson flavour at production. Alongside a tag decision d, each algorithm provides an estimated mistag probability η based on an ANNs response. The algorithms can be classified into two types: the same-side (SS) tagging and opposite-side (OS) tagging algorithms, also called SS/OS taggers. The SS taggers infer the production flavour of the signal B meson by identifying charged candidates that have a high chance of being remnants of its hadronisation process. The OS taggers exploit the dominant production of B mesons through $b\overline{b}$ quark pair production, allowing to partially reconstruct the b hadron produced together with each reconstructed signal B meson and thereby infer its initial flavour. Fig. 4.2 gives an overview of the tagging algorithms used on the opposite-side and same-side.

The tagging algorithms are developed using simulated $B^+ \to J/\psi K^+$ and $B^0 \to D^{*-} \mu^+ \nu_\mu$ decays. In an iterative procedure the selection criteria were optimized in order to maximise the effective tagging efficiency ε_{eff}. The algorithms only consider charged tracks with a good quality of the track fit and momenta above $2\,\text{GeV}/c$.

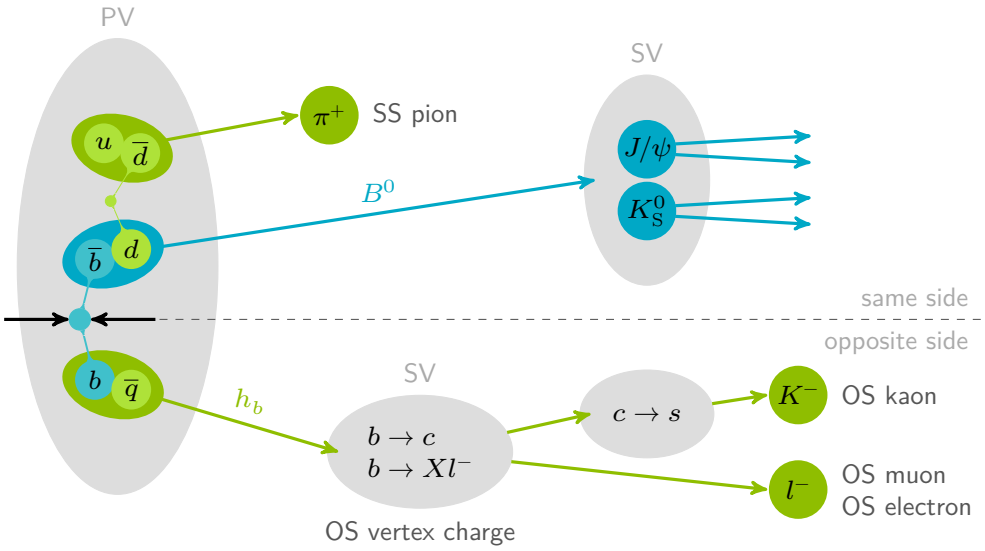

Figure 4.2 – Schematic overview of the used OS and SS tagging algorithms. [43]

Tracks with a polar angle of less than 12 mrad with respect to the beamline are declined. Further on, particles originating from the signal candidate are suppressed by rejecting all tracks that lie inside a cone of 5 mrad around any signal B meson daughter. Tracks from other PVs are eliminated using impact parameter (IP) requirements.

Secs. 4.2.1 and 4.2.2 contain detailed the SS tagging and OS tagging algorithms, also called SS/OS taggers. The SS taggers infer the production flavour of the signal B meson by identifying charged candidates that have a high chance of being remnants of its hadronisation process. On the other hand, the OS taggers exploit the dominant production of B mesons through $b\bar{b}$ quark pair production, allowing to partially reconstruct the b hadron produced together with each reconstructed signal B meson and thereby infer its initial flavour.

4.2.1 Opposite-side algorithms

The OS algorithms all infer the tagging decision from the quark flavour of the b hadron produced in association with the signal B meson. If for example a B^+ decays into a K^+X final state through $\overline{b} \to \overline{c} \to \overline{s}$ transition, it can unambiguously be stated by looking at the kaon charge that the b hadron produced along with the B^+ contained a b quark. The tag identification for events with this signature fall into the scope of the opposite-side kaon (OSK) tagger. In contrast to the SS taggers all OS algorithms are sensitive to an intrinsic mistag due to flavour oscillations of neutral B mesons.

In total, four distinct OS taggers, each developed for a special OS decay signature, provide tagging information. Besides the OSK tagger, the opposite-side electron (OSe) and the opposite-side muon (OSμ) taggers select leptons coming from the

Table 4.1 – Selection requirements for the OSK tagger [87].

Property	Value
p_{T}	$> 0.5\,\mathrm{GeV}/c$
IP	$< 1.25\,\mathrm{mm}$
IP $/\sigma_{\mathrm{IP}}$	> 3.35
track fit χ^2/ndf	< 2.75
$\Delta \ln \mathcal{L}_{K\pi}$	> 6
$\Delta \ln \mathcal{L}_{Kp}$	> -4
IP $/\sigma_{\mathrm{IP}}$ wrt. any PV	> 4.5
reject clone tracks	

primary $b \to cl^-\overline{\nu}$ decay to use their charge as an information carrier of the B flavour. Finally, the opposite-side vertex charge (OSQ_{vtx}) tagger performs an inclusive reconstruction of the OS SV to then compute a weighted sum of all particle track charges that originate from the SV. In the following, the selection criteria and algorithms of the OS taggers are briefly described.

The opposite-side kaon tagger

The kaon tagger exploits the charge of kaons stemming from $b \to c \to s$ decays of the opposite side b hadron. As the charge of the kaon is the same of the ancestor's charge, the kaon always carries the opposite charge as the signal B meson.

To reduce background contributions of prompt kaons and kaons from primary $\overline{b} \to W^+(\to c\overline{s})\overline{c}$ transitions, in which case the kaon carries the 'wrong' charge, several selection criteria are applied. Requirements on the transverse momentum, the impact parameter, the impact parameter fit significance, IP$/\sigma_{\mathrm{IP}}$, and the track fit χ^2/ndf are performed. PID requirements on the $\Delta \ln \mathcal{L}_{K\pi}$ and the $\Delta \ln \mathcal{L}_{Kp}$ suppress mis-identified particles (cf. Sec. 3.4.4). Clone tracks are removed using the Kullback-Liebler criterion [86] and kaon candidates which originate from other PVs are rejected using IP$/\sigma_{\mathrm{IP}}$ requirements with respect to any PV. Tab. 4.1 lists all applied cuts. If more than one tagging candidate is found, the decision obtained from the candidate with the highest p_{T} is chosen. To further increase the effective tagging efficiency only tag decisions are considered if the estimated probability of the tagger to be correct is larger than 0.54.

The opposite-side electron and the opposite-side muon taggers

Leptons from $b \to cW^-(\to l^-\overline{\nu})$ transitions are selected in order to deduce the opposite b hadron charge. Thus positive lepton charge indicates a b quark content of the signal B meson and vice versa.

Cuts on the PID and the lepton p_{T} are applied to reduce the mis-identification rate and to suppress leptons from secondary decays of charm mesons. The muon

Table 4.2 – Selection requirements for the OSe and OSμ taggers [87], where E is the particle energy measured in the ECAL and p the measured particle momentum. Q_{VELO} describes the ionisation charge deposit in the VELO.

Property	Value
lepton p_{T}	$> 1.2\,\mathrm{GeV}/c$
muon $\Delta \ln \mathcal{L}_{\mu\pi}$	> 1
muon track fit χ^2/ndf	< 3.2
reject muon clone tracks and fake muons	
electron $\Delta \ln \mathcal{L}_{e\pi}$	> 4
electron E/p	> 0.8
max. electron Q_{VELO}	< 1.6
electron candidate track in HCAL acceptance	

candidate purity is further enhanced by reducing fake muons, clone tracks, and requiring a sufficient track fit quality. Electron candidate tracks must lie inside the HCAL acceptance and leave a substantial energy deposition in the ECAL compared to their momentum. To reduce backgrounds from photon conversions close to the pp interaction region, an upper limit on the maximal ionisation charge Q_{VELO} deposited in the VELO is set. If more than one lepton candidate passes the requirements, the one with the highest p_{T} is chosen. The selection requirements for the lepton taggers are listed in Tab. 4.2.

The opposite-side vertex charge tagger

Besides the single particle taggers for kaons, muons, and electrons, the OSQ_{vtx} tagger follows an alternative approach by trying to inclusively reconstruct the decay vertex of the opposite b hadron. Starting with a two-track seed, matching tracks are appended and a weighted sum of the vertex charge is calculated. The procedure is optimized using cuts on the considered tracks, the seed properties, and the features of the reconstructed vertex.

The initial vertex seed is found by sampling track pairs from all particle candidates surviving the following criteria: At least one of the tracks must be a long track with a track fit quality of $\chi^2/\mathrm{ndf} < 2.5$. To exclude poor track reconstruction only tracks with an IP (wrt. the PV) uncertainty of $\sigma_{\mathrm{IP}} < 1$ are taken into account. Tracks from prompt particles are rejected if the IP significance $\mathrm{IP}/\sigma_{\mathrm{PV}}$ wrt. the PV is below 2.5 or above 100. Additionally the track has to have a $p_{\mathrm{T}} > 0.15\,\mathrm{GeV}/c$ and an IP $< 3\,\mathrm{mm}$ wrt. the PV. The two seed tracks must be separated by an angle of $\phi > 1\,\mathrm{mrad}$ and one of the tracks has to have a $p_{\mathrm{T}} > 0.3\,\mathrm{GeV}/c$.

For tracks pairs passing all selection criteria a vertex fit is performed. If the fit succeeds and a fit quality of at least $\chi^2/\mathrm{ndf} < 10$ is met, the fitted vertex is considered as a seed. The seed is required to lie inside the detector acceptance and in the forward direction of the PV ($z > 0$).

The invariant mass of the seed is calculated and has to be greater than $0.2\,\mathrm{GeV}/c^2$ and not be compatible with the known K^0_S or Λ^0 masses. A likelihood is computed for all seeds considering the vertex fit χ^2/ndf, the minimum p_T, the maximum PV IP, the minimum PV IP $/\sigma_\mathrm{IP}$, the angle between the seed tracks, the z-distance to PV, and the angle between the seed direction wrt. the PV. The seed with the maximum likelihood is selected. The seed algorithm successfully finds a seed in nearly 50 % of all events and has a rate of 60 % to find a seed that is formed by b hadron decay products.

Subsequently more tracks are added to the seed. Additional tracks are required to be compatible with the reconstructed seed vertex (IP $< 0.9\,\mathrm{mm}$), have a distance of closest approach (DOCA) to any track in the seed smaller than 0.2 mm, the track fit quality is at least $\chi^2/\mathrm{ndf} < 3$, and are unlikely to be a clone track. Additionally, the IP with respect to the PV has to be larger than 0.1 mm and $\mathrm{IP}/\sigma_\mathrm{IP} > 3.5$.

After all tracks are added to the vertex, another set of selection requirements has to be fulfilled to optimize the effective tagging efficiency. The sum of all track momenta has to be $\sum_i p_i > 10\,\mathrm{GeV}/c$ and $\sum_i p_\mathrm{T}(i) > 10\,\mathrm{GeV}/c$, the invariant vertex mass must be greater than $m_\mathrm{vtx} > 0.5\,\mathrm{GeV}/c^2$, the sum of the track $\sum_i \mathrm{IP}_i/\sigma_{\mathrm{IP}_i}$ has to be larger 10 and the sum of the track DOCA has to be $\sum_i \mathrm{DOCA}_i < 0.5\,\mathrm{mm}$.

The tag decision is then deduced from the inclusively reconstructed vertex by calculating the weighted charge for all tracks i forming the vertex

$$Q_\mathrm{vtx} = \frac{\sum_i p_\mathrm{T}^k(i) Q_i}{\sum_i p_\mathrm{T}^k(i)}\,, \tag{4.4}$$

where the track p_T are used as weights and the k parameter is optimised using simulated data to be $k = 0.4$. In a final step, only charges of $|Q_\mathrm{vtx}| > 0.25$ are considered and the mistag probability has to be smaller than 0.46.

4.2.2 Same-side algorithms

The same-side taggers exploit charge information from pions or kaons produced in the hadronisation process of the signal B meson. As illustrated in Fig. 4.2 the $q\overline{q}$ quark pair produced alongside the signal meson, hadronises to form the B meson and in the case of a B^0 (B^0_s) an accompanying pion (kaon). Another potential production mechanism of pions or kaons associated with the signal B meson is in the decay of excited B meson states (cf. [88]).

The same-side pion tagger

The pions from either the B meson hadronisation or the decay of excited states carry the same charge sign as the signal B meson's b quark and are therefore suitable to extract tagging information. The selection criteria for pion candidates are listed in Tab. 4.3. If more than one pion candidate passes the requirements,

Table 4.3 – Selection requirements for the SSπ tagging candidates [87], where ΔQ describes the difference between the $B^0\pi$ and the B^0 invariant mass.

Property	Value
only long track pion candidates	
$\Delta \ln \mathcal{L}_{K\pi}$	< 4.5
$\Delta \ln \mathcal{L}_{p\pi}$	< 15
p_{T}	$> 0.5\,\mathrm{GeV}/c$
p	$> 2.5\,\mathrm{GeV}/c$
PV IP$/\sigma_{\mathrm{IP}}$	< 4
ΔQ	$< 1.5\,\mathrm{GeV}/c^2$

the one with the highest p_{T} is chosen. The tag decision has to have a probability to be correct of at least 0.54 otherwise it will be refused.

The same-side kaon tagger

The charge of kaons produced together with a signal B_s^0 meson can be exploited in order to deduce a tag decision. The selection requirements for kaon candidates are similar to those for the SSπ tagger. Besides PID variables, momenta, the quality of the IP fit and the track fit, differences between the $B_s^0 K$ mass and the B_s^0 mass, the difference in the ϕ angle between the signal B meson and the kaon, and the pseudo-rapidity between the signal B meson and the kaon are taken into account. If more than one candidate passes the criteria, the one with the highest p_{T} is used. The same-side kaon (SSK) tagger is not used in this analysis as only B^0 and $\overline{B}^0$ meson initial states are considered.

4.3 Calibration of the flavour tagging output

The tagging decisions each tagger makes are based on selection criteria developed using simulations and flavour-specific decays. While the tag decision d depends on a measured particle or vertex charge, the mistag estimate η is computed using ANNs trained on sWeighted $B^+ \to J/\psi K^+$ data incorporating kinematic and geometric event properties.

In order to adjust for differences between the training on simulated data and the application on data, the ANN output is calibrated using flavour-specific decays. For the OS taggers and the SSπ tagger, $B^+ \to J/\psi K^+$ decays are used to develop a calibration function $\omega(\eta)$ (while the portion of the data sample that was used to train the ANN before is omitted). Decays of charged B mesons are not subject to quark mixing, thus, the true mistag probability ω can be determined directly by counting and comparing the final state charges. In case of neutral B decays into flavour-specific final states a full time-dependent mixing analysis is necessary.

In Sec. 4.3.1 general concepts and the choice of the calibration function are presented, then the methodologies of a calibration using decays of either charged or neutral B mesons is explained. Two different approaches how to incorporate the per-event tagging information are described and an outlook into the technique of combining different tagger's output into a single tag decision is given. Then the calibration of the OS and the SSπ taggers using $B^+ \to J/\psi K^+$ and $B^0 \to J/\psi K^{*0}$ decays is shown in Secs. 4.3.2 and 4.3.3.

4.3.1 Methodology

The calibration of the flavour tagging output usually follows an iterative procedure. All single taggers and the combination of all OS tagging decisions (see Sec. 4.4) is calibrated using the high yield decay channel $B^+ \to J/\psi K^+$. The correction determined in this step is then applied to the tagging algorithms during the common data processing stage (*stripping*). Afterwards, the calibration is checked on several control channels, i.e. $B^+ \to J/\psi K^+$, $B^+ \to D^0\pi^+$, $B^0 \to J/\psi K^{*0}$, $B^0 \to D^-\pi^+$, $B^0 \to D^{*-}\mu^+\nu_\mu$ and $B_s^0 \to D_s^-\pi^+$ and possible small corrections can be applied for individual analyses. Assuming no correlations amongst the single taggers, it can be assumed, that the calibration is still valid for the combined tagging estimates. This assumption is checked as well.

A linear calibration function $\omega(\eta)$ is chosen with two parameters p_0 and p_1,

$$\omega(\eta) = p_0 + p_1(\eta - \langle\eta\rangle)\,, \tag{4.5}$$

with $\langle\eta\rangle$ being the average mistag estimate introduced to decorrelate p_0 and p_1. Hence, a perfectly calibrated tagging output would result in $p_0 = \langle\eta\rangle$ and $p_1 = 1$. The performance of the tagging algorithms may depend on the flavour of the initial B meson. Different interaction of particles, e.g. kaons used by the OSK tagger, induce deviating reconstruction efficiencies, resulting in different tagging efficiencies ε_{tag} and mistag probabilities ω for initial B^0 and $\overline{B}^0$ states. To correct for asymmetries of the tagging calibration, $\Delta\omega = \omega^{B^0} - \omega^{\overline{B}^0}$, two independent calibration functions are defined

$$\begin{aligned} \omega^{B^0}(\eta) &= p_0^{B^0} + p_1^{B^0}(\eta - \langle\eta\rangle)\,, \\ \omega^{\overline{B}^0}(\eta) &= p_0^{\overline{B}^0} + p_1^{\overline{B}^0}(\eta - \langle\eta\rangle)\,, \end{aligned} \tag{4.6}$$

where the calibration parameters p_i (with $i = 0, 1$) can be parametrised as

$$p_i^{B^0} = p_i + \frac{\Delta p_i}{2} \quad \text{and} \quad p_i^{\overline{B}^0} = p_i - \frac{\Delta p_i}{2}\,. \tag{4.7}$$

Flavour tagging calibration using decays of charged *B* mesons

Using decays of charged B mesons into flavour-specific final states like $B^+ \to J/\psi K^+$ and $B^+ \to D^0\pi^+$ is the straightforward way to calibrate the flavour tagging, as the decisions given by the tagging algorithms can be easily compared to the final state

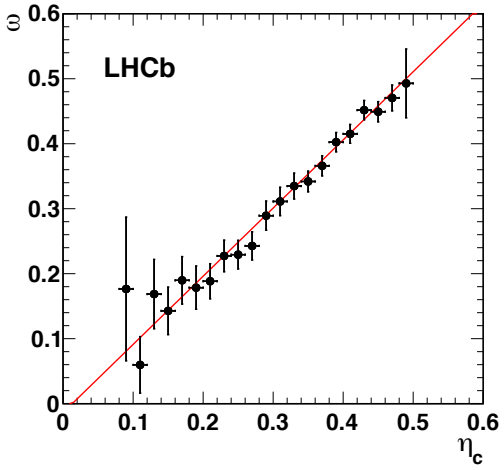

Figure 4.3 – Measured mistag fraction ω plotted against the mistag estimate η provided by the OS tagging algorithms. Described in black are data of $B^+ \to J/\psi K^+$ decays corresponding to an integrated luminosity of $0.37\,\text{fb}^{-1}$. The red line illustrates the linear calibration function fit to the data. [84]

charges. Using a fit to the B^+ mass distribution, signal weights (sWeights) can be computed using the sPlot technique [89]. The mistag estimate distribution can then be split into n bins to compare the average estimated mistag of each bin η_i to the counted mistag ratio ω_i. Fig. 4.3 shows an exemplary calibration plot using a dataset of $B^+ \to J/\psi K^+$ decays corresponding to an integrated luminosity of $0.37\,\text{fb}^{-1}$ [84]. The data is categorised into 21 bins of η and a linear function is fit to the data to estimate the calibration parameters p_0 and p_1.

As an alternative, the calibration function parameters can be estimated through an unbinned maximum likelihood fit to tagging decision, true state, and mistag probability estimate, using a probability density function (PDF) $\mathcal{P}^{\text{Sig}}(d, d', \eta)$, where d' describes the true B^+ tag derived from the final-state particle charge,

$$\mathcal{P}^{\text{Sig}}(d, d', \eta) = \begin{cases} \varepsilon_{\text{tag}}(1 - \omega(\eta))\mathcal{P}^{\text{Sig}}(\eta) & \text{if } d = d' \\ \varepsilon_{\text{tag}}\omega(\eta)\mathcal{P}^{\text{Sig}}(\eta) & \text{if } d \neq d' \\ 1 - \varepsilon_{\text{tag}} & \text{if } d = 0 \end{cases} . \tag{4.8}$$

Flavour tagging calibration using decays of neutral *B* mesons

In the decay of neutral B mesons, the oscillation of the propagating B state prevents the determination of the initial flavour just by measuring the final state charge. Instead, a full decay time dependent mixing analysis has to be performed. As described e.g. in [90], the signal mixing asymmetry is given by

$$\mathcal{A}_{\text{Mix}}(t) = (1 - 2\omega)\cos(\Delta m_d t) . \tag{4.9}$$

This can be either utilised in a simultaneous fit in different bins of η to extract per bin ω_i, then following the same procedure as described for charged initial states or by implementing the calibration function $\omega(\eta)$ directly into the PDF.

Evaluation of systematic uncertainties

In the determination of systematic uncertainties two different causes of errors are considered: 'type I' uncertainties are related to systematic uncertainties from the methodology of the calibration itself, while 'type II' uncertainties account for systematic uncertainties resulting from using the calibration parameters determined in a control channel in the signal channel. The standard type II uncertainties cover for differences between all commonly used control channels, whereas the procedure followed in this analysis differs, as described later on.

4.3.2 Opposite-side tagger calibration using $B^+ \to J/\psi K^+$ decays

Deviating from the standard procedure to calibrate the OS taggers and their combination using a set of physics channels, only $B^+ \to J/\psi K^+$ is used. A previous study [28] made apparent that the type II uncertainties arising from the flavour tagging calibration provide the largest contribution to the overall systematic uncertainties on the measured CP parameters $S_{J/\psi K^0_S}$ and $C_{J/\psi K^0_S}$. Therefore, giving up on semileptonic and fully hadronic decay modes with different kinematic properties and only using $B^+ \to J/\psi K^+$ decays with a nearly similar final state, can reduce these uncertainties. An additional cross-check of the calibration is performed on $B^0 \to J/\psi K^{*0}$ decays to confirm the portability of the calibration on a B^+ to a B^0 initial state.

The calibration then follows the already outlined approach: extracting sWeights by a fit to the B^+ mass distribution, then comparing the true fraction of wrongly tagged candidates to the average mistag estimate in 60 bins of η. The mass model used in the fit is a sum of three Gaussian PDFs with a shared mean to describe the signal shape and an exponential PDF for the background contributions. The fit to the (η_i, ω_i) pairs using Eq. (4.5) yields

$$
\begin{aligned}
p_0^{\mathrm{OS}} &= 0.3815 \pm 0.0011\,(\mathrm{stat}) \pm 0.0015\,(\mathrm{syst.\,type\ I}) \pm 0.0005\,(\mathrm{syst.\,type\ II})\,, \\
p_1^{\mathrm{OS}} &= 0.978\ \ \pm 0.012\ \ (\mathrm{stat}) \pm 0.006\ \ (\mathrm{syst.\,type\ I}) \pm 0.007\ \ (\mathrm{syst.\,type\ II})\,, \\
\langle \eta^{\mathrm{OS}} \rangle &= 0.3786\,, \\
\rho_{p_0,p_1} &= 0.14\,,
\end{aligned}
$$

where ρ_{p_0,p_1} is the statistical correlation between p_0^{OS} and p_1^{OS} [13]. Fig. 4.4 shows the mass distribution and the PDF projection as well as the calibration plot. The asymmetries in the mistag probabilities are determined by repeating the measurement when splitting the data sample into the initial B^0 flavours and

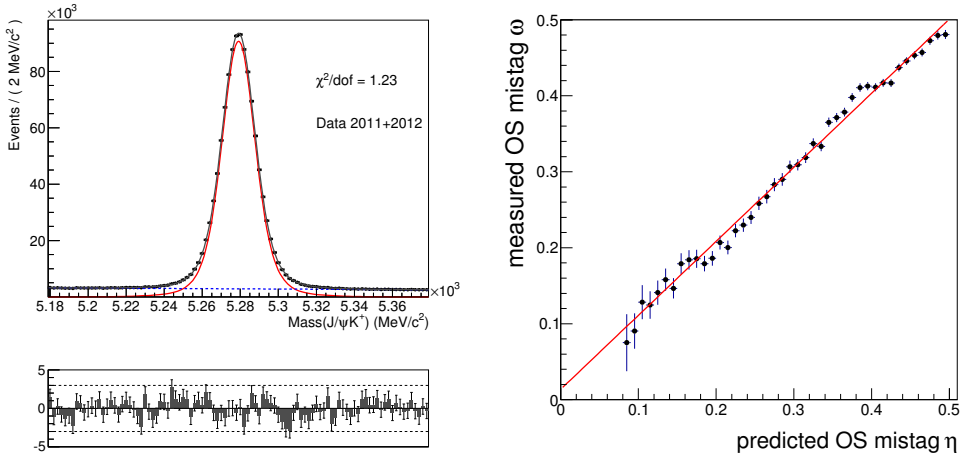

Figure 4.4 – (Left) Distribution of $B^+ \to J/\psi K^+$ mass and projection of the fit PDF. The black solid line shows the total mass PDF, the red solid line the signal and the blue dashed line the background component. (Right) Distribution of (η_i, ω_i) pairs in the decay $B^+ \to J/\psi K^+$ together with the linear calibration function in red. [13]

comparing the values for p_0 and p_1. The results [13] are

$$\begin{aligned}
\Delta p_0^{\mathrm{OS}} &= 0.0148 \pm 0.0016\,(\mathrm{stat}) \pm 0.0007\,(\mathrm{syst.\ type\ I}) \pm 0.0004\,(\mathrm{syst.\ type\ II})\,, \\
\Delta p_1^{\mathrm{OS}} &= 0.070\ \ \pm 0.018\ \ (\mathrm{stat}) \pm 0.003\ \ (\mathrm{syst.\ type\ I}) \pm 0.002\ \ (\mathrm{syst.\ type\ II})\,, \\
\Delta \varepsilon_{\mathrm{tag}}^{\mathrm{OS}} &= \varepsilon_{\mathrm{tag}}^{\mathrm{OS},B^0} - \varepsilon_{\mathrm{tag}}^{\mathrm{OS},\overline{B}^0} = (-0.09 \pm 0.09\,(\mathrm{stat}) \pm 0.09\,(\mathrm{syst}))\%\,.
\end{aligned}$$

As the difference in the tagging efficiencies $\Delta\varepsilon_{\mathrm{tag}}^{\mathrm{OS}}$ is compatible with zero, it is neglected in the following.

The type I systematic uncertainties stem mainly from the method of background subtraction. To study the size of the uncertainties, the model to determine the sWeights is changed, the calibration procedure is repeated, and differences in the results to the nominal determination are considered as a measure of the systematic uncertainties.

To study the type II systematic uncertainties, possible differences between the calibration channel $B^+ \to J/\psi K^+$ and the signal channel $B^0 \to J/\psi K_{\mathrm{S}}^0$ are inspected. Distributions of parameters that are known to influence the tagging algorithms as the transverse momentum (p_{T}), the η, the azimuthal angle (ϕ) of the B meson candidate, and the number of tracks (nTracks) and primary vertices (nPVs) in the event are compared using signal sWeights. The five distributions in the calibration channel are reweighted to match the distribution found in $B^0 \to J/\psi K_{\mathrm{S}}^0$. For each correlated variable the deviation is assigned and the sum in quadrature is taken as systematic uncertainty of type II. The results are summarised in Tab. 4.4.

Table 4.4 – Summary of type II systematic uncertainties for the OS calibration parameters from reweighting the distributions of p_{T}, η, ϕ, and the number of tracks and PVs using signal sWeights. [13]

	δp_0 (10^{-3})	δp_1 (10^{-2})	$\delta\Delta p_0$ (10^{-3})	$\delta\Delta p_1$ (10^{-2})
p_{T}	0.2	0.2	0.2	0.2
η	0.4	0.5	0.2	0.2
ϕ	0.0	0.1	0.3	0.1
nTracks	0.3	0.4	0.1	0.1
nPVs	0.1	0.2	0.2	0.1
Total	0.5	0.7	0.4	0.2
Percentage of stat. uncert.	45.5 %	58.3 %	25.0 %	11.1 %

4.3.3 Same-side tagger calibration using $B^0 \to J/\psi K^{*0}$ decays

The SSπ mistag estimate is pre-calibrated using the calibration parameters

$$p_0 = 0.425\,, \quad p_1 = 0.939\,, \quad \langle\eta\rangle = 0.379. \tag{4.10}$$

Afterwards, the SSπ tagger is calibrated using a dataset of $B^0 \to J/\psi K^{*0}$ decays corresponding to an integrated luminosity of $3.0\,\mathrm{fb}^{-1}$ collected by the LHCb experiment in Run I. As the SSπ tagging algorithm depends on the fragmentation process of the initial B meson, a B^0 decay mode is preferred over a decay of B^+ mesons. Only candidates carrying a tagging response from the SSπ tagger are considered in the following.

To determine the mixing asymmetry $\mathcal{A}_{\mathrm{Mix}}(t)$, a fit to the reconstructed decay time and mass distribution is performed. The signal mass distribution is modelled utilising a Hypatia PDF [91], composed of a generalised hyperbolic core and two-sided tails as introduced by the Crystal ball PDF [92]. A more detailed description of the Hypatia PDF is provided in Sec. 5.6.1. In the present case the tail parameters are fixed to values determined on simulations. The description of the combinatorial background component consists of a sum of two exponential PDFs with shared parameters in the mass dimension to reflect two background components with different lifetimes seen in the decay time dimension. Hence, the background decay time distribution is modelled by two exponential functions as well. The decay time signal PDF contains an acceptance function $\varepsilon(t)$ describing reconstruction and selection inefficiencies for signal candidates with low decay times and a convolution of a B mixing PDF and a resolution model

$$\mathcal{P}_{\mathrm{Sig}} = \varepsilon(t) \cdot \left[\mathcal{P}_{\mathrm{Mix}}(t, d, d') \otimes \mathcal{R}(t - t_{\mathrm{true}})\right]\,, \tag{4.11}$$

with

$$\mathcal{P}_{\mathrm{Mix}}(t, d, d') \propto \mathrm{e}^{-t/\tau}\left(1 - d\,\langle\Delta\omega\rangle + dd'(1 - 2\,\langle\omega\rangle)\cos(\Delta m_d t)\right)\,, \tag{4.12}$$

where the acceptance function is parametrised as

$$\varepsilon(t) = \arctan(t\mathrm{e}^{\alpha t+\beta})\,. \tag{4.13}$$

The resolution model consists of a single Gaussian resolution function $\mathcal{R}(t - t_{\mathrm{true}})$ with the width fixed to 50 fs and no offset from zero. The parameters α and β of the acceptance function are fixed in the fit to values determined on simulated candidates. The mixing PDF depends on the decay time t, the tag decision d of the SSπ tagging algorithm, and the tag d' extracted from the final state flavour (cf. Eq. (4.8)). This parametrisation includes the average mistag difference $\langle\Delta\omega\rangle$ and the average of the mistag $\langle\omega\rangle$ for the given dataset and therefore no per-event mistag information enter the fit model. To strike a balance between the per-event technique outlined in Sec. 4.3.1 and the complexity of the fit model, an intermediate approach is chosen. The calibration is performed by a simultaneous fit in 5 equally filled bins of the mistag estimate η. The per-bin average $\langle\eta\rangle_i$ of all signal candidates is computed using the sPlot method [89]. Then, the calibration can be parametrised inside the PDF

$$\begin{aligned} \langle\Delta\omega\rangle_i &= \Delta p_0 + \Delta p_1(\langle\eta\rangle_i - \langle\eta\rangle)\,, \\ \langle\omega\rangle_i &= p_0 + p_1(\langle\eta\rangle_i - \langle\eta\rangle)\,, \end{aligned} \tag{4.14}$$

with the calibration parameters p_0, p_1, Δp_0, and Δp_1 are shared among all sub-samples of data where $\langle\eta\rangle$ and $\langle\eta\rangle_i$ denote the average mistag estimates for the total dataset and the correspondent sub-samples. Fig. 4.5 presents the mass and decay time distributions of the $B^0 \to J/\psi K^{*0}$ candidates, as well as projections of the fitted PDF components. The calibration parameters are determined to be

$$\begin{aligned} p_0^{\mathrm{SS}\pi} &= 0.4232 \pm 0.0029\,(\mathrm{stat}) \pm 0.0020\,(\mathrm{syst.\,type\ I}) \pm 0.0019\,(\mathrm{syst.\,type\ II}), \\ p_1^{\mathrm{SS}\pi} &= 1.011 \pm 0.064 \,(\mathrm{stat}) \pm 0.009 \,(\mathrm{syst.\,type\ I}) \pm 0.030 \,(\mathrm{syst.\,type\ II}), \\ \Delta p_0^{\mathrm{SS}\pi} &= -0.0026 \pm 0.0043\,(\mathrm{stat}) \pm 0.0024\,(\mathrm{syst.\,type\ I}) \pm 0.0013\,(\mathrm{syst.\,type\ II}), \\ \Delta p_1^{\mathrm{SS}\pi} &= -0.171 \pm 0.096 \,(\mathrm{stat}) \pm 0.029 \,(\mathrm{syst.\,type\ I}) \pm 0.027 \,(\mathrm{syst.\,type\ II}), \\ \langle\eta^{\mathrm{SS}\pi}\rangle &= 0.425, \end{aligned}$$

and the parameter correlations are given in Tab. 4.5 [13]. The type I systematic uncertainties cover influences of the decay time acceptance and resolution, the production and detection asymmetries, as well as possible deviations of the results when performing a fit using a signal sWeighted dataset. The study of the type II systematic uncertainties follows closely the approach outlined in Sec. 4.2.1. The results of the reweighting procedure are presented in Tab. 4.6.

4.4 Combination of single tagger outputs

In order to fully exploit the information of all tagging algorithms it is desirable to combine their tag decisions d_i and mistag estimates η_i into one mutual decision.

Table 4.5 – Statistical correlations between the SSπ tagging calibration parameters. [13]

	$p_0^{\mathrm{SS}\pi}$	$p_1^{\mathrm{SS}\pi}$	$\Delta p_0^{\mathrm{SS}\pi}$	$\Delta p_1^{\mathrm{SS}\pi}$
$p_0^{\mathrm{SS}\pi}$	1	0.04	-0.007	0.0004
$p_1^{\mathrm{SS}\pi}$	0.04	1	0.0016	-0.006
$\Delta p_0^{\mathrm{SS}\pi}$	-0.007	0.0016	1	0.03
$\Delta p_1^{\mathrm{SS}\pi}$	0.0004	-0.006	0.03	1

Table 4.6 – Summary of type II systematic uncertainties for the SSπ calibration parameters from reweighting the distributions of p_{T}, η, ϕ, and the number of tracks and PVs using signal sWeights. [13]

	δp_0 (10^{-3})	δp_1 (10^{-2})	$\delta\Delta p_0$ (10^{-3})	$\delta\Delta p_1$ (10^{-2})
p_{T}	1.3	2.1	0.6	2.7
η	0.23	0.020	0.7	0.5
ϕ	0	0.6	0.14	0.27
nTracks	1.5	2.0	1.1	0.08
nPVs	0.6	0.5	0	0.05
Total	1.9	3.0	1.3	2.7
Percentage of stat. uncert.	65.5 %	46.9 %	30.2 %	28.1 %

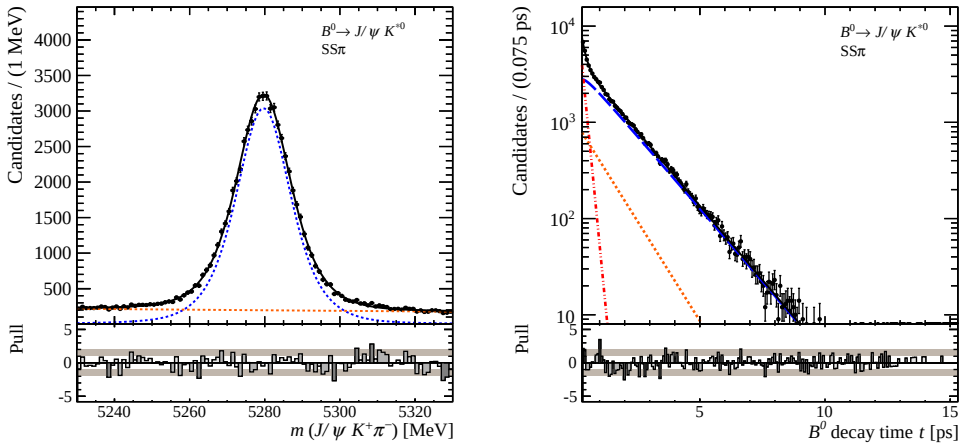

Figure 4.5 – (Left) Mass and (Right) decay time distributions of $B^0 \to J/\psi K^{*0}$ candidates. In blue the projections of the fitted signal components and in red/orange the projections of the combinatorial background components are shown. [13]

Given the probabilities $p(b)$ and $p(\bar{b})$ that a meson contains a b or a $\bar{b}$ quark

$$\begin{aligned} p(b) &= \prod_i \left(\frac{1+d_i}{2} - d_i(1-\eta_i) \right) , \\ p(\bar{b}) &= \prod_i \left(\frac{1-d_i}{2} + d_i(1-\eta_i) \right) , \end{aligned} \tag{4.15}$$

the combined probabilities $P(b)$ and $P(\bar{b})$ can be calculated

$$P(b) = \frac{p(b)}{p(b)+p(\bar{b})} , \quad P(\bar{b}) = 1 - P(b) . \tag{4.16}$$

Then, the combined tag decision and mistag estimate are $d = +1$ and $\eta = 1 - P(\bar{b})$ if $P(\bar{b}) > P(b)$, otherwise $d = -1$ and $\eta = 1 - P(b)$. As Eq. (4.15) ignores possible correlation among the involved taggers, the joint mistag estimate might over- or underestimate the true mistag. To correct for this the mistag estimates as well have to be calibrated after the single tagger combination using a flavour-specific control channel.

The analysis presented in this thesis utilises the combination of the calibrated OS tagging algorithms (see Sec. 4.3.2) as well as of the SSπ tagger (see Sec. 4.3.3). As the OS and SS taggers find their decisions using independent particle information their output is assumed to be uncorrelated and no further calibration is necessary after combining the OS and SSπ tagging decisions (cf. Sec. 5.6.2).

4.5 Recent developments and Run II

The algorithms utilised in the flavour tagging are always subject of active development with the aim to improve their performance and extend the tagging strategy. Several taggers are being revisited using particle selections based on ANNs or boosted decision trees (BDTs).

A BDT based SSπ tagging algorithm (SSπ BDT) is in the stage of early development, intended to replace the existing cut-based SSπ tagger in the future.

For both the OSK and the SSK tagging algorithms ANN based versions are implemented (NNetOSK and NNetSSK) [88].

The performance of the NNetSSK tagger shows a significant enhancement compared to the cut-based SSK implementation. In the $B_s^0 \to D_s^- \pi^+$ channel an effective tagging efficiency of $\varepsilon_{\text{eff}} = (1.80 \pm 0.23)\,\%$ is found, while in selected $B_s^0 \to J/\psi\phi$ candidates $\varepsilon_{\text{eff}} = (1.26 \pm 0.17)\,\%$ is measured. This corresponds to an improvement of more than 40 % in both cases.

The NNetOSK tagger also shows an enhancement in the effective tagging efficiency of around 10 % in decays of $B^0 \to D^- \pi^+$ with respect to the cut-based OSK tagger. Still, more development effort is needed here, as the overall efficiency gain is still small and the improvements can not be confirmed yet in B_s^0 decays.

The study of opposite side decays of charm hadrons has lead to the development of the opposite-side charm (OSc) tagger [93]. The OSc algorithm exploits the charge of charm hadrons or its daughter kaons produced in the decay of opposite side b hadrons. Candidates are identified using a set of multivariate selections of fully or partially reconstructed Cabibbo-favoured decays, as e.g. $D^0 \to K^- \pi^+$, $D^+ \to K^- \pi^+ \pi^+$, $D^0/D^+ \to K^- e^+ X$, or $\Lambda_c^+ \to p K^- \pi^+$.

The performance of the OSc tagger is studied on data using selected $B^+ \to J/\psi K^+$ candidates where an effective tagging efficiency of $\varepsilon_{\text{eff}} = (0.30 \pm 0.01\ (\text{stat}) \pm 0.01\ (\text{syst}))\%$ is found. A cross-check on selected $B^0 \to J/\psi K^{*0}$ candidates provides compatible results with an effective tagging efficiency of $\varepsilon_{\text{eff}} = (0.30 \pm 0.03\ (\text{stat}) \pm 0.01\ (\text{syst}))\%$. Fully-hadronic final states show a better performance: effective tagging efficiencies of $\varepsilon_{\text{eff}} = (0.40 \pm 0.02\ (\text{stat}) \pm 0.01\ (\text{syst}))\%$ and $\varepsilon_{\text{eff}} = (0.39 \pm 0.03\ (\text{stat}) \pm 0.01\ (\text{syst}))\%$ are found for $B^0 \to D^- \pi^+$ and $B_s^0 \to D_s^- \pi^+$ candidates. As the OSc decisions are highly correlated with the OSK output, only an additional 0.113 % absolute gain in effective tagging efficiency can be observed once the full OS combination is computed, still that compares to a month worth of Run I data taking.

Similar to the SSπ or SSK algorithms a newly developed same-side proton tagger infers its tagging decision from protons produced in the fragmentation of the signal B meson.

Alongside new developments and optimisation of existing tagging algorithms the performance of the flavour tagging will be affected by altered experimental conditions in Run II of the LHC. The higher centre-of-mass energy of $\sqrt{s} = 13\,\text{TeV}$ leads to higher particle momenta, resulting in a better selection of the particles involved in the tagging, thus leading to a higher performance of the flavour tagging.

Though, this will also result in higher track multiplicities, impeding the selection, thus reducing the efficiency of the involved algorithms. However, the higher peak luminosity due to the increased centre-of-mass energy, allows for an extensive luminosity levelling which itself will result in an effect the opposite of what was described before, in a reduction of track multiplicities.

It can be summarised that the change in run conditions will force a reoptimisation and recalibration of the flavour tagging algorithms. Studies on MC simulated data with Run II conditions just started and data taken in the first months of Run II will be employed to study the performance and retune the algorithms to be ready as soon as the CP violation and B oscillation measurements are started. It is clear that with higher statistics available in all physics and control channels, systematic effects will need to be even better understood, thus making a universal calibration not feasible any more.

5 The measurement of sin(2β)

5.1 Overview of the measurement ingredients

The measurement of CP violation in the decay of $B^0 \to J/\psi K^0_S$ poses a variety of challenges to the experimenter. Great demands on the vertex resolution, the decay time resolution, PID, and the trigger have to be fulfilled by the LHCb detector as was outlined in Sec. 3.2.

In the analysis an emphasis has to be placed especially on the identification of the initial B meson flavour, the so called flavour tagging, that is explained in more detail in Ch. 4.

This chapter summarises the measurement of the CP parameters $S_{J/\psi K^0_S}$ and $C_{J/\psi K^0_S}$. Starting with an overview of the data in use, including data taking, trigger strategy, candidate selection and employment of simulated data (Sec. 5.2) a short round-up of the flavour tagging strategy is provided (Sec. 5.3).

Possible troublesome influences from mis-reconstructed or mis-identified physical background contributions are studied in Sec. 5.4. The decay time resolution model is described in Sec. 5.5 together with the parametrisation of the decay time acceptance caused by reconstruction and selection inefficiencies. The utilised likelihood function is presented in Sec. 5.6 before showing the results of the fit in Sec. 5.7. Finally, all studies on the systematic influences of a variety of effects are collected in Sec. 5.8.

5.2 Data preparation

This section describes the data employed in this analysis, summarises the different signal candidate selection steps, as well as the handling of multiple PVs and B meson candidates. Finally the different data samples used in the analysis are stated.

The presented analysis is performed on a dataset collected by the LHCb experiment during two run periods in 2011 and 2012, dubbed 'Run I'[1]. The 2011 subsample corresponds to an integrated luminosity of $(1.00 \pm 0.04)\,\mathrm{fb}^{-1}$ collected at a centre-of-mass energy of $\sqrt{s} = 7\,\mathrm{TeV}$, while the 2012 subsample corresponds to an integrated luminosity of $(1.990 \pm 0.024)\,\mathrm{fb}^{-1}$ collected at $\sqrt{s} = 8\,\mathrm{TeV}$.

The $B^0 \to J/\psi K^0_S$ decay candidates are reconstructed in the $J/\psi \to \mu^+\mu^-$ and $K^0_S \to \pi^+\pi^-$ final state. In order to enhance the purity of the signal candidates, several selection steps are performed. At first a two-layer trigger system selects

[1] In contrast to the second 'Run II' period scheduled to start in 2015 and last until mid 2018.

events from the *pp* collisions (cf. Sec. 5.2.1). Then a loose and very general selection, the so called *stripping* is applied to the triggered data (cf. Sec. 5.2.2). The final step is an offline selection of the remaining candidates that is further adjusted to the specific decay and the reconstructed final state (cf. Sec. 5.2.3).

Besides reducing the background level and enhancing the fraction of signal in the data set, the selection tries to minimise a possible bias of the measured B^0 lifetime caused by selection steps that preferably remove candidates with small decay times. As it is inevitable, then at least the biasing effects should be understood and accounted for (cf. Sec. 5.5.2).

Global decay chain fit

In order to correctly comprise correlations and uncertainties on vertex positions, particle momenta, flight distances, decay times, and invariant masses, a global decay chain fit (DTF) [94] is performed. Instead of fitting 'leaf-by-leaf' starting from the final state particles to determine the parameters of all composite mother particles one after another, the DTF fit extracts all parameters in the decay chain simultaneously.

Entities decorated with the expression $\mathrm{DTF}_{\mathrm{PV}}$ stem from a DTF fit where the knowledge about the PV has been used to constrain the production vertex of the B^0 meson, while the expression $\mathrm{DTF}_{\mathrm{PV}}^{J/\psi K^0_{\mathrm{S}}}$ means that, additionally to this PV, the J/ψ and K^0_{S} invariant masses are constrained to their masses listed by the Particle Data Group (PDG) ($m^{\mathrm{PDG}}_{K^0_{\mathrm{S}}} = 497.614\,\mathrm{MeV}/c^2$, $m^{\mathrm{PDG}}_{J/\psi} = 3096.916\,\mathrm{MeV}/c^2$, see [33]) inside the DTF fit. In the stripping and if not stated otherwise the much simpler leaf-by-leaf fitting was used.

Observables

Throughout the analysis, several observables are used: the B^0 invariant mass $m_{J/\psi K^0_{\mathrm{S}}}$, the decay time of the B^0 in its rest frame t, the B^0 decay time error estimate σ_t, and the tag decisions $d_{\{\mathrm{OS,SS}\pi\}}$ and mistag estimates $\eta_{\{\mathrm{OS,SS}\pi\}}$ of the opposite site and same side tagging algorithms (cf. Ch. 4). Tab. 5.1 summarises all used observables, provides the considered observable ranges, and defines the used fit constraints.

Data set subsamples

Year The data consists of subsamples from data-taking in both, 2011 and 2012, run periods. To differentiate between these samples, they are indicated by the terms **11** and **12**.

Track type Due to the long lifetime of the K^0_{S}, its daughter pions may or may not leave hits in the VELO (cf. Sec. 3.3.3). K^0_{S} candidates (and accordingly the associated B meson candidate) of which both reconstructed pions have hits in the VELO are classified as *long track* (**LL**) candidates. If both pions do

Table 5.1 – Used observables, observable ranges, and DTF fit properties.

Name	Range	Fit constraints		
		$m_{K^0_S}^{\text{PDG}}$	$m_{J/\psi}^{\text{PDG}}$	PV position
$m_{J/\psi K^0_S}$	$5230 - 5330\,\text{MeV}/c^2$	✓	✓	✓
t	$0.3 - 18.3\,\text{ps}$	-	-	✓
σ_t	$0.0 - 0.2\,\text{ps}$	-	-	✓
d_{OS}	$+1, -1$	-	-	-
η_{OS}	$0.0 - 0.5$	-	-	-
$d_{\text{SS}\pi}$	$+1, -1$	-	-	-
$\eta_{\text{SS}\pi}$	$0.0 - 0.5$	-	-	-

not leave hits in the VELO, the candidate is called *downstream track* (**DD**) candidate. Candidates where only one or less of the reconstructed pions has a long track are not considered in this analysis.

Tagger Depending on the tag decisions, events are categorised: as exclusively *opposite side tagged* (**OS**) if **only** the opposite side tagger combination returns a tag decision, as exclusively *same side pion tagged* (**SS**) if **only** the same side pion tagger returns a decision, as tagged by both tagging algorithms (or *tagged by both sides* (**BS**)), and as *untagged* (**UT**) if none of the used taggers returns a tag decision. See Ch. 4 for an elaborated description of the flavour tagging methods.

Trigger As described in Sec. 5.2.1, the different trigger lines induce decay time acceptance effects. To describe these effects independently the data is split into a sample where almost no decay time acceptance effects are visible, called *almost unbiased* subsample (**AU**), and a sample that includes the major fraction of events, affected by a decay time acceptance, called *exclusively biased* subsample (**EB**).

Unless explicitly stated otherwise, no untagged (**UT**) events are used. Therefore, splitting the data set in all possible categories results in a total of 24 disjoint subsamples.

5.2.1 Trigger

The LHCb trigger system reduces the amount of data to be stored using loose criteria to filter events with interesting physical signatures. As described in Sec. 3.5 a two-stage system is utilised build up from the fast hardware trigger (L0) and the software based high level trigger (HLT).

The trigger requirements are collected in so called *trigger lines*, consisting of a set of selections criteria to map certain event types. In the following the trigger requirements applied in this measurement are described. If not stated otherwise

Table 5.2 – HLT1 J/ψ muon lines and their requirements. [69]

	`DiMuonHighMass`	`TrackMuon`
Track IP	-	$> 0.1\,\mathrm{mm}$
Track χ^2_{IP}	-	> 16
Track p_{T}	$> 0.5\,\mathrm{GeV}/c$	$> 1\,\mathrm{GeV}/c$
Track p	$> 6\,\mathrm{GeV}/c$	$> 8\,\mathrm{GeV}/c$
Track χ^2/ndf	< 4	< 2
DOCA	$< 0.2\,\mathrm{mm}$	-
χ^2_{vtx}	< 25	-
Mass	$> 2.7\,\mathrm{GeV}/c^2$	-

all candidates passing the requirements specified by the trigger line configuration `(Hlt1DiMuonHighMass || Hlt1TrackMuon) && Hlt2DiMuonDetachedJPsi` are used in this analysis.

Both the HLT1 `TrackMuon` as well as the HLT2 `DiMuonDetachedJPsi` line require cuts on parameters depending on the candidates' measured decay time, preferably removing candidates with small decay times. This leads to a bias on the experimentally accessible lifetime. Candidates are split into two disjoint subsamples: candidates passing the requirements given by the trigger line configuration `DiMuonHighMass && DiMuonDetachedJPsi` are classified as *almost unbiased* (**AU**) where else candidates passing the requirements given by the combination `(TrackMuon && !DiMuonHighMass) && DiMuonDetachedJPsi` correspond to the *exclusively biased* subsample (**EB**). The strategy to cope with acceptance effects is described in detail in Sec. 5.5.2.

L0 trigger requirements

The HLT lines in use require all candidates to either pass the `L0Muon` or the `L0DiMuon` trigger lines, i.e. show one or two high transverse momentum tracks in the five muon stations. No further L0 criteria are required.

HLT1 trigger requirements

All candidates accepted by the two HLT1 trigger lines are required to carry a J/ψ 'trigger on signal' (TOS) decision, where TOS refers to events where the signal particle tracks alone fulfil the trigger line requirements. Both lines are designed to trigger on muons, in this case originating from the secondary decay of the J/ψ into $\mu^+\mu^-$. The HLT1 `TrackMuon` introduces a bias on the lifetime through a cut on the minimal muon track IP with respect to any PV and is therefore called a *biased* line. The HLT1 `DiMuonHighMass` does not affect the decay time distribution, hence is called an *unbiased* line. All trigger requirements are summarised in Tab. 5.2.

Table 5.3 – HLT2 J/ψ dimuon lines and their requirements[§]. [69]

	`DiMuonJPsi`	`DiMuonDetachedJPsi`
Track χ^2/ndf	< 5	< 5
Mass	$M_{J/\psi} \pm 0.12\,\mathrm{GeV}/c^2$	$M_{J/\psi} \pm 0.12\,\mathrm{GeV}/c^2$
flight distance χ^2	-	> 9
χ^2_{vtx}	< 25	< 25
Pre-scale	0.2	-

[§] With $M_{J/\psi} = 3096.916\,\mathrm{MeV}/c^2$ [33].

Table 5.4 – Trigger selection efficiencies as determined on (simulated) data. The first column gives the numbers obtained on $B^0 \to J/\psi K^0_{\mathrm{S}}$ signal MC, where the normalisation is performed wrt. events that pass at least one physics trigger line in the L0, the HLT1, and the HLT2. The second column shows *signal in data* numbers obtained using an sWeighted data sample. The last column contains numbers extracted from data without distinction between signal and background.

trigger requirements	signal MC	signal in data	overall data
`Hlt1DiMuonHighMass && Hlt2DiMuonDetachedJPsi`	70.3 %	72.3 %	60.9 %
`(Hlt1DiMuonHighMass || Hlt1TrackMuon ) && Hlt2DiMuonDetachedJPsi`	84.7 %	86.6 %	74.6 %
Difference between trigger requirements	14.4 pp	14.3 pp	13.7 pp
Relative gain from adding `Hlt1TrackMuon`	+20.4 %	+19.7 %	+22.5 %

HLT2 trigger requirements

The HLT2 trigger line requirements are summarised in Tab. 5.3. Again a TOS decision is required for events passing the trigger selection. Induced by a cut on the flight distance significance of the J/ψ candidate the HLT2 `DiMuonDetachedJPsi` line causes a lifetime bias. Hence, the HLT2 `DiMuonJPsi` line is used as an unbiased reference line. With a pre-scale of 0.2, only 20 % of all events passing L0 and HLT1 are chosen randomly as input to this line.

Trigger efficiencies

The ratio of events passing a trigger requirement compared to all events within the geometrical detector acceptance is called trigger efficiency. Compared to the efficiency of the $1\,\mathrm{fb}^{-1}$ LHCb analysis [28], where events had to fulfil the trigger requirements of the introduced unbiased HLT1 line and the biased HLT2 line, a gain of 19.7 % in signal efficiency is measured by additionally accepting events that pass the requirements defined by the biased HLT1 muon line. Tab. 5.4 compares the calculated trigger efficiencies in detail.

5.2.2 Stripping

To further reduce the amount of data a loose selection is applied in a common effort, called the *stripping* of data. Criteria on the properties of the reconstructed final state particles as well as on the reconstructed J/ψ, K^0_S, and B^0 candidates are applied as described in detail in Tab. 5.5. Two different stripping configurations, the `BetaSBd2JpsiKsDetached` and `BetaSBd2JpsiKsPrescaled` lines are employed. In the *CP* violation measurement the `BetaSBd2JpsiKsDetached` line is used, where a cut requires the B^0 candidate's decay time to be larger than 0.2 ps. For studies requiring the full decay time range, the `BetaSBd2JpsiKsPrescaled` line with a pre-scale of 0.3 is used.

Besides the decay time cut in the detached line and the pre-scale in the corresponding line, all other selection criteria are shared among both lines.

5.2.3 Offline selection

The final step in the selection of signal candidates follows the trigger and stripping selection. The *offline* selection attempts to enhance the signal purity of the data sample without introducing additional biases on the B^0 candidates' decay time distribution. The major objective of the selection is to preserve a large number of signal candidates while the reduction of background candidates only serves an inferior standing. This approach is promoted by the fact, that the physics backgrounds are well under control (cf. Sec. 5.4) and the combinatorial background is easy to model in the fit (cf. Sec. 5.6).

To measure the signal efficiency ε_{Sig} and the background rejection $1-\varepsilon_{\text{Bkg}}$ of the respective selection requirements an sPlot fit [89] has been performed to retrieve signal and background weights for each event. The fit describes the signal using a Hypatia PDF (cf. Sec. 5.6.1) with double sided tails and the background using a single exponential PDF. In case of the LL sample an additional Gaussian PDF with fixed mean and width estimated from MC simulations is used to describe the $B^0 \to J/\psi K^{*0}$ component. For a more detailed description of the used mass model, see Sec. 5.6.1.

Fig. 5.1 shows the mass distribution of the 2011 and 2012 data set and the fit projection. The data set includes all candidates that pass the nominal trigger and stripping. Only the PV with the smallest IP χ^2/ndf wrt. the B^0 trajectory is included and—in case of multiple B^0 candidates—a random B^0 candidate is chosen. Please note that all offline selection efficiencies are calculated individually for each cut or cut ensemble with respect to the candidate numbers passing the stripping selection. The total efficiency is then provided in Sec. 5.2.3.

Sanity cuts

A set of sanity cuts (see Tab. 5.6) is applied to remove outliers and ensure that all DTF fits are converged. The overall performance shows a signal efficiency of

Table 5.5 – Stripping cuts applied in the reconstruction and selection of the J/ψ, the K^0_S, and the B^0 candidates[§].

	J/ψ candidate[†]
μ $\Delta \ln \mathcal{L}_{\mu\pi}$	> 0
μ momentum	$> 0.5\,\mathrm{GeV}/c$
$\mu\mu$ χ^2_{DOCA}	< 20
$m_{\mu\mu}$	$M^{\mathrm{PDG}}_{J/\psi} \pm 80\,\mathrm{MeV}/c^2$
J/ψ χ^2_{vtx}/ndf	< 16
	K^0_S candidate[‡]
π momentum	$> 2\,\mathrm{GeV}/c$
π min χ^2_{IP} wrt. any PV	> 4 for DD > 9 for LL
$\pi^+\pi^-$ χ^2_{DOCA}	< 25
$m_{\pi\pi}$	$M^{\mathrm{PDG}}_{K^0_S} \pm 80\,\mathrm{MeV}/c^2$ for DD $M^{\mathrm{PDG}}_{K^0_S} \pm 50\,\mathrm{MeV}/c^2$ for LL
$m_{K^0_S}$	$M^{\mathrm{PDG}}_{K^0_S} \pm 64\,\mathrm{MeV}/c^2$ for DD $M^{\mathrm{PDG}}_{K^0_S} \pm 35\,\mathrm{MeV}/c^2$ for LL
K^0_S χ^2_{vtx}/ndf	< 20
K^0_S best PV decay length significance	> 5
	B^0 candidate
B^0 χ^2_{vtx}/ndf	< 10
m_{B^0}	$5150\,\mathrm{MeV}/c^2 < m_{\mu\mu\pi\pi} < 5550\,\mathrm{MeV}/c^2$

[§] With $M^{\mathrm{PDG}}_{J/\psi} = 3096.916\,\mathrm{MeV}/c^2$ and $M^{\mathrm{PDG}}_{K^0_S} = 497.614\,\mathrm{MeV}/c^2$ [33].

[†] The requirements on the muon daughters are based on their momenta, their PID information, the χ^2 of their distance of closest approach, χ^2_{DOCA}, and their invariant mass prior to the vertex fit, $m_{\mu\mu}$. After the vertex fit, requirements on the resulting J/ψ candidate are based on its invariant mass, $m_{J/\psi}$, and the χ^2/ndf of the vertex fit, χ^2_{vtx}/ndf.

[‡] The requirements on the pion daughters are based on their momenta, their minimal IP χ^2 wrt. to all PVs in the event, χ^2_{IP}, the χ^2 of their distance of closest approach, χ^2_{DOCA}, and their invariant mass prior to the vertex fit, $m_{\pi\pi}$. After the vertex fit, requirements on the resulting K^0_S candidate are based on its invariant mass, $m_{K^0_S}$, its decay length significance with respect to its best PV, i.e. the PV with the smallest IP χ^2 wrt. to its trajectory, and the χ^2/ndf of the vertex fit, χ^2_{vtx}/ndf.

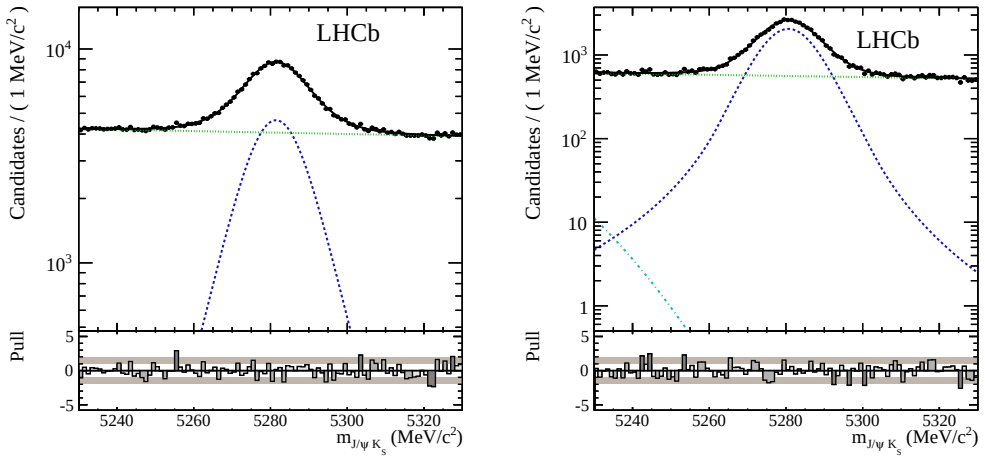

Figure 5.1 – Mass distribution of the combined 2011 and 2012 data set after stripping (in logarithmic scale). Only the PV with the smallest IP χ^2/ndf wrt. the B^0 trajectory is included and— in case of multiple B^0 candidates—a random B^0 candidate is chosen. The left plot shows the DD, the right one the LL candidates. The solid black line is the projection of the fit PDF, the blue dashed line shows the signal, and the green dashed line shows the background component. For the description of the LL candidates, the additional $B^0 \to J/\psi K^{*0}$ component is depicted as dash-dotted turquoise line. Below the mass distribution the pull distribution shows the difference of the bin content and the PDF value at the bin centre normalized by the error estimate on the bin content.

Table 5.6 – Offline selection sanity cuts.

$\mathrm{DTF}_{\mathrm{PV}}^{J/\psi K_{\mathrm{S}}^0}$ σ_m	$< 30\,\mathrm{MeV}/c^2$
$\mathrm{DTF}_{\mathrm{PV}}$ σ_t	$< 0.2\,\mathrm{ps}$
$\lvert z_{PV}\rvert$	$< 250\,\mathrm{mm}$
B^0 $\chi^2_{\mathrm{vtx}}/\mathrm{ndf}$	< 10
J/ψ $\chi^2_{\mathrm{vtx}}/\mathrm{ndf}$	< 16
K_{S}^0 $\chi^2_{\mathrm{vtx}}/\mathrm{ndf}$	< 20
$\mathrm{DTF}_{\mathrm{PV}}$ μ p_T	$> 500\,\mathrm{MeV}/c$
μ $\chi^2_{\mathrm{track}}/\mathrm{ndf}$	< 3
μ PID	> 0
$\mathrm{DTF}_{\mathrm{PV}}$ π p	$> 2000\,\mathrm{MeV}/c$
maximal π $\chi^2_{\mathrm{track}}/\mathrm{ndf}$	< 3
minimal π IP χ^2/ndf	> 4
$\mathrm{DTF}_{\mathrm{PV}}^{J/\psi K_{\mathrm{S}}^0}$ fit and $\mathrm{DTF}_{\mathrm{PV}}$ fit converged	

Table 5.7 – Offline selection cuts on ghost track probabilities.

	DD	LL
μ ghost track probability	< 0.2	
π ghost track probability	< 0.3	

99.29 % (99.75 %) and a background rejection of 6.18 % (0.75 %) in the DD (LL) sample.

Ghost track probability cuts

To reduce the amount of ghost tracks, a cut on each tracks ghost probability is applied, as shown in Tab. 5.7. The overall signal efficiency yields 95.72 % (98.09 %) with a background rejection of 26.38 % (23.36 %) for the DD (LL) sample.

Cuts on daughter masses and Λ mass veto

Background contributions due to particle mis-ID (cf. Sec. 5.4) are reduced by employing cuts on the invariant daughter masses as given in Tab. 5.8. As long track candidates show a better mass resolution, different cuts are applied depending on the candidates' track type. These cuts yield a signal efficiency of 98.70 % (98.92 %) and a background rejection of 27.53 % (39.78 %) in the DD (LL) sample. The cuts correspond to roughly eight times (four times) the measured K_{S}^0 width for DD (LL) K_{S}^0 candidates and around five times the measured J/ψ width for the J/ψ candidates.

To reduce proton-pion mis-ID from background $\Lambda_b^0 \to J/\psi\Lambda$ decays all pion candidate pairs are combined, assigning the proton mass hypothesis to either one

Table 5.8 – Offline selection cuts on the J/ψ and K^0_S candidates' invariant mass[§].

	DD	LL
$m_{\pi\pi}$	$M^{\mathrm{PDG}}_{K^0_S} \pm 55\,\mathrm{MeV}/c^2$	$M^{\mathrm{PDG}}_{K^0_S} \pm 15\,\mathrm{MeV}/c^2$
$m_{\mu\mu}$	$M^{\mathrm{PDG}}_{J/\psi} \pm 60\,\mathrm{MeV}/c^2$	

[§] With $M^{\mathrm{PDG}}_{J/\psi} = 3096.916\,\mathrm{MeV}/c^2$ and $M^{\mathrm{PDG}}_{K^0_S} = 497.614\,\mathrm{MeV}/c^2$ [33].

of the pions and recalculating their invariant mass. An additional requirement on the p-π PID of $\Delta \ln \mathcal{L}_{p\pi} < 7$ (< 10) is then applied to all candidates lying inside a $\pm 7\,\mathrm{MeV}/c^2$ ($\pm 5\,\mathrm{MeV}/c^2$) region around the mass $M^{\mathrm{PDG}}_{\Lambda} = 1115.683\,\mathrm{MeV}/c^2$ in the DD (LL) sample. This veto has a signal efficiency of 99.32 % (99.9 %) and a background rejection of 10.50 % (2.53 %) in the DD (LL) sample. The cut efficiency on $\Lambda^0_b \to J/\psi\Lambda$ signal MC is given in Sec. 5.4.

DTF fit performance and K^0_S decay time significance cuts

Finally, cuts on the $\mathrm{DTF}^{J/\psi K^0_S}_{\mathrm{PV}}$ fit $\chi^2/\mathrm{ndf} < 30$ and on the K^0_S decay time significance (wrt. to the B^0 decay vertex) of $t_{K^0_S}/\sigma_{t_{K^0_S}} > 4$ from a $\mathrm{DTF}_{\mathrm{PV}}$ fit are applied. These two cuts yield a signal efficiency of 99.25 % (97.61 %) and a background rejection of 33.68 % (24.89 %) for the DD (LL) sample.

The fit range is limited to events within $0.3\,\mathrm{ps} < t < 18.3\,\mathrm{ps}$. Low decay time candidates are neglected to suppress decay time acceptance effects and prompt background. The number of candidates with decay times above the limit is negligible. This cut yields a signal efficiency of 95.30 % (94.86 %) and a background rejection of 12.77 % (25.71 %) for the DD (LL) sample.

Overall offline selection performance

The total offline selection performance shows a signal efficiency of $\varepsilon_{\mathrm{Sig}} \sim 90\,\%$ paired with a background rejection of $1 - \varepsilon_{\mathrm{Bkg}} \sim 70\,\%$. The exact numbers quoted separately for DD and LL are given in Tab. 5.9.

Table 5.9 – Overall offline selection performance.

	$\varepsilon_{\mathrm{Sig}}$	$1 - \varepsilon_{\mathrm{Bkg}}$
DD	89.55 %	67.61 %
LL	89.79 %	70.60 %

Table 5.10 – Number of multiple $B^0 \to J/\psi K^0_S$ candidates after stripping. The numbers in the first row represent the fraction of B^0 candidates that are not *unique* in an event, i.e. the event contains more than one candidate. The numbers in the second row show the fraction of events with multiple B^0 candidates. Additionally, a listing of the occurrence of events with different numbers of multiple B^0 candidates is given. The last row shows the fraction of B^0 candidates that need to be discarded in order to only get events with a single B^0 candidate.

	2011		2012	
fraction of multiple B^0 candidates	4.2 %		4.9 %	
fraction of events with multiple B^0 candidates	2.1 %		2.4 %	
	$\#B^0$ cands	#events	$\#B^0$ cands	#events
	1	575780	1	1482895
	2	11997	2	35921
	3	382	3	1223
	4	50	4	194
	5	4	5	9
	6	1	6	9
	7	0	7	1
fraction of B^0 candidates to discard	2.2 %		2.5 %	

5.2.4 Multiple candidates

As in a typical LHCb bunch crossing around 2.5 visible proton-proton collisions occur, the chances are high to find more than one primary vertex per recorded event. Choosing the primary vertex with the highest quality of the trajectory impact parameter DTF fit with respect to the B^0 candidate is called *best PV selection* in contrast to a *random PV selection*. Given the small $B^0 \to J/\psi K^0_S$ branching ratio, not more than one signal event can be expected per event. Still, it is possible that more than one candidate gets reconstructed. From those candidates either one can be chosen by its DTF trajectory impact parameter fit quality with respect to a given PV (*best B^0 candidate selection*) or as well randomly (*random B^0 candidate selection*). Instead of consecutively selecting a primary vertex and B meson candidate a joint decision can be made. Each (PV, B^0) pair can again be chosen either based on the best fit quality or by random. The number of multiple primary vertices and candidates is studied following Ref. [95].

After stripping selection around 2 % of the events contain more than one B^0 candidate and $4-5$ % of all B meson candidates are not unique in their event (cf. Tab. 5.10). After stripping and subsequent offline selection roughly 0.3 % of events

contain multiple B^0 candidates while in 6 % of the events more than one primary vertex is found. Tab. 5.11 presents the detailed numbers for multiple primary vertex and B^0 candidates after stripping and offline selection. Of the remaining (PV, B^0) pairs one is chosen randomly.

5.2.5 MC and data samples

All candidates in the nominal dataset finally used for the fit to estimate the CP observables $S_{J/\psi K^0_S}$ and $C_{J/\psi K^0_S}$ pass the given trigger configuration, the detached stripping selection, and the described offline selection leaving 114 000 signal candidates. The analysis only uses 42 000 tagged signal candidates. Tab. 5.12 lists the numbers of tagged signal candidates split into subsamples of tagger, trigger, track type, and year of data-taking. The mass distribution of the nominal dataset, split into year of data-taking and track type is depicted in Fig. 5.2.

MC datasets

The Monte Carlo (MC) samples are produced using Pythia6 and Pythia8 in the generation step. An equal amount of events is generated using each generator version and also for both possible magnet polarities. Also different samples are produced for 11 and 12 running conditions. The EvtGen physics model is set to `SSD_CP` with parameters as summarised in Tab. 5.13. Studies to check for possible background contributions from partly reconstructed decays or decays with mis-identified particles (outlined in Sec. 5.4) require several inclusive and exclusive MC samples using the same generator toolchain as in the generation of the nominal signal MC sample. Tab. 5.14 shows the used MC data sets and gives the number of generated events.

Table 5.11 – Number of multiple candidates after stripping and selection. The numbers in the first row represent the fraction of (PV, B^0) candidate pairs that are not unique in an event. The numbers in the second row show the fraction of events with multiple (PV, B^0) candidate pairs. The third row includes the numbers of event with multiple B^0 candidates. Additionally, a listing of the occurrence of events with different numbers of multiple B^0 candidates is given. After that, the number of B^0 candidates to discard is given. In the fourth row the number of events containing multiple PVs is listed together with the detailed description of the frequency of multiple PVs per event. The last row shows the fraction of (PV, B^0) candidate pairs that need to be discarded in order to only keep one (PV, B^0) candidate per event.

	2011		2012	
fraction of multiple candidates	12.5 %		12.8 %	
fraction of events with multiple (PV, B^0) candidates	6.0 %		6.1 %	
fraction of events with multiple B^0 candidates	0.3 %		0.4 %	
	#B^0 cands	#events	#B^0 cands	#events
	1	74065	1	165915
	2	253	2	635
	3	0	3	3
fraction of B^0 candidates to discard	0.3 %		0.4 %	
fraction of events with multiple PVs	5.7 %		5.8 %	
	#PVs	#events	#PVs	#events
	1	69755	1	156211
	2	4279	2	9583
	3	265	3	692
	4	19	4	58
	5	0	5	9
fraction of (PV, B^0) candidate pairs to discard	6.5 %		6.6 %	

Table 5.12 – Number of tagged signal candidates split into categories of tagger, trigger, track type, and year of data-taking. All numbers rounded.

			DD					LL		
11	OS	AU	5134	5991	9423	OS	AU	2263	2597	3799
		EB	857				EB	334		
	SS	AU	2028	2352		SS	AU	744	834	
		EB	324				EB	90		
	BS	AU	941	1080		BS	AU	321	368	
		EB	139				EB	47		
12	OS	AU	10 378	12 567	20 160	OS	AU	4599	5571	8178
		EB	2189				EB	972		
	SS	AU	4247	5226		SS	AU	1550	1831	
		EB	979				EB	281		
	BS	AU	1963	2367		BS	AU	658	776	
		EB	404				EB	118		

Table 5.13 – Physics parameters used in the simulation.

Parameter	Generation value
Δm_d	$0.502 \cdot 10^{12}$ ($\hbar$/s)
$\frac{\Delta\Gamma}{\Gamma}$	0
$\left\lvert\frac{q}{p}\right\rvert$	1
$\arg(\frac{q}{p})$	-0.775
$\lvert A_f\rvert$	1
$\arg(A_f)$	0
$\left\lvert A_{\bar{f}}\right\rvert$	-1
$\arg(A_{\bar{f}})$	0
τ	1.519 068 ps

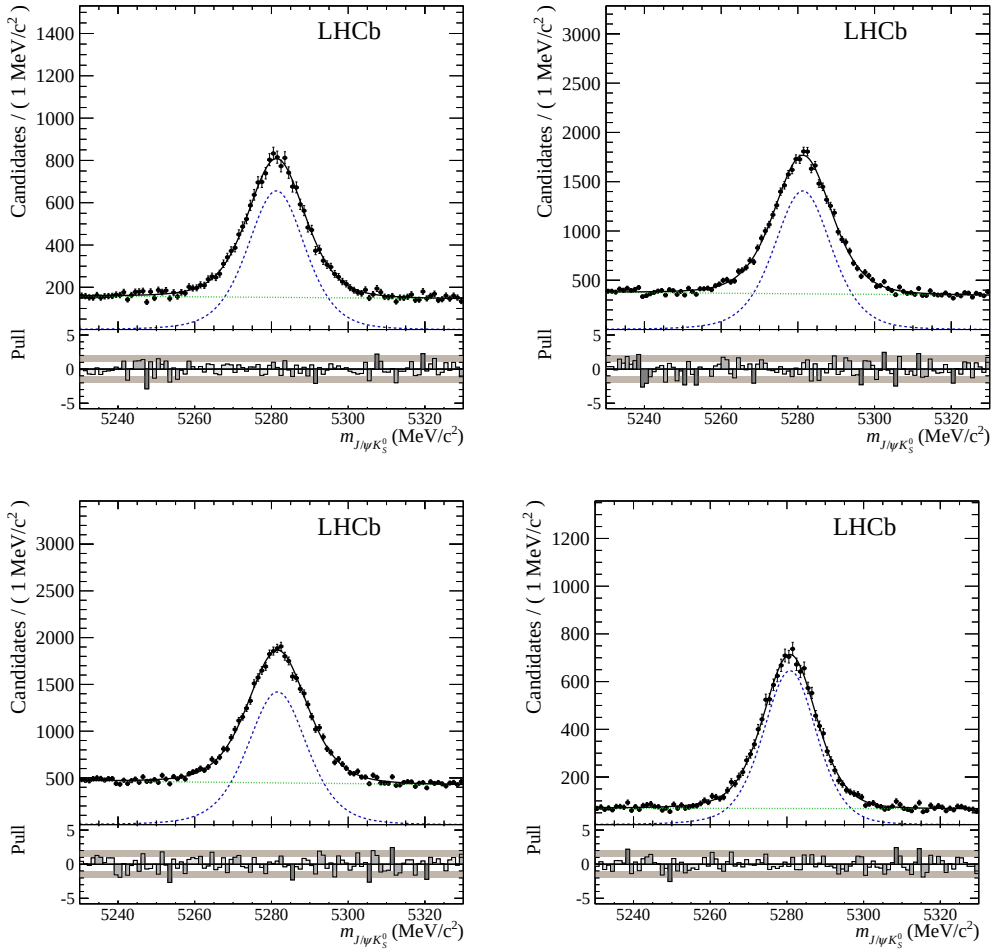

Figure 5.2 – Mass distribution of the nominal dataset, split into year of data-taking and into K^0_S track type. Top row: on the left 11, on the right 12. Bottom row: on the left DD, on the right LL. The solid black line shows the fit projection of the nominal mass PDF (cf. Sec. 5.6.2). The blue dashed line shows the signal, the green dashed line the background component.

Table 5.14 – Inclusive and signal MC data sets used in this analysis, with the generated number of events and if possible an estimate on the corresponding integrated luminosity.

MC name	# events	int. lumi. [fb^{-1}]
inclJpsi	60 M	-
Bd2JpsiX	20 M	-
Bu2JpsiX	20 M	-
Bs2JpsiX	20 M	-
Bd2JpsiKst	4 M	≈ 1.6
Lb2JpsiL	3 M	≈ 15

5.3 Flavour tagging

The flavour tagging employed is described in detail in Ch. 4. Two different tagging decisions are utilised: the opposite-side (OS) tagger combination and the same-side pion (SSπ) tagger. The calibration and subsequent combination of the two tagging decisions is performed within the fit (cf. Sec. 5.6). To assure correct propagation of uncertainties and correlations of the calibration parameters to the *CP* parameters Gaussian constraints based on the calibration parameters' central values and theirs statistical uncertainties are applied. The influence of the systematic uncertainties on the calibration parameters is described in Sec. 5.8.2.

5.3.1 Performance

The effective tagging efficiency (Eq. (4.3))—inherent in the used data sample given the choice of utilised taggers—is calculated as the sum of the effective tagging efficiencies carried by each (including untagged) signal candidate

$$\varepsilon_{\text{eff}} = \frac{\sum_{i=0}^{N} w_i D_i^2(d_{\text{OS}}, d_{\text{SS}\pi}, \omega_{\text{OS}}, \omega_{\text{SS}\pi})}{\sum_{i=0}^{N} w_i}\,, \tag{5.1}$$

where ω_{OS} and $\omega_{\text{SS}\pi}$ refer to the calibrated mistag estimates. The signal sWeights w_i for each candidate are computed from an sPlot fit to the B^0 mass distribution using the nominal mass PDF described in Sec. 5.6. This adds up to an effective tagging efficiency of $\varepsilon_{\text{eff}} = (3.02 \pm 0.05)\,\%$, which splits into a tagging efficiency of $\varepsilon_{\text{tag}} = (36.54 \pm 0.14)\,\%$ and an effective dilution of $D = (28.75 \pm 0.24)\,\%$ corresponding to an average mistag probability of $\omega = (35.62 \pm 0.12)\,\%$.

Tab. 5.15 lists the tagging efficiency separate for the OS, SS, and BS parts of the dataset, as well as for the case where all SSπ decisions are ignored and only the OS tagging information are exploited ('all OS') and vice versa ('all SSπ'). This allows the performance obtained on the given dataset to be compared with the results of the previous LHCb measurement [28], where only the tagging information provided by the OS algorithms were used. Here, relative improvements of 10 % from 2.38 % to 2.63 % can be observed. Finally, supplementing the measurement with information from the SSπ tagger allows for an overall improvement in effective tagging efficiency of almost 27 %.

Table 5.15 – Effective tagging efficiency given for all three tagging categories. Additionally listed are the results just exploiting the information of the OS or SSπ tagging algorithms, as well as the total effective tagging efficiency of the dataset.

Tagger	ε_{eff} [%]
OS	2.259 ± 0.034
SS	0.262 ± 0.017
BS	0.503 ± 0.010
all OS	2.63 ± 0.04
all SSπ	0.376 ± 0.024
Total	3.02 ± 0.05

5.4 Backgrounds

This section describes the evaluation of background contributions in the data. Besides combinatorial background from particles combined by chance with properties that allow to pass all selection steps two other sources are investigated: physics backgrounds from decays with mis-identified final state particles are studied in Sec. 5.4.1 and the influence of non-uniform tagging responses for the background candidates is examined in Sec. 5.4.2.

5.4.1 Physics backgrounds

To ensure that the background consists only of combinatorial backgrounds, and that exclusive backgrounds are negligible, possible physics backgrounds are studied with simulated data (see Sec. 5.2.5).

Using the true particle identities from MC reveals the existence of remnants from physics backgrounds in the inclusive J/ψ and the $B^0 \to J/\psi X$ MC samples.

Compared to the number of all reconstructed events, around 0.04 % $B^0 \to J/\psi K^{*0}$ candidates survive the applied selection criteria compared to 0.5 % signal events in the sample of $B^0 \to J/\psi X$ decays. In the inclusive J/ψ sample 0.0005 % $B^0 \to J/\psi K^{*0}$, 0.0002 % $B_s^0 \to J/\psi K_S^0$, and 0.0002 % $\Lambda_b^0 \to J/\psi \Lambda$ background events contribute, compared to 0.01 % $B^0 \to J/\psi K_S^0$ candidates.

Since the production of B_s^0 mesons is a factor 100 less frequent than that of the lighter B^0 mesons and reconstructed $B_s^0 \to J/\psi K_S^0$ candidates lie outside the nominal mass range, no contributions are expected. While $B^0 \to J/\psi K^{*0}$ background results from kaon-pion mis-identification, $\Lambda_b^0 \to J/\psi \Lambda$ candidates are found in the sample due to a proton-pion mis-identification. Their expected contribution in the data sample is further studied by using signal MC samples of $B^0 \to J/\psi K^{*0}$ and $\Lambda_b^0 \to J/\psi \Lambda$.

Physics backgrounds from K-π mis-ID

In the $B^0 \to J/\psi K^{*0}$ signal MC 0.3 % of $4 \cdot 10^6$ generated background candidates get reconstructed and survive the applied stripping cuts. This number already reduces to 0.004 % after applying cuts on the nominal mass and time ranges. After full offline selection, considering a tagging efficiency of 38 %, and scaling the numbers to match a data sample corresponding to $3\,\text{fb}^{-1}$ integrated luminosity, 20 $B^0 \to J/\psi K^{*0}$ candidates remain. This corresponds to a fraction of roughly 0.04 % of the background in the nominal data sample. The source of the remaining contributions are e.g. decays like $B^{0*} \to B^0(\to J/\psi K^{*0})\, X$.

Physics backgrounds from p-π mis-ID

Out of $3 \cdot 10^6$ generated $\Lambda_b^0 \to J/\psi\Lambda$ signal candidates only 2 % get reconstructed and pass the stripping. The cuts on the nominal mass and time ranges reduce this number down to 0.32 %. The veto cut applied in the offline selection (see Sec. 5.2.3) decreases the number of candidates inside this mass and decay time window by more than 50 % to 0.15 %. After applying the full offline selection, including the tagging efficiency, and scaling the sample to correspond to the collected integrated luminosity in data, 120 $\Lambda_b^0 \to J/\psi\Lambda$ candidates remain. Therefore, we expect a 0.2 % contribution of $\Lambda_b^0 \to J/\psi\Lambda$ background candidates in the nominal data sample.

5.4.2 Background tagging asymmetries

As shown in the previous section any physics induced background in the data sample can be neglected and the remaining background candidates are assumed to be purely of combinatorial origin. Following this, all flavour tagging decisions provided for background candidates should be randomly distributed. This assumption can be tested in two ways: counting the time-integrated numbers of B^0 and $\overline{B}^0$ tagged background candidates or checking for a non-vanishing time-dependent tag asymmetry in the background.

The tests are performed independently for the DD and LL subsample as well as for both employed tagging algorithms (OS and SSπ). In order to study the background sample an unbinned maximum likelihood fit is performed on the B^0 mass distribution and background sWeights [89] are computed. The signal component is modelled using a Hypatia PDF while the background component is described by an exponential PDF (cf. Sec. 5.6.2).

Time integrated background asymmetry

The time-integrated asymmetry

$$\mathcal{A}^{\text{int}}_{\text{Bkg}} = \frac{N^{\overline{B}^0}_{\text{Bkg}} - N^{B^0}_{\text{Bkg}}}{N^{\overline{B}^0}_{\text{Bkg}} + N^{B^0}_{\text{Bkg}}} \tag{5.2}$$

is computed for all four subsamples using the sWeighted dataset and the results are collected in Tab. 5.16. Compared to the time-integrated *CP* asymmetry (cf. Eq. (5.49)) in the signal component in the order of $\mathcal{O}(0.1)$ the time-integrated background tagging asymmetry is small and except for the DD OS subsample the results are not significant. A vanishing time-integrated asymmetry does not eliminate the possibility of a time-dependent asymmetry, thus further studies are necessary.

Table 5.16 – Time-integrated asymmetry of sWeighted background distributions for DD and LL OS and SSπ tagged events.

category		$\mathcal{A}^{\text{int}}_{\text{Bkg}}$
DD	OS	0.017 ± 0.005
	SSπ	-0.016 ± 0.011
LL	OS	-0.005 ± 0.012
	SSπ	0.044 ± 0.034

Decay time dependent background asymmetry

The decay time dependent background tagging asymmetry is defined similar to Eq. (5.2) as

$$\mathcal{A}_{\text{Bkg}}(t) = \frac{N^{\overline{B}^0}_{\text{Bkg}}(t) - N^{B^0}_{\text{Bkg}}(t)}{N^{\overline{B}^0}_{\text{Bkg}}(t) + N^{B^0}_{\text{Bkg}}(t)}\,. \tag{5.3}$$

At first, histograms of $\mathcal{A}_{\text{Bkg}}$ in bins of the decay time are consulted to check for the null-hypothesis of a vanishing asymmetry using a χ^2-test. The test is performed on the background sWeighted dataset as well as on a background sWeighted cocktail MC sample. The latter is built from signal MC and background candidates from a pseudo-experiment (ToyMC) sample generated with randomly distributed tag decisions. Finally, a likelihood fit to the decay time distribution of the background sWeighted dataset is performed using a PDF $\mathcal{P}_{\text{TagAsym}}(t, d)$ modelling a potential tag asymmetry.

$$\mathcal{P}_{\text{TagAsym}}(t, d) \propto \mathrm{e}^{-\frac{t}{\tau}}\,(1 + d\mathcal{A}) \tag{5.4}$$

Histograms of the background candidates binned in the reconstructed decay time are created for DD/LL candidates with OS and SSπ tag decisions. This is done for the background sWeighted data sample and for a cocktail MC sample, where the sWeights are extracted using the same model as used before. Figs. 5.3 and 5.4 show the histograms. The corresponding p-values from the χ^2-test are summarised in Tab. 5.17. All p-values do not contradict the tested null-hypothesis. Increased p-values for LL SSπ are found both on data and cocktail MC and might be explained by the low statistics in this particular subsample.

Table 5.17 – Resulting p-values from a χ^2-test for the time-integrated asymmetry. The values were computed on sWeighted background distributions for DD and LL OS and SSπ tagged events.

category		p-value data	p-value cocktail MC
DD	OS	0.100	0.525
	SSπ	0.437	0.386
LL	OS	0.617	0.110
	SSπ	0.969	0.989

A likelihood fit to the sWeighted background candidates is conducted in order to exploit the per-event tag information. To do so the distributions are fitted using a PDF as presented in Eq. (5.4) where a potential asymmetry has been modelled. The parametrisation uses the sum of three (two in case of the DD SSπ subsample) exponential PDFs with independent pseudo-lifetimes τ_i and individual asymmetry parameters $\mathcal{A}_i$.

Table 5.18 – Fit results of the asymmetries $\mathcal{A}_i$ of a fit to the sWeighted background distributions of DD and LL OS and SSπ tagged events.

category		$\mathcal{A}_1$	$\mathcal{A}_2$	$\mathcal{A}_3$
DD	OS	0.001 ± 0.028	-0.039 ± 0.030	-0.01 ± 0.07
DD	SSπ	-0.01 ± 0.04	0.14 ± 0.14	—
LL	OS	0.05 ± 0.05	-0.03 ± 0.13	-0.11 ± 0.12
LL	SSπ	-0.01 ± 0.20	-0.18 ± 0.18	0.4 ± 0.4

A final conclusion on how to proceed is difficult as the results are inconclusive due to a lack of statistical power. Although all results are compatible with the hypothesis of a vanishing background tagging asymmetry, there is evidence of non-vanishing asymmetries supported by fluctuations found in the results.

Thus, the nominal fit model does not incorporates a description of a potential tagging asymmetry in the background component. The impact of this decision is further investigated in a ToyMC study presented in Sec. 5.8.2

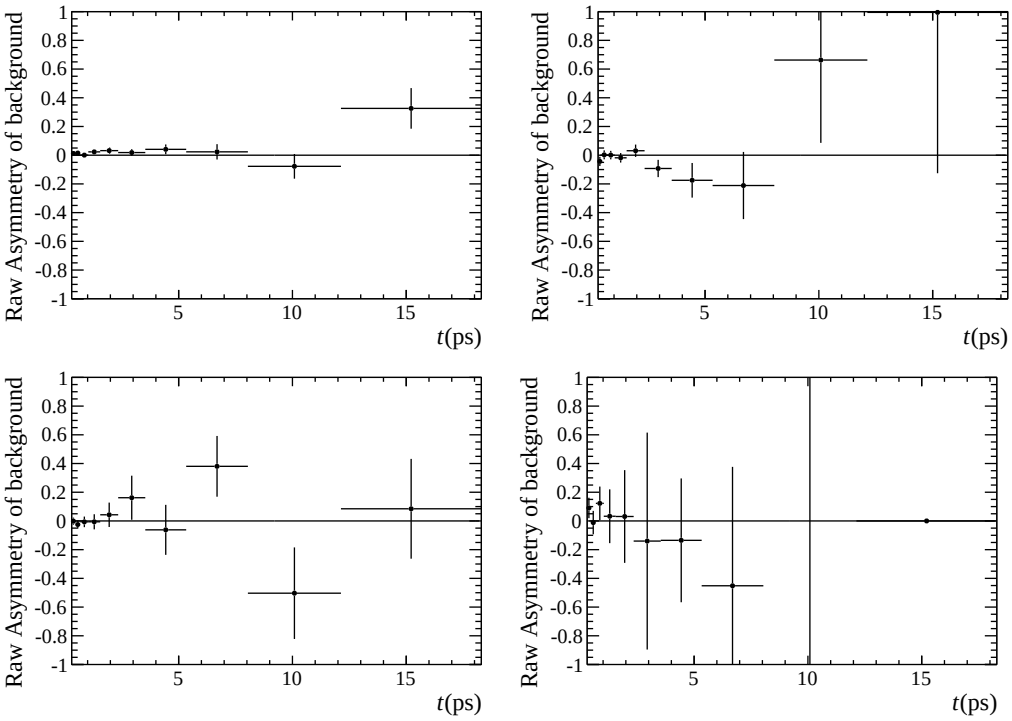

Figure 5.3 – Tagging asymmetry $\mathcal{A}(t)$ in background sWeighted data. The binning of the x-axis is chosen logarithmic. The top (bottom) plots show DD (LL) candidates, while OS (SSπ) tagged candidates are depicted in the left (right) side.

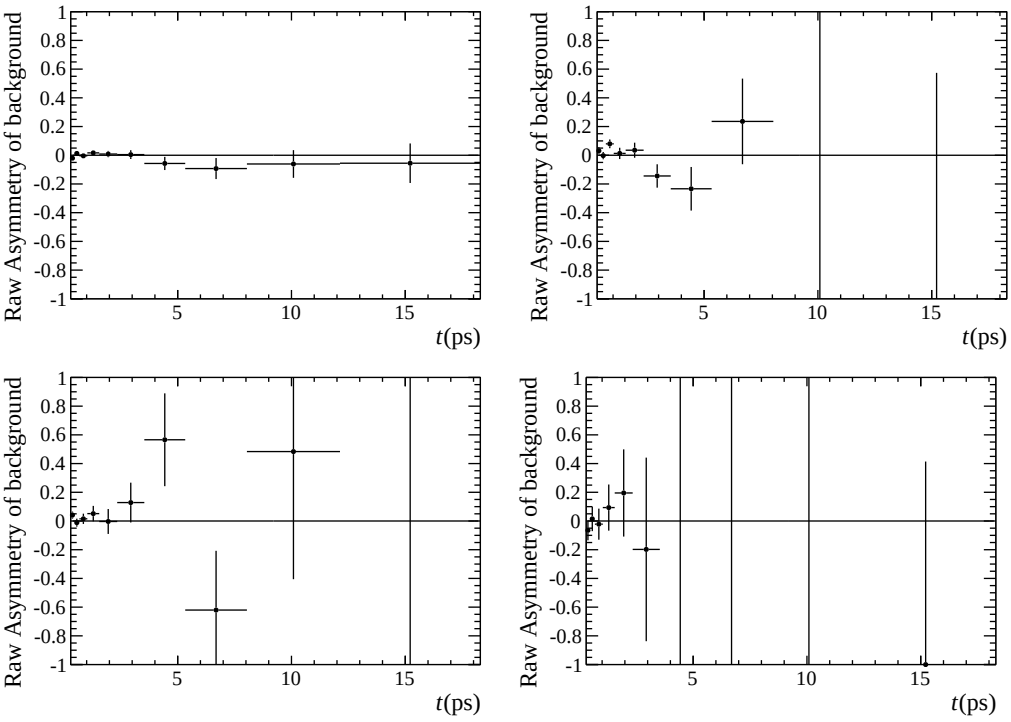

Figure 5.4 – Tagging asymmetry $\mathcal{A}(t)$ in cocktail MC with signal candidates taken from $B^0 \to J/\psi K^0_S$ signal MC and background candidates from a ToyMC sample. The binning of the x-axis is chosen logarithmic. The top (bottom) plots show DD (LL) candidates, while OS (SSπ) tagged candidates are depicted in the left (right) side.

5.5 Decay time resolution and acceptance

In the following sections the parametrisation of the decay time resolution and the model to describe the decay time acceptance are studied.

5.5.1 Resolution

In this section the applicability of the $\mathrm{DTF}_{\mathrm{PV}}$ output variable σ_t as the per-event decay time error resolution estimate is checked and a model to calibrate the estimate is developed. The model is determined in a two step procedure. At first, different calibration models are tested using a binned fit on the decay time resolution determined on data as a function of the resolution estimate σ_t. Then the found resolution model is used in an unbinned likelihood fit to determine the calibration parameter values.

The study is performed on $B^0 \to J/\psi K^0_{\mathrm{S}}$ candidates passing the pre-scaled stripping line and the unbiased trigger lines only. The nominal selection is applied, except the decay time cut at $t < 0.3\,\mathrm{ps}$, all remaining candidates are considered irrespective of their tagging information. Without cuts restricting the reconstructed decay time of the B^0 candidates, the sample consists mainly of combinatorial background candidates promptly produced at the PV. As these candidates quasi decay instantaneously at $t = 0$ their decay time distribution should give a proper handle on the decay time resolution. A fit to the J/ψ candidate's reconstructed mass is applied to get signal sWeights that are subsequently used in a weighted likelihood fit to the reconstructed B^0 candidates' decay time distribution.

The J/ψ mass distribution is described by a Hypatia PDF (cf. Sec. 5.6.1) for the signal component and an exponential PDF for the background candidates. The fit is performed on the reconstructed invariant dimuon mass $m_{\mu^+\mu^-}$ in a range from 3040 to 3155 MeV/c^2. The fitted distribution and the PDF projections split into the DD and LL categories are shown in Fig. 5.5. Although, the pion track types have no influence on the mass distribution of the J/ψ candidates, the separation is justified by the different decay time resolutions expected in these categories. Using a simultaneous fit in 20 equally filled bins of the decay time error prediction σ_t the width of the prompt peak in the decay time distribution is fitted. This choice is based on the assumption that the decay time resolution behaves alike for all candidates combined into one bin. As the last bin is too wide, this assumption does not hold not any more, thus the last bin is left out from then on. The fit model consists of two Gaussian PDFs sharing a common mean parameter to model the prompt peak and two additional decay PDFs as parametrisation of the non-prompt components. The decay PDF is convoluted with the same double-Gaussian PDF used to model the prompt peak. The two widths—one narrow and one wider—are then both employed in the calibration.

For both widths a binned χ^2-fit of the 19 per-bin parameter values against the per-bin σ_t averages is performed. One linear and two parabolic calibration models (with and without offset) are tested. For both widths ($i = \{1, 2\}$) as well as for

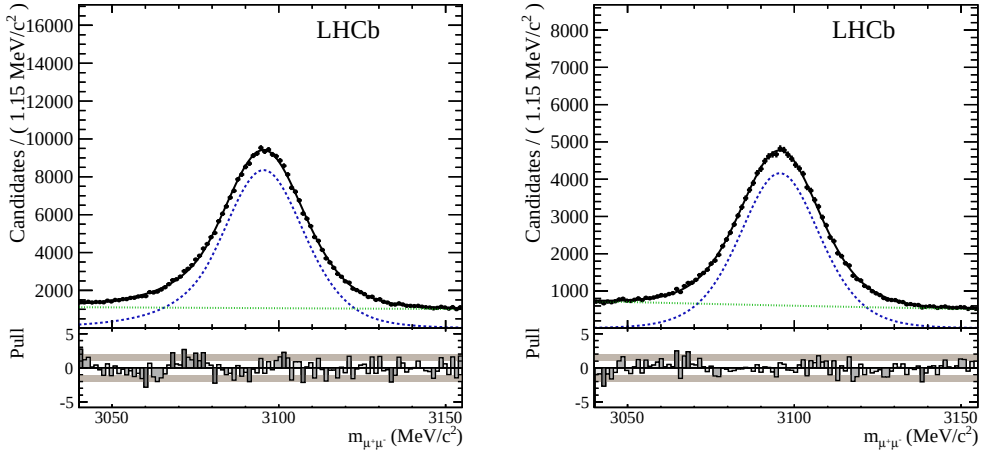

Figure 5.5 – Invariant J/ψ candidates' mass distribution in the (left) DD and (right) LL subsample. Data are shown in black, the projection of the total PDF as solid black line, the signal component described by a Hypatia PDF as dashed blue line, and the exponential background component as dotted green line.

both the DD and LL candidates the linear model $\sigma'(\sigma_t) = c_i + b_i\sigma_t$ describes the data at least equally well wrt. the other parametrisations, such that the simpler model is chosen in case of comparable results. Fig. 5.6 shows the calibration function for both track types and both Gaussian width parameters. Results of the depicted fits are given in Tab. A.1 and A.2 in Appendix A.1.1.

Using the determined calibration model, the nominal decay time resolution model is developed. An unbinned maximum likelihood fit to the B^0 decay time is performed on the same J/ψ signal sWeighted dataset as described before using the resolution model

$$\begin{aligned}\mathcal{R}(t;\sigma_t) = \sum_{i=1}^{2} g_i \cdot \frac{1}{\sqrt{2\pi}(c_i + b_i\cdot\sigma_t)} \exp\left(-\frac{(t-\mu_t)^2}{2(c_i+b_i\cdot\sigma_t)^2}\right) \\ + f_{\mathrm{PV}} \frac{1}{\sqrt{2\pi}\sigma_{\mathrm{PV}}} \exp\left(-\frac{(t-\mu_t)^2}{2\sigma_{\mathrm{PV}}^2}\right).\end{aligned} \tag{5.5}$$

The first two Gaussian components describe the prompt peak resolution, the third component models the distribution of candidates associated to the wrong PV. Different calibration parameters c_i and b_i are chosen for the width of the narrow ($i = 1$) and the wide ($i = 2$) Gaussian PDF. The fractions g_i add up to unity together with the fraction f_{PV} of candidates associated to the wrong PV. The offset μ_t of the Gaussian central value is shared between all three Gaussian PDFs. Finally, σ_{PV} describes the width of the wrong PV component. The decay time distribution is modelled using two decay PDFs that are convoluted with the resolution model $\mathcal{R}(t;\sigma_t)$ and with pseudo-lifetimes $\tau_{1,2}$. Tab. 5.19 lists the results that are used from now on in the decay time resolution model. It is tested how

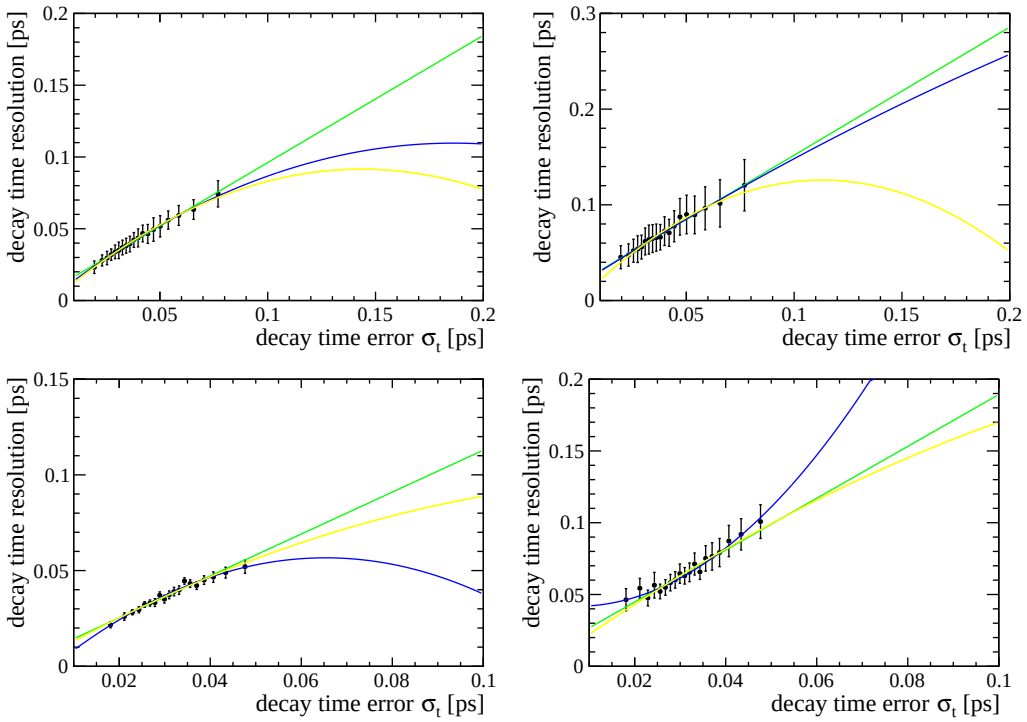

Figure 5.6 – Decay time error estimate calibration for (top) DD and (bottom) LL candidates. Different calibration functions are fitted to the (left) narrow and the (right) wide Gaussian width parameters. In green the linear function $\sigma'(\sigma_t) = c_i + b_i\sigma_t$ is shown, blue and yellow describe the parabolic function with and without offset.

the choice of the calibration model influences the measurement using a ToyMC study (Sec. 5.8.2).

5.5.2 Decay time acceptance

Acceptance effects that alter the distribution of the decay time might result from selection requirements or inefficiencies in the event reconstruction. This section summarises acceptance effects stemming from lifetime biasing selection cuts of trigger requirements (cf. Sec. 5.2.1) and reconstruction inefficiencies mainly caused by the VELO track reconstruction algorithms (cf. Sec. 3.3).

Trigger induced decay time acceptance

The biased trigger lines (cf. Sec. 5.2.1) and the stripping cut on the reconstructed decay time of the B^0 candidates result in a non-flat decay time acceptance.

In order to correctly describe these effects, the data sample is split into two disjoint categories of candidates that show a substantially different behaviour regarding their decay time acceptance. All candidates passing the *almost unbiased*

Table 5.19 – Results of the fit of the parameters described in the decay time resolution model.

Parameter		DD sample		LL sample	
μ_t	(ps)	$-0.002\,91$	$\pm\,0.000\,26$	$-0.001\,69$	$\pm\,0.000\,26$
b_1		0.88	$\pm\,0.09$	1.04	$\pm\,0.14$
c_1	(ps)	0.0077	$\pm\,0.0028$	0.0045	$\pm\,0.0028$
b_2		1.33	$\pm\,0.33$	1.8	$\pm\,0.4$
c_2	(ps)	0.019	$\pm\,0.008$	0.007	$\pm\,0.005$
g_2		0.251	$\pm\,0.020$	0.240	$\pm\,0.023$
σ_{PV}	(ps)	1.6	$\pm\,0.7$	1.40	$\pm\,0.14$
f_{PV}		0.048	$\pm\,0.004$	0.0488	$\pm\,0.0024$
τ_1	(ps)	0.7	$\pm\,0.5$	0.29	$\pm\,0.06$
τ_2	(ps)	2.1	$\pm\,1.3$	1.82	$\pm\,0.12$
f_1		0.08	$\pm\,0.10$	0.046	$\pm\,0.006$
f_2		0.08	$\pm\,0.11$	0.079	$\pm\,0.009$

(**AU**) trigger requirements show nearly no decay time acceptance effects, in contrast to the sample of candidates passing the *exclusively biased* (**EB**) trigger requirements. The addressed requirements are:

AU `DiMuonHighMass && DiMuonDetachedJPsi`

EB `(TrackMuon && !DiMuonHighMass) && DiMuonDetachedJPsi`

To construct the acceptance in terms of ratios, a sample of candidates that pass a set of unbiased trigger requirements is needed:

Unbiased `DiMuonHighMass && DiMuonJPsi`

The acceptance of the AU subsample can be computed using the overlap of events which pass the biased and the unbiased HLT2 di-muon lines. Both lines are using the same trigger cuts except for an additional cut on the flight distance significance (see Tab. 5.3) in the case of the biased line. The acceptance can then be written as a time-dependent efficiency $\varepsilon_{\mathrm{AU}}$, with

$$\begin{aligned}\varepsilon_{\mathrm{AU}} &= \frac{\texttt{AU \&\& Hlt2DiMuonJPsi}}{\texttt{Unbiased}} \\ &= \frac{\texttt{DiMuonHighMass \&\& DiMuonDetachedJPsi \&\& DiMuonJPsi}}{\texttt{DiMuonHighMass \&\& DiMuonJPsi}}\,.\end{aligned} \tag{5.6}$$

For the EB subsample, there is no corresponding reference sample available, so strictly speaking only a relative efficiency can be computed. Nonetheless, the ratio

of the EB subsample and the unbiased subsample can be computed as $\varepsilon_{\mathrm{EB}}$.

$$\begin{aligned}\varepsilon_{\mathrm{EB}} &= \frac{\texttt{EB}}{\texttt{Unbiased}} \\ &= \frac{\texttt{(TrackMuon \&\& !DiMuonHighMass) \&\& DiMuonDetachedJPsi}}{\texttt{DiMuonHighMass \&\& DiMuonJPsi}}.\end{aligned} \tag{5.7}$$

In other words $\varepsilon_{\mathrm{AU}}$ quantifies the efficiency due to the requirements by the biased HLT2 line for events that pass the unbiased HLT1 line, whereas $\varepsilon_{\mathrm{EB}}$ effectively quantifies the relative efficiency introduced by both, the HLT1 and HLT2, biased trigger lines.

Methodology

The data set for studying the trigger acceptance effects consists of all events that are selected by the `BetaSBd2JpsiKsDetached` stripping line and pass the offline selection. As the tagged and untagged candidates are expected to behave equally concerning the studied effect all available candidates are used. On the remaining multiple candidates, a random candidate selection is applied. All candidates are selected by either one of the four considered trigger lines.

The efficiencies are time-dependent and, since the focus lies on the acceptance of the signal component's decay time distribution, have to be determined through a fit to separate signal from background. To do so, a simultaneous fit for the signal yield is performed in ten bins of decay time. The bin boundaries are chosen in a way that each bin contains the same number of events (before splitting the data into the different fit categories). The fit is also performed simultaneously in categories of track type, tagger, and both trigger sets given by the numerators and the denominator of $\varepsilon_{\mathrm{AU}}$ and $\varepsilon_{\mathrm{EB}}$. The yields for the different tagger and track type categories are summed up (including error propagation). Then the efficiency per time bin is calculated. For $\varepsilon_{\mathrm{AU}}$ a binomial error is estimated, while a Gaussian error propagation is used for $\varepsilon_{\mathrm{EB}}$.

In the mass fit, the signal peak is described by a Hypatia PDF, while a single exponential is used to describe the combinatorial background. Fig. 5.7 shows both mass distributions and fit projections for the biased and unbiased sample, respectively. In both plots the sum over all categories is displayed. Fig. 5.8 shows the acceptance histograms for the AU and the EB sample. In the nominal fit cubic splines [96] are used instead of the histograms themselves. Each bin centre is used as a knot for the splines. The bin contents determine the shape of the splines. However, the bin contents aren't fixed but constrained with a Gaussian function where the width is given by the uncertainty on the bin content. As there is no information about the acceptance at the decay time limits, the efficiency is assumed to be flat between the lower decay time limit at 0.3 ps and the first bin centre/knot and the last bin centre/knot and the upper decay time limit at 18.3 ps, respectively.

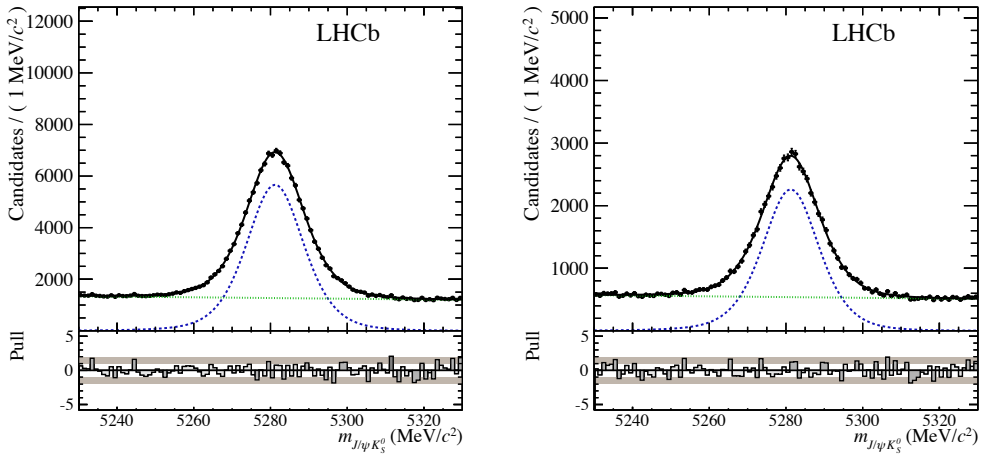

Figure 5.7 – Mass distribution and fit projection summed over all categories for the (left) biased (AU and EB) and the (right) unbiased sample.

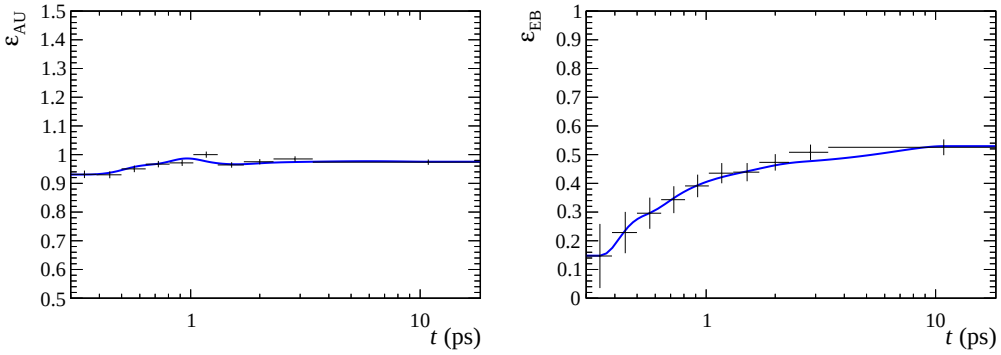

Figure 5.8 – Histograms of the trigger acceptance for the (left) almost unbiased and the (right) exclusively biased sample. The blue curve shows the fitted acceptance using cubic splines.

Table 5.20 – Decay time correction factor β_τ in ps^{-1}.

	2011	2012
DD	0.0036 ± 0.0029	0.0084 ± 0.0032
LL	0.018 ± 0.004	0.035 ± 0.005

Upper decay time acceptance

Due to a decrease in the VELO reconstruction efficiency for tracks with a larger offset to the beam line, a second decay time acceptance effect has to be modelled. To account for this a correction factor β_τ is included into the fit model by implementing the modified lifetime

$$\tilde{\tau} = \frac{\tau}{1 + \beta_\tau \tau} \,. \tag{5.8}$$

The value of β_τ is determined using an unbinned fit to simulated data while fixing the lifetime τ to its generation value. Based on the $B^0 \to J/\psi K^0_\mathrm{S}$ signal MC data set, only candidates passing the `BetaSBd2JpsiKsPrescaled` stripping line and the unbiased trigger lines `Hlt1DiMuonHighMass` and `Hlt2DiMuonJPsi` are chosen to avoid any additional lifetime bias for events with short decay times. Only candidates being matched on MC as true signal events are considered. The nominal offline selection is applied and from the remaining multiple (PV, B^0) candidate pairs, one is chosen randomly. To avoid wrong-PV associations of the reconstructed $B^0 \to J/\psi K^0_\mathrm{S}$ candidate the true MC decay time is used in the fit. To reduce the statistical uncertainties, and as no deviations of the decay time distributions are expected, all untagged events are included. The number of remaining MC candidates available for this study is roughly 60 000. Due to differences in the reconstruction efficiency the factor β_τ is determined separately for 11/12 and DD/LL events. The results are collected in Tab. 5.20.

Influence of higher order effects

Eq. (5.8) expands to

$$\begin{aligned} \mathcal{P}(t) &= \mathrm{e}^{-\frac{t}{\tau}(1+\beta_\tau\tau)} \\ &= \mathrm{e}^{-\frac{t}{\tau}-\beta_\tau t} = \mathrm{e}^{-\frac{t}{\tau}}\mathrm{e}^{-\beta_\tau t} \\ &= \mathrm{e}^{-\frac{t}{\tau}}\left(1 - \beta_\tau t + \frac{\beta_\tau^2 t^2}{2} + \mathcal{O}\left((\beta_\tau t)^3\right)\right). \end{aligned} \tag{5.9}$$

To check the influence of higher order terms, a quadratic correction function is tested where the second order term has an own degree of freedom given by γ'_τ,

$$\mathcal{P}(t) = \mathrm{e}^{-\frac{t}{\tau}}\left(1 - \beta'_\tau t + \gamma'_\tau t^2\right). \tag{5.10}$$

Again the parameters β'_τ and γ'_τ are fitted while fixing the lifetime τ. In Tab. 5.21 the results are listed for 11/12 and DD/LL events. To visualise the effect, the

Table 5.21 – Decay time correction factors β'_τ (in ps^{-1}) and γ'_τ (in ps^{-2}).

	2011		2012	
	β'_τ	γ'_τ	β'_τ	γ'_τ
DD	-0.016 ± 0.007	-0.0030 ± 0.0008	-0.001 ± 0.007	-0.0014 ± 0.0009
LL	-0.001 ± 0.009	-0.0028 ± 0.0012	0.01 ± 0.06	-0.0027 ± 0.0008

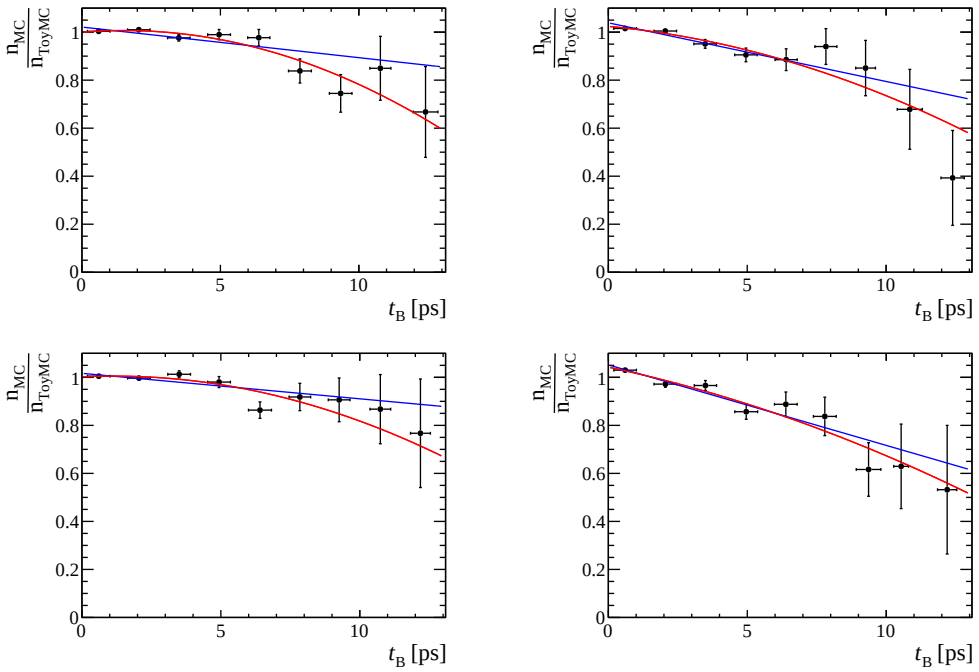

Figure 5.9 – Decay time ratio in bins of decay time for (left/right) DD/LL and (top/bottom) 11/12. The blue (red) curve shows a linear (quadratic) fit to the data points.

per-bin ratio of the decay time distributions of signal MC events to events generated from ToyMC is calculated and shown in Fig. 5.9. The ToyMC decay time distribution follows an exponential function with the same lifetime as used in the generation of the signal MC. As the uncertainties on β'_τ and γ'_τ are large and the parameters are strongly correlated ($\rho > 90\,\%$), the linear model is selected. A possible bias due to this choice is investigated in Sec. 5.8.2.

5.6 Likelihood fit

This section presents the model developed to describe the data and estimate the values and uncertainties of the physics observables using an unbinned extended maximum likelihood (uEML) fit. Starting with a short review of the uEML method, the PDFs in use to describe the different dimensions and components are shown,

and the fit model is outlined.

The *CP* observables of interest $S_{J/\psi K^0_S}$ and $C_{J/\psi K^0_S}$ are estimated in a multi-dimensional simultaneous uEML fit. As summarised in Tab. 5.1 the seven observables $\boldsymbol{x}$ are given by the reconstructed mass and decay time of the B^0 candidate, its decay time error estimate, and its OS and SSπ tag decision as well as the corresponding mistag estimates

$$\boldsymbol{x} = (m_{J/\psi K^0_S}, t, \sigma_t, d_{\mathrm{OS}}, d_{\mathrm{SS}\pi}, \eta_{\mathrm{OS}}, \eta_{\mathrm{SS}\pi}) \,. \tag{5.11}$$

The extended likelihood for a total of $N = \sum_s N^s$ observed events in s subsamples of data, where $n^s = \sum_j n^s_j$ are the expected candidate numbers per subsample for the two categories $j = \{\mathrm{Sig}, \mathrm{Bkg}\}$, is then defined as

$$\mathcal{L}\left(\boldsymbol{\theta}, \boldsymbol{n}; \boldsymbol{x}\right) = \prod_s \frac{\mathrm{e}^{-n^s}}{N^s!} \prod_{i=1}^{N^s} \sum_j^{\{\mathrm{Sig},\mathrm{Bkg}\}} n^s_j \mathcal{P}^s_j\left(\boldsymbol{x}^s_i; \boldsymbol{\theta}_j\right) \,, \tag{5.12}$$

where $\boldsymbol{n}$ is the vector of estimated candidate numbers, and $\boldsymbol{\theta}$ the parameters with unknown values to be estimated by the uEML fit.

The software library RooFit [97]—part of the ROOT [98] software framework—and its implementation of the Minuit algorithm is used to minimize the negative log-likelihood expression $-\ln\mathcal{L}$.

In Sec. 5.6.1 the PDFs used to build the likelihood function are introduced shortly, before Sec. 5.6.2 presents the complete fit model employed by the uEML fit. The approach to prevent any experimenter's bias during the development of the fit model is described in Sec. 5.6.3. The results of the fitter validation study are summarised in Sec. 5.6.4.

5.6.1 List of used probability density functions

The following PDFs are employed to model the distributions of the fit observables.

Exponential

The exponential function with the parameter α to describe e.g. the distribution of combinatorial background candidates with masses m

$$\mathcal{P}_{\mathrm{Exponential}}(m \,|\, \alpha) \propto \mathrm{e}^{\alpha m} \,. \tag{5.13}$$

Decay

The decay function is derived from the exponential function with $\alpha = -1/\tau$, where τ describes the lifetime of candidates with decay times t

$$\mathcal{P}_{\mathrm{Decay}}(t \,|\, \tau) \propto \mathrm{e}^{-\frac{t}{\tau}} \,. \tag{5.14}$$

Gaussian

A simple Gaussian function described by the central value or mean μ and the width σ of the distribution

$$\mathcal{P}_{\text{Gaussian}}(x \,|\, \mu, \sigma) \propto \frac{1}{\sigma\sqrt{2\pi}} \mathrm{e}^{-\frac{1}{2}\left(\frac{x-\mu}{\sigma}\right)^2} . \tag{5.15}$$

Lognormal

The lognormal function is e.g. used to describe the distribution of the decay time error estimate σ_t and is parametrised by its median μ and the parameter $k = \mathrm{e}^{\sigma}$, where σ is named the shape parameter

$$\mathcal{P}_{\text{Lognormal}}(\sigma_t \,|\, \mu, k) \propto \frac{1}{\sigma_t\sqrt{2\pi}\log(k)} \mathrm{e}^{-\frac{\log^2(\sigma_t/\mu)}{2\log^2(k)}} . \tag{5.16}$$

BDecay

A generalised exponential function to describe the time evolution of B meson states with decay times t. The coefficients C, S, and D can be adapted to describe B meson mixing, CP violation, and different asymmetries e.g. in the production of the B mesons. The PDF is further parametrised by the lifetime parameter τ, the decay width difference $\Delta\Gamma$ and the mass difference Δm of the B meson mass eigenstates.

$$\begin{aligned}\mathcal{P}_{\text{BDecay}}(t \,|\, \ldots) \propto \\ \mathrm{e}^{-\frac{t}{\tau}} \left(\cosh(\Delta\Gamma t) + D\sinh(\Delta\Gamma t) + C\cos(\Delta m t) + S\sin(\Delta m t)\right)\end{aligned} \tag{5.17}$$

Hypatia

The Hypatia PDF [91] is a generalisation of the Crystal ball PDF [92], marginalised over the a priori unknown per-event mass resolution. The PDF is used to describe the distribution of the reconstructed B candidates mass $m_{J/\psi K^0_{\mathrm{S}}}$ and is parametrised as

$$\begin{aligned}\mathcal{P}_{\text{Hypatia}}(m \,|\, \mu, \sigma, \lambda, \zeta, \beta, a_1, a_2, n_1, n_2) \propto \\ \begin{cases} G(m, \mu, \sigma, \lambda, \zeta, \beta) & \text{if } -a_1 < \frac{m-\mu}{\sigma} < a_2 \\ \frac{G(\mu - a_1\sigma, \mu, \sigma, \lambda, \zeta, \beta)}{(1 - m S_1^{-1})^{n_1}} & \text{if } -a_1 > \frac{m-\mu}{\sigma} \\ \frac{G(\mu - a_2\sigma, \mu, \sigma, \lambda, \zeta, \beta)}{(1 - m S_2^{-1})^{n_2}} & \text{if } \quad a_2 < \frac{m-\mu}{\sigma} \end{cases},\end{aligned} \tag{5.18}$$

with the substitution

$$S_i = n_i \frac{G(\mu - a_i\sigma, \mu, \sigma, \lambda, \zeta, \beta)}{G'(\mu - a_i\sigma, \mu, \sigma, \lambda, \zeta, \beta)} - a_i\sigma , \tag{5.19}$$

where $G(x, \mu, \sigma, \lambda, \zeta, \beta)$ defines the generalised hyperbolic function

$$G(x, \mu, \sigma, \lambda, \zeta, \beta) = \left((x-\mu)^2 + A_\lambda^2(\zeta)\sigma^2\right)^{\frac{1}{2}\lambda - \frac{1}{4}} \mathrm{e}^{\beta(x-\mu)} K_{\lambda-\frac{1}{2}}\left(\zeta\sqrt{1+\left({}^{x-\mu}/_{A_\lambda(\zeta)\sigma}\right)^2}\right), \quad (5.20)$$

with the cylindrical harmonics K_λ and

$$A_\lambda^2(\zeta) = \frac{\zeta K_\lambda(\zeta)}{K_{\lambda+1}(\zeta)}. \quad (5.21)$$

Here, μ and σ are comparable to the mean and width known from a Gaussian distribution. The parameters λ and ζ describe the shape of the central peak, β characterises the skewness of the distribution. The left and right side tails of the distribution are parametrised by a_i and n_i.

5.6.2 Parametrisation of the fit model

The total PDF is composed of two components for signal and background labelled 'Sig' and 'Bkg'

$$\mathcal{N}_{\mathrm{Total}}\mathcal{P}_{\mathrm{Total}} = \mathcal{N}_{\mathrm{Sig}}\mathcal{P}_{\mathrm{Sig}} + \mathcal{N}_{\mathrm{Bkg}}\mathcal{P}_{\mathrm{Bkg}}, \quad (5.22)$$

where $\mathcal{N}$ are normalisation factors. As the mass and decay time are uncorrelated the summed PDF can be decomposed into a product of a mass and a decay time PDF. The decay time PDF describes the conditional distributions of the decay time and its dependent observable dimensions, the decay time resolution estimate σ_t, the flavour tags $d_{\{\mathrm{OS,SS}\pi\}}$, and their associated mistag probability estimates $\eta_{\{\mathrm{OS,SS}\pi\}}$.

$$\mathcal{P}_{\mathrm{Sig/Bkg}}\left(m_{J/\psi K^0_{\mathrm{S}}}, t, \sigma_t, d_{\mathrm{OS}}, d_{\mathrm{SS}\pi}, \eta_{\mathrm{OS}}, \eta_{\mathrm{SS}\pi}\right) = \mathcal{P}_{\mathrm{Sig/Bkg}}\left(m_{J/\psi K^0_{\mathrm{S}}}\right) \cdot \mathcal{P}_{\mathrm{Sig/Bkg}}(t, \sigma_t, d_{\mathrm{OS}}, d_{\mathrm{SS}\pi}, \eta_{\mathrm{OS}}, \eta_{\mathrm{SS}\pi}) \quad (5.23)$$

As shown in Sec. 5.6.2 the per-event mistag estimates are uncorrelated to the reconstructed decay time. Hence, the signal decay time PDF can be further decomposed into a product of the conditional decay time PDF $\mathcal{P}_{\mathrm{Sig}}(t, d_{\mathrm{OS}}, d_{\mathrm{SS}\pi} \mid \sigma_t, \eta_{\mathrm{OS}}, \eta_{\mathrm{SS}\pi})$ describing the B meson time evolution as well as the CP violating effects, the PDF $\mathcal{P}_{\mathrm{Sig}}(\sigma_t)$ describing the resolution estimate, and the PDFs $\mathcal{P}_{\mathrm{Sig}}\left(\eta_{\{\mathrm{OS,SS}\pi\}}\right)$ describing the mistag probability estimates.

$$\mathcal{P}_{\mathrm{Sig}}(t, \sigma_t, d_{\mathrm{OS}}, d_{\mathrm{SS}\pi}, \eta_{\mathrm{OS}}, \eta_{\mathrm{SS}\pi}) = \mathcal{P}_{\mathrm{Sig}}(t, d_{\mathrm{OS}}, d_{\mathrm{SS}\pi} \mid \sigma_t, \eta_{\mathrm{OS}}, \eta_{\mathrm{SS}\pi}) \cdot \mathcal{P}_{\mathrm{Sig}}(\sigma_t) \cdot \mathcal{P}_{\mathrm{Sig}}(\eta_{\mathrm{OS}}) \cdot \mathcal{P}_{\mathrm{Sig}}(\eta_{\mathrm{SS}\pi}) \quad (5.24)$$

As the background decay time PDF does not depend on the mistag probability distributions, only the decay time error estimate enters the conditional decay time

PDF.

$$\mathcal{P}_{\text{Bkg}}(t, \sigma_t, d_{\text{OS}}, d_{\text{SS}\pi}, \eta_{\text{OS}}, \eta_{\text{SS}\pi}) = \\ \mathcal{P}_{\text{Bkg}}(t, d_{\text{OS}}, d_{\text{SS}\pi} \mid \sigma_t) \cdot \mathcal{P}_{\text{Bkg}}(\sigma_t) \cdot \mathcal{P}_{\text{Bkg}}(\eta_{\text{OS}}) \cdot \mathcal{P}_{\text{Bkg}}(\eta_{\text{SS}\pi}) \quad (5.25)$$

With this general structure being outlined, each single dimension and the parametrisation of the signal and background components are explained. The utilised PDFs are listed and it is explained which parameters are shared in the categories of the simultaneous fit to the different data subsamples (cf. Sec. 5.2).

Mass

The **signal** mass distribution is modelled using a Hypatia PDF. Individual parameters are chosen for the track types DD and LL. The parameter ζ is always fixed to zero. The values of the tail parameters a_1, a_2, n_1, n_2 and of the parameter λ are determined on simulated data and fixed to these values in the fit.

The **background** component is described by a single exponential PDF. The parameter α is shared among all subsamples except for DD and LL.

Decay time

The conditional **signal** decay time PDF is given by

$$\mathcal{P}_{\text{Sig}}(t, d_{\text{OS}}, d_{\text{SS}\pi} \mid \sigma_t, \eta_{\text{OS}}, \eta_{\text{SS}\pi}) \\ = \varepsilon_{\text{Sig}}^{\text{AU,EB}}(t') \cdot \left(\mathcal{P}_{\text{Sig}}(t', d_{\text{OS}}, d_{\text{SS}\pi} \mid \eta_{\text{OS}}, \eta_{\text{SS}\pi}) \otimes \mathcal{R}_{\text{Sig}}(t - t') \right) , \quad (5.26)$$

where the acceptance function $\varepsilon_{\text{Sig}}^{\text{AU,EB}}$ (cf. Sec. 5.5.2) is implemented using cubic splines [96] and the resolution model $\mathcal{R}_{\text{Sig}}(t - t')$ (cf. Sec. 5.5.1) is convolved with the B physics PDF.

In the following the B physics PDF is explained in detail. The theoretical distributions—neglecting all experimental effects—for B^0 and $\overline{B}^0$ mesons ($\mathcal{P}_{\text{true}}^{B^0}(t')$ and $\mathcal{P}_{\text{true}}^{\overline{B}^0}(t')$) are given by (cf. Eq. (2.25))

$$\begin{aligned} \mathcal{P}_{\text{true}}^{B^0}(t') &= \frac{1}{\mathcal{N}_{t'}^{B^0}} \mathrm{e}^{-t'/\tau} \left(1 - S \sin(\Delta m_d t) + C \cos(\Delta m_d t)\right) , \\ \mathcal{P}_{\text{true}}^{\overline{B}^0}(t') &= \frac{1}{\mathcal{N}_{t'}^{\overline{B}^0}} \mathrm{e}^{-t'/\tau} \left(1 + S \sin(\Delta m_d t) - C \cos(\Delta m_d t)\right) , \end{aligned} \quad (5.27)$$

with normalisation factors

$$\begin{aligned} \mathcal{N}_{t'}^{B^0} &= \int_{t_{\min}}^{t_{\max}} \mathrm{d}t \, \mathrm{e}^{-t'/\tau} \left(1 - S \sin(\Delta m_d t) + C \cos(\Delta m_d t)\right) \quad \text{and} \\ \mathcal{N}_{t'}^{\overline{B}^0} &= \int_{t_{\min}}^{t_{\max}} \mathrm{d}t \, \mathrm{e}^{-t'/\tau} \left(1 + S \sin(\Delta m_d t) - C \cos(\Delta m_d t)\right) . \end{aligned} \quad (5.28)$$

Here, $t_{\min}$ and $t_{\max}$ are the lower and upper limits of the analysed decay time range (cf. Tab. 5.1) and the parameter τ is the measured B^0 lifetime. The conditional PDFs for true B^0 and $\overline{B}^0$ mesons can now be written as

$$\begin{aligned} \mathcal{P}_{\text{true}}\left(t' \,\middle|\, B^0\right) &= \frac{\mathcal{N}^{B^0}_{t'}}{\mathcal{N}_{t'}} \mathcal{P}^{B^0}_{\text{true}}(t') \;, \\ \mathcal{P}_{\text{true}}\left(t' \,\middle|\, \overline{B}^0\right) &= \frac{\mathcal{N}^{\overline{B}^0}_{t'}}{\mathcal{N}_{t'}} \mathcal{P}^{\overline{B}^0}_{\text{true}}(t') \;, \end{aligned} \tag{5.29}$$

with the normalisation factor

$$\mathcal{N}_{t'} = \mathcal{N}^{B^0}_{t'} + \mathcal{N}^{\overline{B}^0}_{t'} \;. \tag{5.30}$$

A possible difference in the B^0 and $\overline{B}^0$ production rates R_B and $R_{\overline{B}^0}$ is treated by introducing the production asymmetry

$$A_P = \frac{R_{\overline{B}^0} - R_{B^0}}{R_{\overline{B}^0} + R_{B^0}} \,, \tag{5.31}$$

leading to modified conditional PDFs

$$\begin{aligned} \mathcal{P}_{\text{true}}\left(t' \,\middle|\, B^0\right) &= \frac{\mathcal{N}^{B^0}_{t'}}{\mathcal{N}_{t'}} (1 - A_P) \mathcal{P}^{B^0}_{\text{true}}(t') \quad \text{and} \\ \mathcal{P}_{\text{true}}\left(t' \,\middle|\, \overline{B}^0\right) &= \frac{\mathcal{N}^{\overline{B}^0}_{t'}}{\mathcal{N}_{t'}} (1 + A_P) \mathcal{P}^{\overline{B}^0}_{\text{true}}(t') \;. \end{aligned} \tag{5.32}$$

As the production flavour is unknown under experimental conditions the measurement depends on the flavour tagging information of the OS and SSπ tagging algorithms to decide whether the B meson was produced as B^0 or $\overline{B}^0$. With ω_i is short for the calibrated mistag probability $\omega(\eta_i)$ the PDF is then given as

$$\begin{aligned} \mathcal{P}(t', d_{\text{OS}}, d_{\text{SS}\pi} \mid \omega_{\text{OS}}, \omega_{\text{SS}\pi}) = \\ \delta_{d_{\text{OS}},+1} \delta_{d_{\text{SS}\pi},+1} \mathcal{P}\left(t' \,\middle|\, +1, +1, \omega_{\text{OS}}, \omega_{\text{SS}\pi}\right) \;, \\ + \delta_{d_{\text{OS}},+1} \delta_{d_{\text{SS}\pi},-1} \mathcal{P}\left(t' \,\middle|\, +1, -1, \omega_{\text{OS}}, \omega_{\text{SS}\pi}\right) \;, \\ + \delta_{d_{\text{OS}},-1} \delta_{d_{\text{SS}\pi},+1} \mathcal{P}\left(t' \,\middle|\, -1, +1, \omega_{\text{OS}}, \omega_{\text{SS}\pi}\right) \;, \\ + \delta_{d_{\text{OS}},-1} \delta_{d_{\text{SS}\pi},-1} \mathcal{P}\left(t' \,\middle|\, -1, -1, \omega_{\text{OS}}, \omega_{\text{SS}\pi}\right) \;, \end{aligned} \tag{5.33}$$

with

$$\begin{aligned}
&\mathcal{P}(t' \,|\, +1,+1,\omega_{\mathrm{OS}},\omega_{\mathrm{SS}\pi}) = \\
&\qquad \left(1-\omega_{\mathrm{OS}}^{B^0}\right)\left(1-\omega_{\mathrm{SS}\pi}^{\overline{B}^0}\right)\mathcal{P}_{\mathrm{true}}(t' \,|\, B^0)\,\omega_{\mathrm{OS}}^{B^0}\,\omega_{\mathrm{SS}\pi}^{\overline{B}^0}\,\mathcal{P}_{\mathrm{true}}(t' \,|\, \overline{B}^0)\,, \\
&\mathcal{P}(t' \,|\, +1,-1,\omega_{\mathrm{OS}},\omega_{\mathrm{SS}\pi}) = \\
&\qquad \left(1-\omega_{\mathrm{OS}}^{B^0}\right)\omega_{\mathrm{SS}\pi}^{\overline{B}^0}\,\mathcal{P}_{\mathrm{true}}(t' \,|\, B^0)\,\omega_{\mathrm{OS}}^{B^0}\left(1-\omega_{\mathrm{SS}\pi}^{\overline{B}^0}\right)\mathcal{P}_{\mathrm{true}}(t' \,|\, \overline{B}^0)\,, \\
&\mathcal{P}(t' \,|\, -1,+1,\omega_{\mathrm{OS}},\omega_{\mathrm{SS}\pi}) = \\
&\qquad \omega_{\mathrm{OS}}^{B^0}\left(1-\omega_{\mathrm{SS}\pi}^{\overline{B}^0}\right)\mathcal{P}_{\mathrm{true}}(t' \,|\, B^0)\left(1-\omega_{\mathrm{OS}}^{B^0}\right)\omega_{\mathrm{SS}\pi}^{\overline{B}^0}\,\mathcal{P}_{\mathrm{true}}(t' \,|\, \overline{B}^0)\,, \text{ and} \\
&\mathcal{P}(t' \,|\, -1,-1,\omega_{\mathrm{OS}},\omega_{\mathrm{SS}\pi}) = \\
&\qquad \omega_{\mathrm{OS}}^{B^0}\,\omega_{\mathrm{SS}\pi}^{\overline{B}^0}\,\mathcal{P}_{\mathrm{true}}(t' \,|\, B^0)\left(1-\omega_{\mathrm{OS}}^{B^0}\right)\left(1-\omega_{\mathrm{SS}\pi}^{\overline{B}^0}\right)\mathcal{P}_{\mathrm{true}}(t' \,|\, \overline{B}^0)\,.
\end{aligned} \tag{5.34}$$

Eq. (5.33) only contains the PDF to model decay time distributions of B candidates where tagging information from both tagging algorithms are available. If one of the taggers does not provide an output, i.e. the event falls into the OS or SS category, the formulas can easily be adapted by setting $d_{\{\mathrm{OS},\mathrm{SS}\pi\}} = 0$ and/or $\omega_{\{\mathrm{OS},\mathrm{SS}\pi\}} = 0.5$. The expression simplifies when explicitly implementing the OS and SSπ tag decisions

$$\begin{aligned}
&\mathcal{P}(t' \mid d_{\mathrm{OS}}, d_{\mathrm{SS}\pi}, \omega_{\mathrm{OS}}, \omega_{\mathrm{SS}\pi}) = \\
&\quad \left(\frac{1+d_{\mathrm{OS}}}{2} - d_{\mathrm{OS}}\omega_{\mathrm{OS}}^{B^0}\right)\left(\frac{1+d_{\mathrm{SS}\pi}}{2} - d_{\mathrm{SS}\pi}\omega_{\mathrm{SS}\pi}^{B^0}\right)\mathcal{P}_{\mathrm{true}}\left(t' \,\middle|\, B^0\right) \\
&+ \left(\frac{1-d_{\mathrm{OS}}}{2} + d_{\mathrm{OS}}\omega_{\mathrm{OS}}^{\overline{B}^0}\right)\left(\frac{1-d_{\mathrm{SS}\pi}}{2} - d_{\mathrm{SS}\pi}\omega_{\mathrm{SS}\pi}^{\overline{B}^0}\right)\mathcal{P}_{\mathrm{true}}\left(t' \,\middle|\, \overline{B}^0\right)\,.
\end{aligned} \tag{5.35}$$

Substituting $\mathcal{P}_{\mathrm{true}}\left(t' \,\middle|\, B^0\right)$ and $\mathcal{P}_{\mathrm{true}}\left(t' \,\middle|\, \overline{B}^0\right)$ making use of Eq. (5.32) and making use of the definition of the tagging asymmetry $\Delta\omega = \omega^{B^0} - \omega^{\overline{B}^0}$, Eq. (5.35) can be summarised as

$$\begin{aligned}
&\mathcal{P}(t', d_{\mathrm{OS}}, d_{\mathrm{SS}\pi} \,|\, \eta_{\mathrm{OS}}, \eta_{\mathrm{SS}\pi}) = \\
&\sum_{d'}\left[\prod_j \zeta(d_j, \eta_j, d')\right](1-d'A_P)\,\mathrm{e}^{-t'/\tau}\left\{1 - d'S_{J/\psi K^0_{\mathrm{S}}}\sin(\Delta m_d t') + d'\cos(\Delta m_d t')\right\},
\end{aligned} \tag{5.36}$$

with

$$\zeta\left(d_j, \eta_j, d'\right) = 1 + d_j\left(1 - 2\left[\omega(\eta_j) + d'\frac{\Delta\omega(\eta_j)}{2}\right]\right)\,, \tag{5.37}$$

where the calibration of the mistag estimates is implied by $\omega(\eta)$ and $\Delta\omega(\eta)$ and d' takes the value $+1$ (-1) for the B^0 $(\overline{B}^0)$ signal component.

The **background** decay time distribution is modelled using sums of exponential decay functions. Three decay PDFs are used to describe the distributions in the LL and the (DD and OS) subsamples. The sum of two decay PDFs is used to

parametrise the PDF describing the (DD and (SS or BS)) subsamples. The PDF parameters including the pseudo-lifetimes are shared among all categories except for DD and LL. In the DD subsample also individual parameters are chosen depending on the tagging category.

The applied resolution model is the same as for the signal component.

Decay time error estimate

For most subsamples the **signal** component's distribution is parametrised using two lognormal PDFs. The lognormal PDFs in the (LL and OS) subsample share a common median parameter. For candidates lying in the (LL and (SS or BS)) subsamples a single lognormal PDF is sufficient to describe the decay time error estimate distribution. Individual parameters are chosen depending on the track type and tagging categories, and in case of the (DD and OS) category, also on the trigger category.

The **background** PDF is composed of two lognormal distributions. In the LL subsample individual parameters are chosen depending on the track type and tagging categories. Candidates lying in the (DD and OS and AU) subsample only share parameters in the 11 and 12 categories. In all other subsamples the parameters are shared except for the track type category.

The parameter values are determined in a multi-dimensional fit to the mass, decay time, and decay time error estimate distributions and subsequently fixed in the nominal fit to reduce fit times.

Mistag estimate

The complicated shapes of the mistag estimate distributions have to be modelled empirically. Popular approaches to model non-parametric distributions are e.g. Gaussian kernel estimations and splines [96]. The later one is used here. Splines are piece-wise defined polynomials parametrised by interval boundaries (*knots*), values at these knots, and boundary conditions to ensure a continuous and smooth function. To model the mistag estimate distributions cubic splines are used as base splines.

For n knots, there are $n+2$ base splines, and accordingly $n+2$ fit parameters modelling the shape of the resulting PDF. The knot positions are chosen arbitrarily at points of noticeable changes in the shape of the described distributions.

The used knots for the η_{OS} and $\eta_{\mathrm{SS}\pi}$ distributions are

$$\begin{aligned}\text{OS knots} &= \{0.06, 0.10, 0.14, 0.165, 0.23, 0.3, 0.34, 0.36, 0.42, 0.44, 0.48\},\\ \text{SS}\pi\text{ knots} &= \{0.16, 0.26, 0.36, 0.41, 0.46, 0.482279\}.\end{aligned}$$

The explanation for the exceptional value of the last SSπ knot can be found in the pre-calibration applied. Originally, the SSπ mistag estimates are cut at values above 0.44. The pre-calibration then shifts this boundary towards the given value (Sec. 4.3.3). Likewise, OS candidates with a mistag estimate larger than 0.48 are

Table 5.22 – Correlations and their 95 % CLs between OS and SSπ mistag estimates.

	Signal		Background	
	$\rho_{\eta_{\mathrm{OS}},\eta_{\mathrm{SS}\pi}}$	95 % CL	$\rho_{\eta_{\mathrm{OS}},\eta_{\mathrm{SS}\pi}}$	95 % CL
DD	0.0731	$(0.0306, 0.1155)$	0.0555	$(0.0139, 0.0972)$
LL	0.0854	$(0.0270, 0.1454)$	-0.0465	$(-0.219, 0.136)$
combined	0.077	$(0.041, 0.112)$	0.0507	$(0.0101, 0.0919)$

Table 5.23 – Correlations and their 95 % CLs between the mistag estimates $\eta_{\mathrm{OS/SS}\pi}$ and the reconstructed B^0 decay time.

	Signal		Background	
	$\rho_{\eta,t}$	95 % CL	$\rho_{\eta,t}$	95 % CL
OS	-0.0046	$(-0.0375, 0.0272)$	-0.0601	$(-0.1086, -0.0135)$
SSπ	0.0223	$(-0.0104, 0.0535)$	-0.002	$(-0.048, 0.044)$

considered as OS untagged. This choice was made to speed up the fit time and to ensure fit stability. As the candidates removed by this cut hold large mistags, the reduction of the effective tagging efficiency is found to be insignificant.

The spline parameters for **signal** and **background** are determined in a multi-dimensional fit including mass, decay time, and mistag estimate and are fixed later on, to achieve a better fit performance. Both, the OS and the SSπ mistag distributions are fitted using cubic splines with different spline parameters for DD and LL and otherwise sharing them through all categories. Only in the signal OS distributions the differences depending on the track type are negligible so the parameters are shared in the DD and LL categories.

Correlation between OS and SSπ mistag estimates To check if the two dimensions of η_{OS} and $\eta_{\mathrm{SS}\pi}$ factorise, the linear Pearson correlation coefficient ρ is calculated on the sWeighted nominal data set. To clarify the significance of the values the bootstrap method (i.e. 'random sampling with replacement', cf. e.g. [99]) is used to get 95 % CL intervals for the correlation coefficients. Tab. 5.22 lists the calculated linear correlation coefficients separately for DD and LL as well as combined while always distinguishing between signal and background. Overall the linear correlations are small, so the factorisation is valid.

Correlation between decay time and OS/SSπ mistag estimates The same ansatz as before is chosen to test the correlation between the decay time distributions and the mistag estimates. Tab. 5.23 shows no significant correlations between the decay time and the OS/SSπ mistag estimates.

5.6.3 Experimenter's bias

To minimise a potential experimenter's bias, a blinding transformation is applied to the *CP* observables $S_{J/\psi K^0_S}$ and $C_{J/\psi K^0_S}$ by adding an obfuscated offset to the fit parameters. This does not affect the uncertainty estimates and still allows to compare and reproduce the fit outcome. The offset is drawn from a uniform distribution using a random number generator. The random seed is generated using a so called blinding string. To ensure a sufficient ambiguity the range of the uniform distribution is chosen to be $[-2, 2]$. The blinding string applied to conceal the estimated value of $S_{J/\psi K^0_S}$ is `SJpsiKS2011und2012` and for $C_{J/\psi K^0_S}$ it is chosen to be `CJpsiKS2011und2012`.

5.6.4 Fitter validation

The likelihood model described before and its code implementation is validated using ToyMC simulated and regular MC simulated data.

Pseudo-experiments

An external ToyMC generator [100] is employed to scrutinise the PDF used in the fit. It generates distributions for the dimensions mass, decay time, decay time error estimate, and mistag estimate, correctly models the per-event tag and mistag for two tagging algorithms, comprises tagging and production asymmetries, as well as tagged background events. Making use of the signal to background ratios found on data a simulated data set is generated and fitted afterwards. No significant deviations from the generated values are found.

In addition the nominal PDF is used to sample distributions. The subsequent fit to the simulated data allows to check if the fit's parameter values and uncertainties estimates are unbiased. In the generation the *CP* parameters are unblinded and set to $S_{J/\psi K^0_S} = 0.7$ and $C_{J/\psi K^0_S} = 0.03$. All other parameters are set to the values estimated on data using the nominal fit model. The results from 1000 iterations of generating an fitting are shown in Fig. 5.10. No bias is observable.

Signal MC

To further validate the nominal fit model, a fit on signal MC (Sec. 5.2.5) is performed and the fit results are compared to the generation values of $S^{\text{Gen}}_{J/\psi K^0_S} = 0.699\,716\,075$, $C^{\text{Gen}}_{J/\psi K^0_S} = 0$, and $\tau^{\text{Gen}}_{B^0} = 1.519\,068\,\text{ps}$ (see Tab. 5.13). Eq. (5.38) presents the results. Both *CP* parameters, as well as the B^0 lifetime are perfectly compatible with the generation values.

$$\begin{aligned} S^{\text{SigMC}}_{J/\psi K^0_S} &= 0.714 \pm 0.032\,, \\ C^{\text{SigMC}}_{J/\psi K^0_S} &= 0.012 \pm 0.028\,, \\ \tau^{\text{SigMC}}_{B^0} &= (1.521 \pm 0.009)\,\text{ps}\,. \end{aligned} \tag{5.38}$$

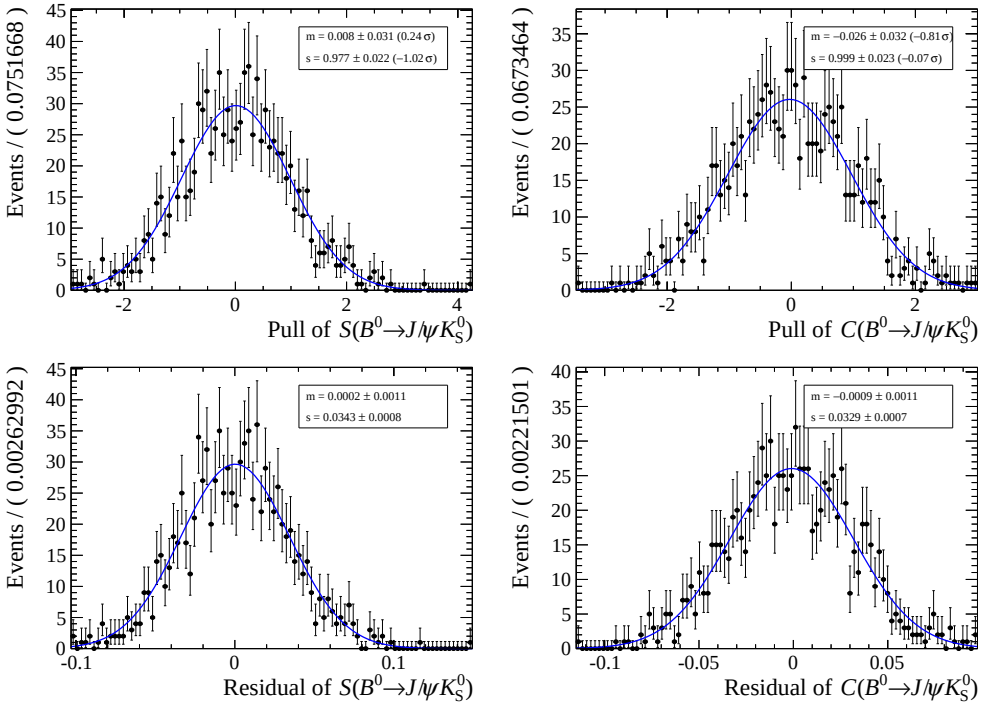

Figure 5.10 – Pull (top) and residual (bottom) distributions of $S_{J/\psi K^0_S}$ (left) and $C_{J/\psi K^0_S}$ (right) in the fitter validation using ToyMC.

Cocktail MC

Further, the fit model is tested on a simulated data set containing both signal and background. For this study, the signal MC sample is enriched with background events generated from the background PDF of the nominal fit model according to the signal to background ratio observed in data. The fit results are shown in Eq. (5.39). Again all measured parameters are perfectly compatible with the generation values.

$$\begin{aligned} S^{\text{CocktailMC}}_{J/\psi K^0_S} &= 0.722 \pm 0.029\,, \\ C^{\text{CocktailMC}}_{J/\psi K^0_S} &= 0.008 \pm 0.027\,, \\ \tau^{\text{CocktailMC}}_{B^0} &= (1.506 \pm 0.010)\,\text{ps}\,. \end{aligned} \tag{5.39}$$

5.7 Measurement of *CP* violation

Utilising the likelihood model presented in Sec. 5.6 an uEML fit is performed to the nominal data set (cf. Sec. 5.2.5). The MINUIT2 algorithm implemented in the ROOFIT (v3.60) framework from ROOT v5.34/18 is used to minimise the negative log-likelihood function with the 'minimize' routine and 'strategy 2'. MINOS is used for the estimation of the (asymmetric) parameter uncertainties.

Table 5.24 – Listing of parameters that are constrained in the fit.

Parameter	Value and uncertainty	Source
A_P^{11}	-0.0108 ± 0.0052	[101]
ΔA_P	0.0004 ± 0.0018	[42, 101]
Δm_d ($\hbar\,\mathrm{ps}^{-1}$)	0.510 ± 0.003	[33]
p_0^{OS}	0.3815 ± 0.0011	Sec. 4.3.2
p_1^{OS}	0.978 ± 0.012	
Δp_0^{OS}	0.0148 ± 0.0016	
Δp_1^{OS}	0.070 ± 0.018	
p_0^{SS}	0.4232 ± 0.0029	Sec. 4.3.3
p_1^{SS}	1.011 ± 0.064	
Δp_0^{SS}	-0.0026 ± 0.0043	
Δp_1^{SS}	-0.17 ± 0.10	

5.7.1 Constrained parameters

Several parameters are incorporated as external inputs. These parameters are constrained using Gaussian PDFs with the mean value fixed to the parameter's value and the Gaussian's width to the uncertainty. The constraint is implemented by multiplying the Gaussian PDFs to the total likelihood. Tab. 5.24 lists the constrained parameters as well as a reference to the source of the value and its uncertainty employed in the fit.

Individual production asymmetry values are used for the 11 and 12 subsamples. Using the recent LHCb measurement [101] of the production asymmetry as a function of the transverse momentum (p_{T}) and the pseudorapidity (η) the per-p_{T}-η-bin signal fractions $\varepsilon_i = {}^{f_i}/_{\sum_i f_i}$ of the nominal dataset are determined to calculate a weighted average of the production asymmetries

$$A_P = \sum_i \varepsilon_i A_{P,i}\,, \tag{5.40}$$

where f_i is the number of signal candidates per bin and $A_{P,i}$ the measured production asymmetry in bin i taken from Ref. [101]. This yields

$$\begin{aligned} A_P^{11} &= -0.0108 \pm 0.0052\,(\mathrm{stat}) \pm 0.0014\,(\mathrm{syst})\,, \\ A_P^{12} &= -0.0104 \pm 0.0051\,(\mathrm{stat}) \pm 0.0014\,(\mathrm{syst})\,. \end{aligned} \tag{5.41}$$

As the measurement has been performed on 7 TeV data only, the numbers for A_P^{11} and A_P^{12} are highly correlated. We therefore constraint A_P^{11} and ΔA_P in the fit and model $A_P^{12} = A_P^{11} + \Delta A_P$ with $\Delta A_P = 0.0004 \pm 0.0018\,(\mathrm{syst})$, where the systematic uncertainty accounts for the production asymmetry differences observed for the two data-taking conditions in LHCb's recent measurement of the semi-leptonic CP asymmetry [42].

5.7.2 Fixed parameters

As mentioned before, various parameters are fixed in the nominal fit. These are the mass parameters obtained on simulated data (Tab. A.3), the parameters describing the distribution of the decay time error estimates (Tab. A.4), the parameters of the cubic spline functions used to model the OS and SSπ mistag estimate distributions (Tab. A.5 and A.6), the calibration parameters of the decay time resolution model (Tab. A.7) and the parameters of the cubic spline functions utilised to parametrise the shape of the lower decay time acceptance (Tab. A.8). All tables are collected in Appendix A.2.1.

5.7.3 Fit results

Employing all constrained and fixed parameters the likelihood describing the seven fit dimensions is fitted to the selected $B^0 \to J/\psi K^0_S$ candidates using the uEML method. For the most interesting *CP* parameters, $S_{J/\psi K^0_S}$ and $C_{J/\psi K^0_S}$, the mass difference Δm_d, and the lifetime of the B^0 candidates, the fit yields

$$\begin{aligned} S_{J/\psi K^0_S} &= 0.729 \pm 0.035\,, \\ C_{J/\psi K^0_S} &= -0.033 \pm 0.032\,, \\ \rho(S_{J/\psi K^0_S}, C_{J/\psi K^0_S}) &= 0.483\,, \\ \Delta m_d &= (0.5100 \pm 0.0030)\,\hbar\,\mathrm{ps}^{-1} \quad (\textit{constrained})\,, \\ \tau &= (1.479 \pm 0.009)\,\mathrm{ps}\,. \end{aligned} \tag{5.42}$$

Tab. A.9 to A.11 in Appendix A.2.2 give the fitted signal and background candidate numbers, the mass parameter estimates, and the results for the decay time background category parameters. Furthermore, Tab. 5.25 shows the results for the tagging parameters and the production asymmetry.

The B meson candidate's distributions in mass, decay time, decay time estimate, and OS and SSπ mistag estimates are shown in Fig. 5.11 including the PDF projections.

Eventually, the decay time dependent signal-yield asymmetry

$$\mathcal{A} = \frac{(N_{\overline{B}^0} - N_{B^0})}{(N_{\overline{B}^0} + N_{B^0})} \tag{5.43}$$

where N_{B^0} ($N_{\overline{B}^0}$) is the number of $B^0 \to J/\psi K^0_S$ signal candidates tagged as B^0 ($\overline{B}^0$) is presented in Fig. 5.12.

Visualisations of the likelihood shape are presented in 1- and 2-dimensional likelihood profile scans in Fig. 5.13. The correlation matrix is provided in Fig. 5.14 including the *CP* observables $S_{J/\psi K^0_S}$ and $C_{J/\psi K^0_S}$, the B^0 meson lifetime τ, as well as the most relevant parameters from the flavour tagging calibration and production asymmetries.

Following the SM predictions of no direct *CP* violation and no *CP* violation in mixing the parameter $C_{J/\psi K^0_S}$ can be fixed to zero in the likelihood description. Repeating the fit under these condition yields

$$S_{J/\psi K^0_S} = \sin(2\beta) = 0.746 \pm 0.030\,. \tag{5.44}$$

Table 5.25 – Results for the tagging parameters and the production asymmetries in the nominal fit. All parameters are constraint in the fit as described in Sec. 5.7.1.

Parameter	Value
p_0^{OS}	0.3815 ± 0.0011
p_1^{OS}	0.977 ± 0.012
Δp_0^{OS}	0.0148 ± 0.0016
Δp_1^{OS}	0.073 ± 0.018
$p_0^{\mathrm{SS}\pi}$	0.4228 ± 0.0028
$p_1^{\mathrm{SS}\pi}$	1.01 ± 0.06
$\Delta p_0^{\mathrm{SS}\pi}$	-0.002 ± 0.004
$\Delta p_1^{\mathrm{SS}\pi}$	-0.16 ± 0.09
A_P^{11}	-0.014 ± 0.005
ΔA_P	0.000 ± 0.002

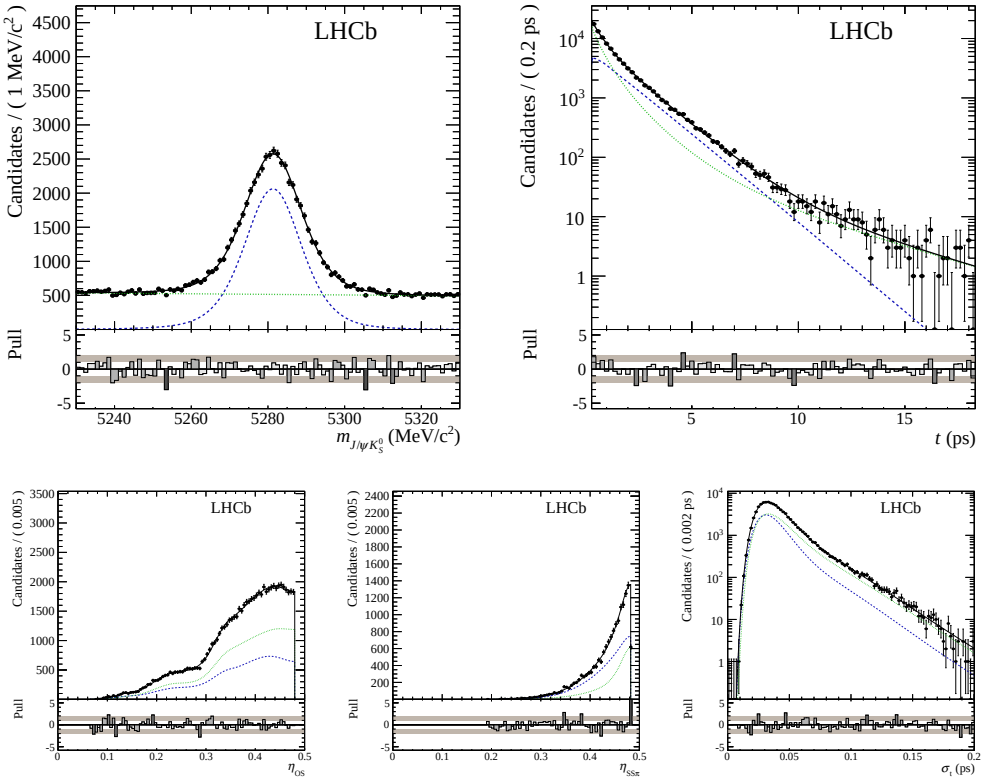

Figure 5.11 – Plots of the $B^0 \to J/\psi K^0_S$ data sample with the projected PDF and pull distributions. Shown is the reconstructed mass $m_{J/\psi K^0_S}$ (top left) and decay time t (top right, logarithmic), per-event mistag (bottom left η_{OS}, bottom center $\eta_{SS\pi}$), and decay time error σ_t (bottom right, logarithmic). Besides the data points and the full PDF (solid black) the projections of the signal (dashed blue) and the background (dotted green) are shown.

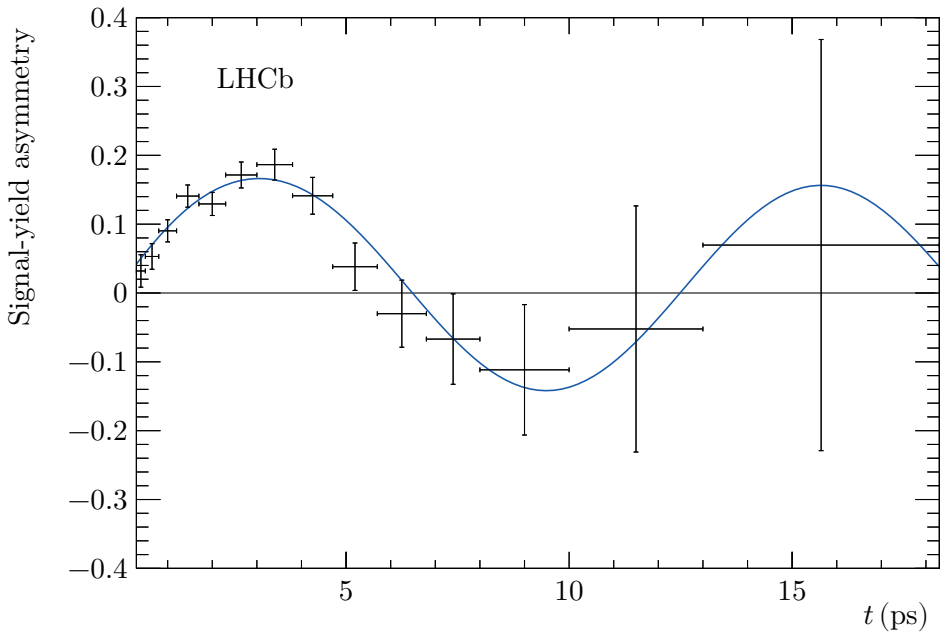

Figure 5.12 – Time-dependent signal-yield asymmetry $(N_{\overline{B}^0} - N_{B^0})/(N_{\overline{B}^0} + N_{B^0})$. Here, $N_{B^0}(N_{\overline{B}^0})$ is the number of $B^0 \to J/\psi K^0_S$ decays with a B^0 ($\overline{B}^0$) flavour tag. The data points are obtained with the sPlot technique [89], assigning signal weights to the events based on a fit to the reconstructed mass distribution. The solid curve is the projection of the signal PDF.

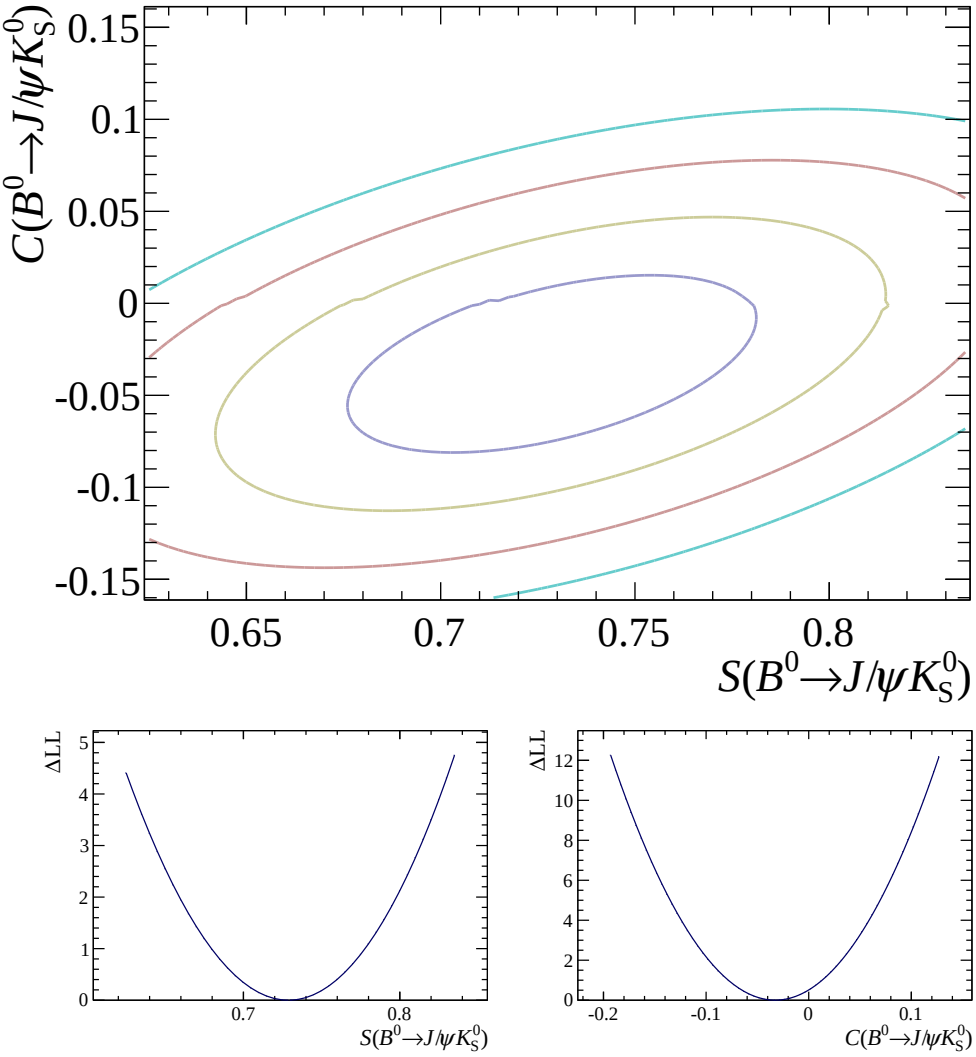

Figure 5.13 – One and two dimensional likelihood profile scans for $S_{J/\psi K^0_S}$ and $C_{J/\psi K^0_S}$.

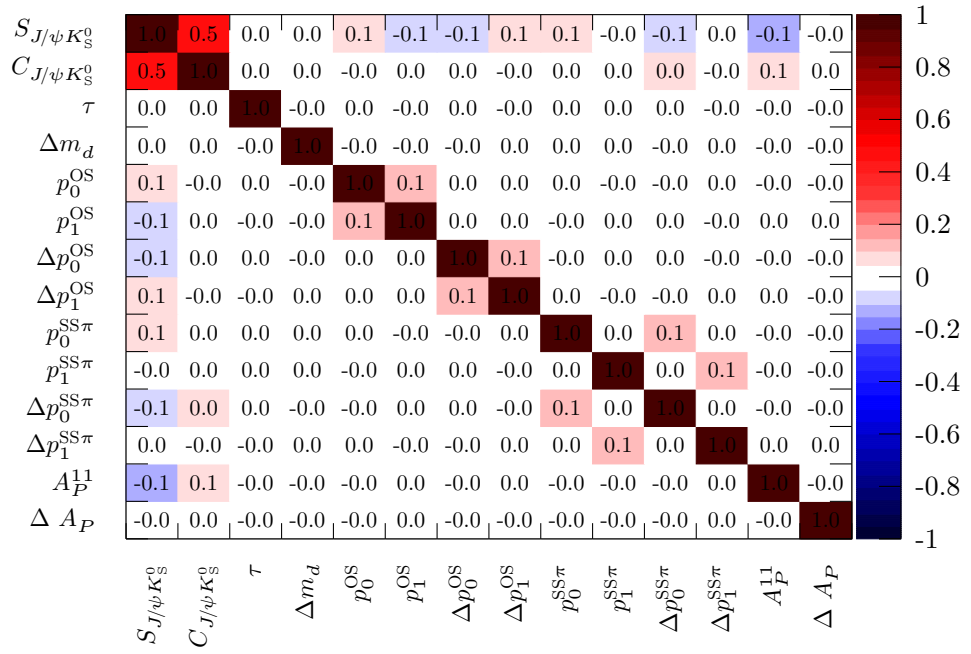

Figure 5.14 – Visualised correlation matrix of the fit parameters in the nominal fit. Positive correlations are represented by the red palette on the z-axis, while negative correlations are represented by the blue palette on the z-axis. The CP observables $S_{J/\psi K^0_S}$ and $C_{J/\psi K^0_S}$ as well as the B^0 lifetime τ are shown together with the most relevant parameters from the flavour tagging calibration and production asymmetries.

5.7.4 Kaon regeneration

The *CP* violation in the neutral kaon system as well as differences in the nuclear interactions of K^0 and $\overline{K}^0$ states with the detector material are not considered in the fit model [102].

The influence of both effects can be broken down into the accidentally reconstruction of K^0_{L} mesons decaying into two pion final states, thus leading to wrong-sign contributions to the decay rates (cf. Eq. (2.25)),

$$\frac{\Gamma(B^0 \to J/\psi K^0_{\mathrm{L}})}{\mathrm{e}^{-\Gamma t}} \propto \Big(1 + \sin(2\beta)\sin(\Delta m_d t)\Big)\,. \tag{5.45}$$

CP violation in the kaon system allows the suppressed decay of $K^0_{\mathrm{L}} \to \pi^+\pi^-$. The same applies when K^0_{L} mesons effectively decay into a two pion final state after transforming into a K^0_{S} state due to regeneration effects taking place in the interaction with the detector material.

With the *CP* violation in the kaon system being very small, as well as a small regeneration rate, both effects are expected to contribute in the same order at a sub-percent level.

Following the procedure described in Ref. [103], corrections are computed for $S_{J/\psi K^0_{\mathrm{S}}}$ and $C_{J/\psi K^0_{\mathrm{S}}}$ and are added to the results from the likelihood fit. The corrections are

$$\begin{aligned} \delta_{S_{J/\psi K^0_{\mathrm{S}}}} &= +0.002 \text{ and} \\ \delta_{C_{J/\psi K^0_{\mathrm{S}}}} &= -0.005\,. \end{aligned} \tag{5.46}$$

5.8 Studies of systematic effects

The determination of potential systematic uncertainties on the *CP* parameters complete the measurement.

The following section will describe the evaluation of systematic effects of the fit model and influences of the flavour tagging, the decay time resolution, the decay time acceptance, and several other inputs to the measurement of *CP* violation.

In Sec. 5.8.1 cross-checks are outlined to test the reproducibility and stability of the fit model. Studies to estimate the effect of various fit model properties are listed in Sec. 5.8.2 while Sec. 5.8.3 gives a summary of all found systematic effects.

5.8.1 Cross-checks

When performing cross-checks, either results obtained on different subsamples or results obtained from different methods on the same sample are compared. In both cases, the deviation of the difference in fit results in terms of its uncertainty is used as a measure of agreement.

When comparing results on different, distinct samples, the uncertainty on the difference is estimated by summing the uncertainties of the single results in

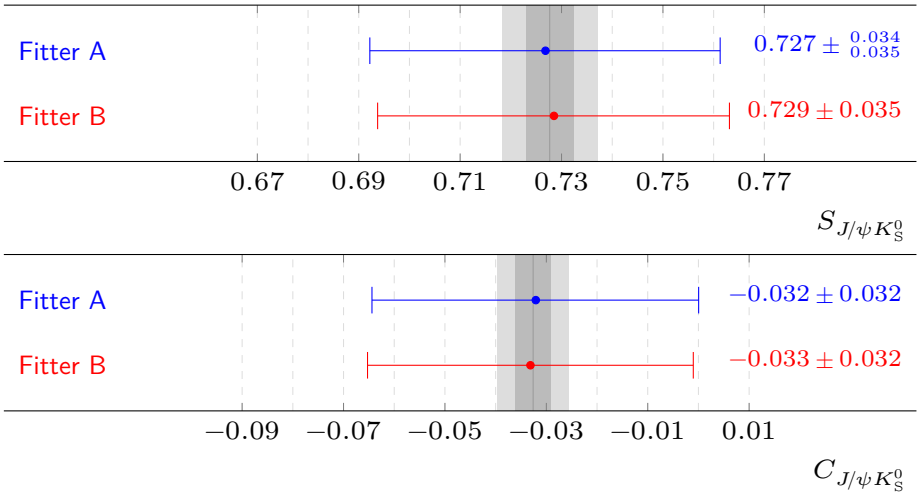

Figure 5.15 – Fit results for $S_{J/\psi K^0_S}$ and $C_{J/\psi K^0_S}$ for both fitter implementations. In blue (red) the result and the statistical error for Fitter A (B). The grey solid line shows the average of both fit results, while the filled grey area describes the uncertainty on the difference σ_Δ of the two results (darker grey $1\sigma_\Delta$, light grey $2\sigma_\Delta$). *Please note: The shown numbers are rounded following the PDG rules. The plot itself is produced using the full precision values.*

quadrature. In contrast, when applying different methods to the same sample, the compatibility of the results is compared by taking into account a full correlation of the data sets. Following Ref. [104], the uncertainty on the difference of the two results A and B on the same data set is defined as

$$\sigma^2_\Delta = \left|\sigma^2_A - \sigma^2_B\right| . \tag{5.47}$$

Again, both measurements can be interpreted as compatible if the uncertainty lies in the same order of magnitude as the difference of the central values.

Second fitter implementation

To provide a cross-check of the fitter implementation, two different, independent fitter implementations were developed by the author and another member of the working group. Being built up on the RooFit library they do not share any common code base. For simplification they will be denoted as *Fitter A* and *Fitter B*. Both fitters are tested against each other in the nominal fitter setup (Sec. 5.6). Applying the measure described before, the results from both fitters are in excellent agreement, as is shown in Fig. 5.15.

sPlot fit

As the background decay time model might influence the measurement, an sPlot fit is performed using the nominal signal mass PDF. As the standard Minuit/Hesse

error estimations in sPlot fits can lead to uncertainties with an incorrect coverage, an additional bootstrapping (cf. e.g. [99]) study is performed to arrive at correct estimates of uncertainties. The procedure followed is:

1. take the sWeighted data sample consisting of N events,
2. sample N randomly selected events with replacement into a new data sample,
3. perform a fit to the resulting sample to measure $S_{J/\psi K^0_S}$ and $C_{J/\psi K^0_S}$,
4. repeat the steps to obtain a distribution of the measured CP parameters.

Fig. 5.16 shows the fit result of the sPlot fit with the corresponding Hesse uncertainty estimates, as well as the nominal fit result. Additionally, the uncertainty estimates from the bootstrapping study are included. For the latter, the medians of the measured $S_{J/\psi K^0_S}$ and $C_{J/\psi K^0_S}$ distributions are chosen as central values, while the quoted uncertainties are the quantile-based estimates for two-sided 68.27 % quantiles of the same distribution. The resulting distributions based on 1000 bootstrapping iterations are presented in Fig. 5.17.

The central values resulting from the bootstrapped sPlot fits are very well compatible with the naive sPlot fit. Compared to the nominal fit this holds true for $C_{J/\psi K^0_S}$ while $S_{J/\psi K^0_S}$ is slightly lower. The uncertainty estimates of the bootstrapping study are slightly larger than the corresponding uncertainties from the nominal fit, but still in the same order of magnitude. In contrast, the uncertainty estimate of the naive sPlot fit for $S_{J/\psi K^0_S}$, should be larger or at the best equal of size compared to the nominal fit, but are found to be too small. Overall, the results of the sPlot fits and the nominal fit are well compatible.

Subsamples

To check for possible systematic effects, fits in different subsamples of the nominal data set are conducted. The cross-checks are performed in categories of track type (DD vs. LL), trigger requirement (AU vs. EB), tagging algorithm (OS vs. SS vs. BS), magnet polarity (Up vs. Down), and admixtures of those together with the year of data-taking (11 vs. 12). As a control sample the full data set is also split randomly into five disjoint subsets (Rndm1-5). Fig. 5.18 illustrates the outcome. No significant deviation is present.

Pure time-dependent and time-integrated fit

The fit is tested furthermore by disentangling the time-integrated and the time-dependent parts of it. To ensure a purely time-dependent extraction of the CP violating parameters a binned χ^2-fit to the signal CP asymmetry (cf. Fig. 5.12) is performed. The theoretical distribution $\mathcal{A}_{CP}(t)$ given in Eq. (2.35), modified to

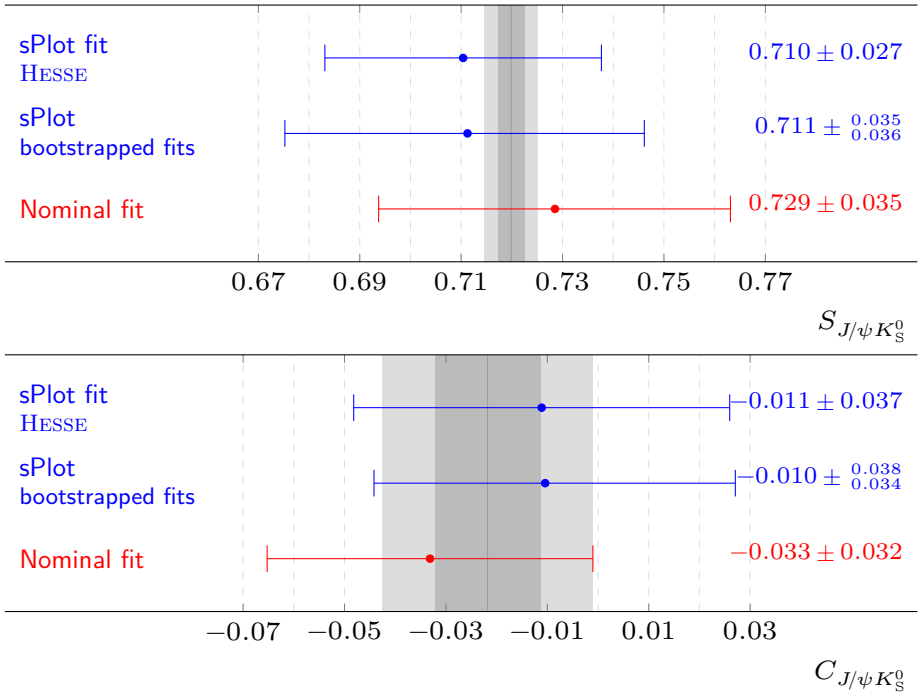

Figure 5.16 – Fit results for $S_{J/\psi K^0_S}$ and $C_{J/\psi K^0_S}$ from the sPlot fit and the nominal fit as a reference. In blue (red) the result and the statistical error for the sPlot fit (nominal fit)s. The grey solid line shows the average of the two below fit results, while the filled grey area describes the uncertainty on the difference σ_Δ of the two lower results (darker grey $1\sigma_\Delta$, light grey $2\sigma_\Delta$). *Please note: The shown numbers are rounded following the PDG rules. The plot itself is produced using the full precision values.*

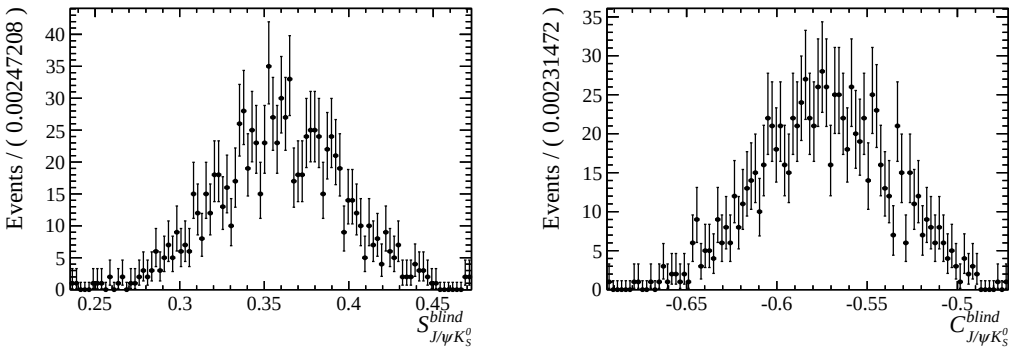

Figure 5.17 – Parameter distributions for $S^{\text{blind}}_{J/\psi K^0_S}$ and $C^{\text{blind}}_{J/\psi K^0_S}$ from sPlot fits to 1000 bootstrapped data samples. The study was performed with still blinded parameter values (cf. Sec. 5.6.3).

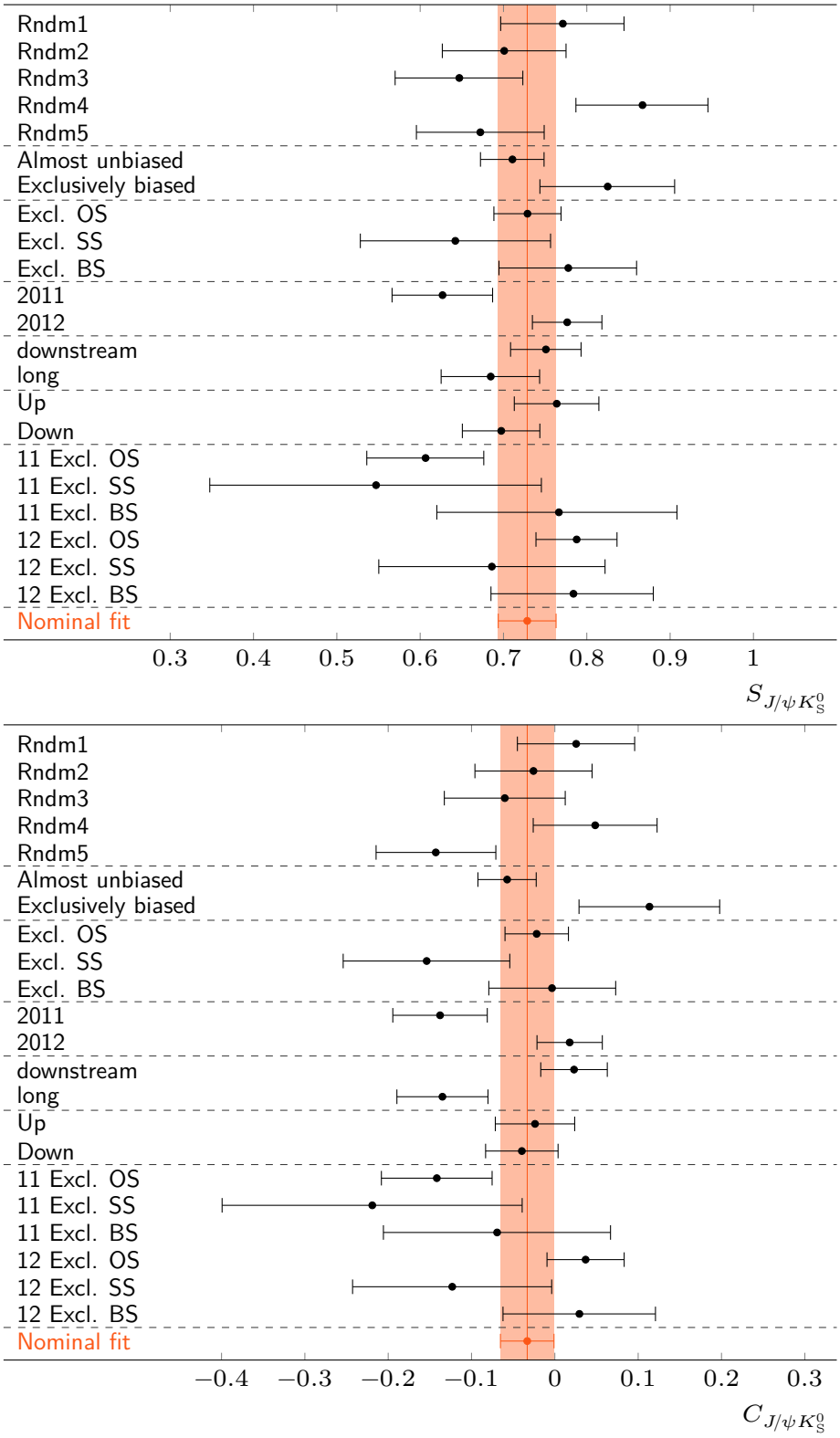

Figure 5.18 – Comparison of fit results of $S_{J/\psi K^0_S}$ and $C_{J/\psi K^0_S}$ for fits on various subsamples.

cover for tagging and production asymmetries results in

$$\mathcal{A}_{CP}^{\text{exp}} = \frac{\omega^{B^0} - \omega^{\overline{B}^0} + A_{\text{P}}^{11}\left(1 - \omega^{B^0} - \omega^{\overline{B}^0}\right) + \mathcal{A}_{CP}(t)\left(1 - \omega^{B^0} - \omega^{\overline{B}^0} + A_{\text{P}}^{11}(\omega^{B^0} - \omega^{\overline{B}^0})\right)}{1 + A_{\text{P}}^{11}\mathcal{A}_{CP}(t)}. \tag{5.48}$$

At this point the OS and SSπ mistag probabilities are combined on a per-event basis assuming true B^0 and $\overline{B}^0$ mesons. Using signal weights extracted by an sPlot fit on the mass distribution, the weighted averages of $\omega^{B^0} = 0.3869$ and $\omega^{\overline{B}^0} = 0.3777$ are incorporated while the values for A_{P}^{11} and Δm_d are taken as found in the nominal fit. This results in central values fully compatible to the ones extracted from the nominal fit

$$\begin{aligned} S_{J/\psi K_{\text{S}}^0} &= 0.713 \pm 0.053\,, \\ C_{J/\psi K_{\text{S}}^0} &= 0.003 \pm 0.055\,. \end{aligned}$$

Leaving the mass difference Δm_d floating in the fit has a large influence on the uncertainty on $C_{J/\psi K_{\text{S}}^0}$, resulting in

$$\begin{aligned} S_{J/\psi K_{\text{S}}^0} &= 0.718 \pm 0.053\,, \\ C_{J/\psi K_{\text{S}}^0} &= 0.040 \pm 0.077\,, \\ \Delta m_d &= (0.540 \pm 0.043)\,\hbar\,\text{ps}^{-1}\,. \end{aligned}$$

In the purely time-integrated approach the number of tagged B^0 and $\overline{B}^0$ signal candidates is counted on an sWeighted sample to compute the time-integrated CP asymmetry

$$\mathcal{A}_{CP}^{\text{int}} = \frac{N_{\overline{B}^0} - N_{B^0}}{N_{\overline{B}^0} + N_{B^0}} = 0.103 \pm 0.005\,. \tag{5.49}$$

Under the SM assumption of $C_{J/\psi K_{\text{S}}^0} = 0$ the relation

$$S_{J/\psi K_{\text{S}}^0}^{\text{int}} = \frac{\mathcal{A}_{CP}^{\text{int}} - (1 - \omega^{B^0} - \omega^{\overline{B}^0})A_{\text{P}}\mathcal{A}_{CP}^{\text{int}}(\omega^{B^0} - \omega^{\overline{B}^0})}{1 - \omega^{B^0} - \omega^{\overline{B}^0} - A_{\text{P}}\mathcal{A}_{CP}^{\text{int}} - \mathcal{A}_{CP}^{\text{int}}(\omega^{B^0} - \omega^{\overline{B}^0})} \cdot \frac{1 - (\Delta m_d \tau)^2}{\sin(\Delta m_d t_{\text{min}}) + \Delta m_d \tau \cos(\Delta m_d t_{\text{min}})}\,, \tag{5.50}$$

leads to

$$S_{J/\psi K_{\text{S}}^0}^{\text{int}} = 0.783 \pm 0.038\,,$$

where the lower integration limit t_{min} is employed and the values for the other parameters are handled as in the time-dependent case described before. Taking into account the correlation between the CP parameters $S_{J/\psi K_{\text{S}}^0}$ and $C_{J/\psi K_{\text{S}}^0}$ by

using the value for $C_{J/\psi K^0_S}$ found in the nominal fit, the previous equation extends by another summand,

$$S^{\text{int}}_{J/\psi K^0_S} = \text{Eq. (5.50)} + C_{J/\psi K^0_S} \frac{\Delta m_d \tau \sin(\Delta m_d t_{\text{min}}) + \cos(\Delta m_d t_{\text{min}})}{\sin(\Delta m_d t_{\text{min}}) + \Delta m_d \tau \cos(\Delta m_d t_{\text{min}})}\,, \quad (5.51)$$

resulting in

$$S^{\text{int}}_{J/\psi K^0_S} = 0.746 \pm 0.040\,.$$

5.8.2 Systematics

Systematic uncertainties resulting from the choice or the handling of the fit model, the flavour tagging calibration, decay time resolution and acceptance, and other ingredients to the measurement are summarised in the following section. All pull and residual distributions originating from the studies are collected in Appendix A.3. If not stated otherwise the *CP* parameter values are set to $S_{J/\psi K^0_S} = 0.7$ and $C_{J/\psi K^0_S} = 0.03$ in the pseudo-experiment (ToyMC) sample generation.

Fit model

A background tagging asymmetry i.e. a non-vanishing tagging asymmetry in the background candidates' sample is found and described in Sec. 5.4.2. A ToyMC study with 1000 iterations is performed to estimate the potential influence on the measurement of $S_{J/\psi K^0_S}$ and $C_{J/\psi K^0_S}$.

For each repetition a dataset is generated using the time-dependent asymmetries provided by the histograms shown in Fig. 5.3. The asymmetry is sampled by incorporating the bin contents and errors. As the decay time resolution model is assumed to not affect the outcome, an average decay time resolution model is incorporated. A significant bias is observed in both *CP* parameters (see Fig. A.1), thus the central value of the residual distributions is used as an estimate of the systematic uncertainties

$$\delta_{S_{J/\psi K^0_S}} = 0.0179 \text{ and } \delta_{C_{J/\psi K^0_S}} = 0.0015\,. \quad (5.52)$$

The influence of a correlation between the mass and the decay time is investigated using a ToyMC study. The nominal PDF model assumes no correlation, therefore the mass and decay time dimensions are directly multiplied. Using the signal MC sample the correlation between the mass and the decay time resolutions, defined as $m - m_{\text{true}}$ and $t - t_{\text{true}}$, is studied and depicted in Fig. 5.19 as binned 2-dimensional histograms as well as profile plots. While the correlation is insignificant for DD candidates, a small positive correlation is found for LL candidates. In a study with 250 iterations data are generated assuming the given correlation for LL candidates while fitted with the nominal model. The pull and residual plots shown in Fig. A.2 show no significant bias on the *CP* parameters.

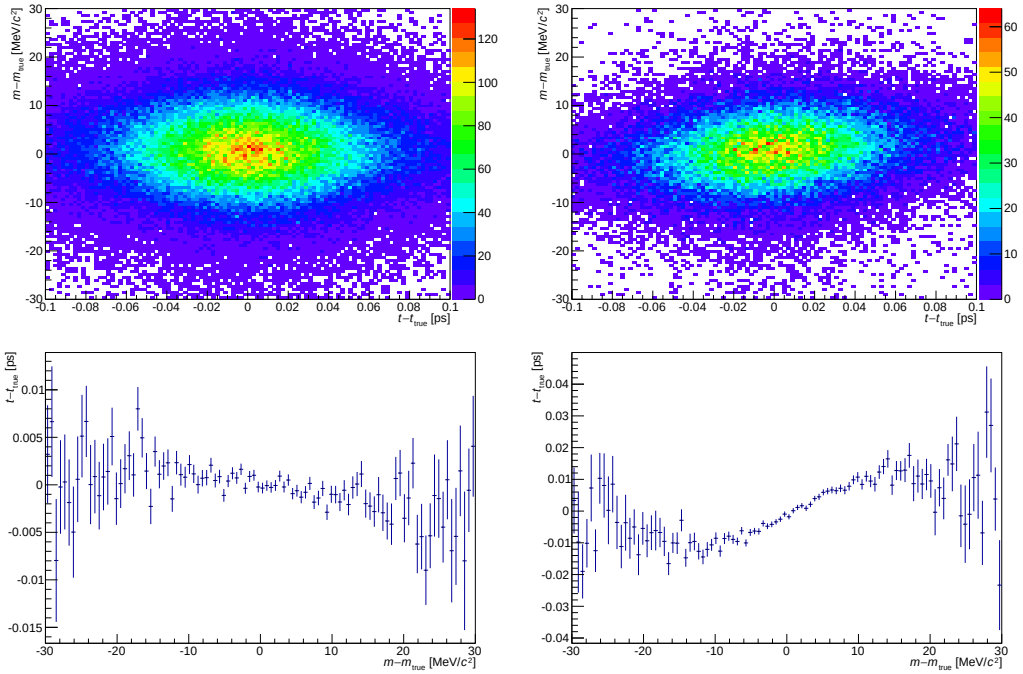

Figure 5.19 – Visualisation of the correlation between the mass and the decay time resolution defined $m - m_{\text{true}}$ and $t - t_{\text{true}}$. On top the binned 2-dimensional distribution is shown, while on the bottom profile plots show the average of the decay time resolution as a function of the mass resolution. Shown are the (left) DD and the (right) LL subsamples.

Flavour tagging

The statistical uncertainties on the flavour tagging calibration parameters ($p_{0,1}^{\text{OS,SS}\pi}$ and $\Delta p_{0,1}^{\text{OS,SS}\pi}$) are taken into account using Gaussian constraints (cf. Sec. 5.7.1). The influence of the systematic uncertainties are investigated by a ToyMC study.

First, the eight parameters are varied up and down by one systematic uncertainty and the effect on the effective dilution is studied. This reduces to 16 combinations if varying p_i^j and Δp_i^j only in the same direction. For each combination 750 iterations are performed and the dilution is calculated. The largest deviation is found when all p_0^j parameters are varied up and all p_1^j parameters are varied down. As the dilution and the *CP* parameters are part of a product in the PDF the relative change in dilution of 1.5 % is already an estimate of the systematic uncertainty.

A ToyMC study with 1000 iterations is performed using values for the *CP* parameters drawn from a Gaussian distribution where the central value is shifted according to the result of the preparatory study and the statistical uncertainty is used as width while including all correlations of the calibration parameters (cf. Sec. 4.3.2 and Tab. 4.5). The nominal model is used in the subsequent fit. As depicted in Fig. A.3 a significant bias is observed. The offsets of the residual

distributions

$$\delta_{S_{J/\psi K^0_S}} = 0.0062 \text{ and } \delta_{C_{J/\psi K^0_S}} = 0.0024 \tag{5.53}$$

are used as an estimate of the systematic uncertainties.

Decay time resolution

In the calibration of the decay time estimate a linear function is used. In a ToyMC study the influence of a different parametrisation of the calibration model is investigated. Based on the results given in Sec. 5.5.1 a parabolic function with non-zero (zero) offset is used in the DD (LL) subsample to generate data, that is then fitted using the nominal calibration model. The parameter values used in the generation are given in Tab. 5.26. In a study with 1000 iterations no significant bias is found as can been seen in the pull and residual distributions provided in Fig. A.4.

Table 5.26 – Fit parameters of the parabolic decay time resolution calibration function for DD and LL candidates. No offset parameter is used in case of the LL model, thus the correspondent entries are marked with a dash.

Parameter		DD	LL
a_1	(ps^{-1})	-1.7 ± 1.3	-4.3 ± 0.7
b_1		1.040 ± 0.014	1.33 ± 0.07
c_1	(ps)	0.0044 ± 0.0027	—
a_2	(ps^{-1})	-1.5 ± 3.4	-2.5 ± 1.0
b_2		1.5 ± 0.4	2.15 ± 0.27
c_2	(ps)	0.016 ± 0.008	—

An offset to the central values of the three Gaussian PDFs is used in the parametrisation of the decay time resolution model (cf. Eq. (5.5)). Due to technical limitations in the implementation of the cubic spline PDFs the value of this offset μ_t has to be set to zero in the nominal fit although non-zero values are found in the determination of the resolution model. The influence of ignoring the non-zero values is tested in a ToyMC study with 250 iterations, where the data is generated using the offset's value originally determined, while fitting with the nominal fit model. No significant bias is observed. Plots of the pull and residual distributions are shown in Fig. A.5.

The fraction of wrongly associated PVs is assumed to be independent of the decay time resolution estimate σ_t. This ignores an increase in the fraction f_{PV} as a function of the decay time error. The influence of this simplification is tested in a ToyMC study with 1000 iterations, where the fraction varies following a parabolic function with offset fixed to zero in the generation, while f_{PV} is set as in the

nominal model in the subsequent fit. As depicted in Fig. A.6 a significant bias is present for the parameter $S_{J/\psi K^0_S}$ as well as for $C_{J/\psi K^0_S}$. Thus, systematic uncertainties of

$$\delta_{S_{J/\psi K^0_S}} = 0.0021 \text{ and } \delta_{C_{J/\psi K^0_S}} = 0.0011 \tag{5.54}$$

are assigned.

Decay time acceptance

The low decay time acceptance's influence on the *CP* parameters is studied using a modified acceptance shape. In the generation histograms of the time-dependent ratios ε_{AU} and ε_{EB} (cf. Sec. 5.5.2) are employed that are determined on the signal MC sample using the same methodology as used for the nominal model. In 250 iterations the generated data are fitted using the nominal (12 and OS) fit model, as no influence from the tagging decision and the year of data taking is expected. The ToyMC study shows no significant bias. Pull and residual distributions can be found in Fig. A.7.

The upper decay time acceptance is parametrised in the nominal fit using a linear scale model. As outlined in Sec. 5.5.2 higher order effects are studied using a quadratic correction function but are not considered in the fit later on. To estimate the impact of a deviating correction function on the *CP* parameters a ToyMC study with 1000 iterations is performed. As the upper decay time acceptance is not expected to dependent on the trigger category nor the tagging category, data are only generated using the (AU and OS) fit model. The generation is performed using the parametrisation given in Eq. (5.10) with parameters fixed to the values shown in Tab. 5.21. In the fit the nominal model with a linear correction function is used. No deviation of a standard normal distribution is found for the $S_{J/\psi K^0_S}$ pull distribution. A small bias on $C_{J/\psi K^0_S}$ is visible in the pull distribution, therefore a systematic uncertainty of

$$\delta_{C_{J/\psi K^0_S}} = 0.0012 \tag{5.55}$$

is assigned. Pull and residual distributions can be found in Fig. A.8.

Production asymmetry, z-scale, Δm_d, and $\Delta\Gamma_d$

The z-scale alignment of the LHCb detector is known up to a relative uncertainty of $\sigma_{z\text{-scale}} = 0.022\,\%$. To study how this affects the measurement of the *CP* parameters, data are generated using an offset of $\mu_t = \sigma_{z\text{-scale}} t$ in the decay time resolution model. In the fit the offset is set to zero as in the nominal fit model. In a ToyMC study with 1000 iterations a small bias is observed for $S_{J/\psi K^0_S}$ as well as for $C_{J/\psi K^0_S}$ and systematic uncertainties of

$$\delta_{S_{J/\psi K^0_S}} = 0.0012 \text{ and } \delta_{C_{J/\psi K^0_S}} = 0.0023 \tag{5.56}$$

are assigned. Pull and residual distributions can be found in Fig. A.9.

The influence of the production asymmetry on the measurement of $S_{J/\psi K^0_S}$ and $C_{J/\psi K^0_S}$ is investigated in a ToyMC study. In 1000 iterations, samples are produced with an enlarged production asymmetry and subsequently fitted with the nominal fit model. The production asymmetry is varied by one systematic uncertainty: $A_P^{11} = -0.0122$ while ΔA_P is not shifted, as any systematic effect from the difference of the production asymmetry between 11 and 12 is already covered. No systematic shift is observed. The pull and residual distributions are depicted in Fig. A.10.

The B^0 decay width difference's impact on the CP measurement is examined in a ToyMC study with 1000 iterations. The data is generated using $\Delta\Gamma_d = 0.007\,\mathrm{ps}^{-1}$ as an upper approximation based on the current world average of the ratio between the decay width difference and the absolute decay width $\Delta\Gamma_d/\Gamma_d = 0.001 \pm 0.010$ [14]. The fit then neglects the non-zero $\Delta\Gamma_d$ value as in the nominal model. A significant bias is observed in the pull distribution of $S_{J/\psi K^0_S}$, thus a systematic uncertainty of

$$\delta_{S_{J/\psi K^0_S}} = 0.0047 \tag{5.57}$$

is assigned as an estimate to cover for this effect. The pull and residual distributions for $S_{J/\psi K^0_S}$ and $C_{J/\psi K^0_S}$ are depicted in Fig. A.11.

The B^0 mass difference Δm_d is taken as a constrained external input to the fit model. The influence of the systematic uncertainty on Δm_d is treated in a ToyMC study with 1000 iterations of generation and fit. In the generation the value of the mass difference is enlarged by the systematic uncertainty, i.e. $\Delta m_d = 0.512\,\hbar\,\mathrm{ps}^{-1}$, the nominal model is used in the fit. The pull distribution of $C_{J/\psi K^0_S}$ shows a significant deviation, therefore the offset of the residual distribution

$$\delta_{C_{J/\psi K^0_S}} = 0.0034 \tag{5.58}$$

is taken as an estimate of the systematic uncertainty. Fig. A.12 shows the pull and residual distributions for $S_{J/\psi K^0_S}$ and $C_{J/\psi K^0_S}$.

5.8.3 Summary of systematic effects

The systematic uncertainties are summarised in Tab. 5.27. The overall systematic uncertainty is calculated by summing the single uncertainties in quadrature. The relative systematic uncertainties compared to the central values of $S_{J/\psi K^0_S}$ and $C_{J/\psi K^0_S}$ are given in brackets. Here, $S_{J/\psi K^0_S} = 0.729$ and $C_{J/\psi K^0_S} = -0.033$ are set as reference values.

Table 5.27 – Systematic uncertainties $\delta_{S_{J/\psi K^0_S}}$ and $\delta_{C_{J/\psi K^0_S}}$ on $S_{J/\psi K^0_S}$ and $C_{J/\psi K^0_S}$. Entries marked with a dash represent studies where no significant effect is observed.

Origin	$\delta_{S_{J/\psi K^0_S}}$		$\delta_{C_{J/\psi K^0_S}}$	
Background tagging asymmetry	0.0179	(2.5%)	0.0015	(4.5%)
Tagging calibration	0.0062	(0.9%)	0.0024	(7.2%)
$\Delta\Gamma_d$	0.0047	(0.6%)	—	
Fraction of wrong PV component	0.0021	(0.3%)	0.0011	(3.3%)
z-scale	0.0012	(0.2%)	0.0023	(7.0%)
Δm_d	—		0.0034	(10.3%)
Upper decay time acceptance	—		0.0012	(3.6%)
Correlation between mass and decay time	—		—	
Decay time resolution calibration	—		—	
Decay time resolution offset	—		—	
Low decay time acceptance	—		—	
Production asymmetry	—		—	
Sum	0.020	(2.7%)	0.005	(15.2%)

6 Conclusion and outlook

During the first LHC run period from 2010 to 2012, the Large Hadron Collider beauty (LHCb) experiment showed an outstanding performance and high quality data was recorded. The discovery of the Higgs boson [29] endorses the theoretical framework and is a huge success for particle physics. Still, the necessity of Beyond Standard Model (BSM) physics is not deniable. Missing direct observations of BSM effects like heavy super-symmetric particles or a suitable dark matter candidate dash the hope of new findings at the TeV-scale. Run II of the LHC will be crucial for the future of the particle physics community and the design of next-generation experiments.

While direct searches for new heavy particles are constrained by the available collision energies, indirect searches are sensitive to BSM effects through higher order contributions, even with collision energies far below the threshold for direct production of heavy particles. The LHCb experiment was therefore designed to perform high precision tests of the Standard Model of Particle Physics (SM) in decays of B and D mesons and to identify possible deviations from the SM. Especially the measurement of CP violation in the decay of $B^0 \to J/\psi K^0_S$ acts as a prime example with small theoretical uncertainties, easy to reconstruct final states, and high event yields.

The measurement of the CP parameters $S_{J/\psi K^0_S}$ and $C_{J/\psi K^0_S}$ presented in this thesis is realised on a dataset corresponding to an integrated luminosity of $3.0\,\text{fb}^{-1}$ recorded by the LHCb experiment in proton-proton collisions at centre-of-mass energies of 7 and 8 TeV. The sample contains 41 500 reconstructed $B^0 \to J/\psi K^0_S$ candidates with a flavour tagging decision assigned by the same-side pion or the opposite-side tagging algorithm. Using an unbinned extended maximum likelihood fit, the CP parameters $S_{J/\psi K^0_S}$ and $C_{J/\psi K^0_S}$ are measured to be

$$\begin{aligned} S_{J/\psi K^0_S} &= \quad 0.731 \pm 0.035\,(\text{stat}) \pm 0.020\,(\text{syst})\,, \text{ and} \\ C_{J/\psi K^0_S} &= -0.038 \pm 0.032\,(\text{stat}) \pm 0.005\,(\text{syst})\,, \end{aligned}$$

with a statistical correlation coefficient of $\rho(S_{J/\psi K^0_S}, C_{J/\psi K^0_S}) = 0.483$. With the parameter $C_{J/\psi K^0_S}$ fixed to zero, the measurement yields

$$S_{J/\psi K^0_S} = \sin(2\beta) = 0.746 \pm 0.030\,(\text{stat})\,.$$

The measurement improves the previous LHCb result [28] by including a larger dataset, additional trigger lines, an optimised candidate selection and by incorporating the same-side pion tagger decisions. It is the most precise measurement of

CP violation at a hadron collider and is in excellent agreement with the current world average.

The obtained precision of the measurement outperforms expectations based on the result from the previous measurement, which predicts a sensitivity on $S_{J/\psi K^0_S}$ of 0.04, only considering the larger data sample while assuming all efficiencies to be unchanged. Implying the improved tagging performance into these predictions, still results in an expected sensitivity on $S_{J/\psi K^0_S}$ of 0.037, thus the choice of including additional trigger lines and optimising the selection proves itself as beneficial.

Including this measurement, the updated world average on $\sin(2\beta)$ [14] is

$$\sin(2\beta) = 0.691 \pm 0.017\,,$$

reducing the tension to the fit of all other Cabibbo-Kobayashi-Maskawa (CKM) matrix parameters slightly to $\Delta\chi^2 = 1.66$ [38]. Fig. 6.1 shows the (d, b) unitarity triangle in the $(\overline{\rho}, \overline{\eta})$-plane from a global fit incorporating all measured CKM parameters [38] except from the one reported here that is additionally shown to allow for a better comparison.

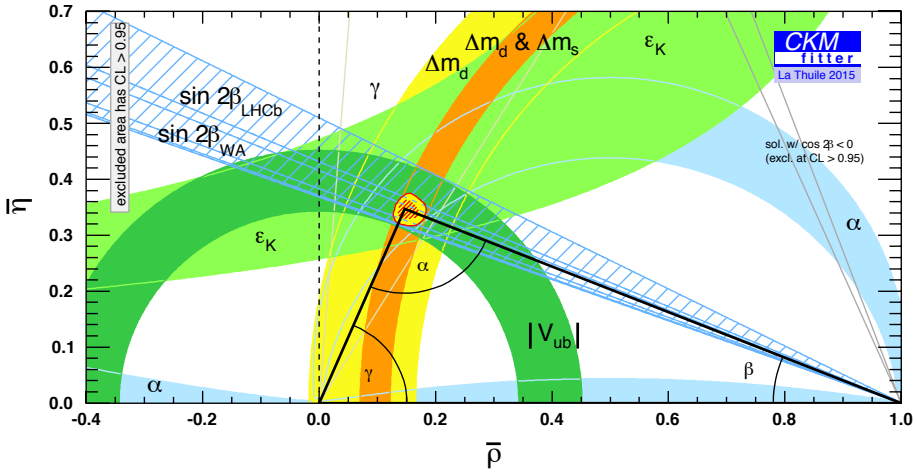

Figure 6.1 – Constraints on the (d, b) unitarity triangle in the $(\overline{\rho}, \overline{\eta})$-plane from a global fit incorporating all measured CKM parameters except the result presented in this thesis, which is shown separately as a comparison in light blue. Regions outside the coloured areas have $1 - p > 95.45\,\%$. The red hashed region of the global combination corresponds to 68 % CLs. [38]

During Run II of the LHC, starting this year at a centre-of-mass energy of 13 TeV, LHCb is expected to collect a large dataset corresponding to an integrated luminosity of around $5\,\text{fb}^{-1}$ until the next long shut-down scheduled in 2018. With an estimated sensitivity on $S_{J/\psi K^0_S}$ of 0.018 [105], this additional data will allow the LHCb collaboration to perform the world's best single measurement of $\sin(2\beta)$. As this sensitivity falls below the current systematic uncertainty, a better

understanding of the background tagging asymmetry and a reduction of the flavour tagging uncertainties are necessary. With more data being available, a reassessment of the magnitude of the background tagging asymmetry is possible, leading either to a model to describe the effect inside the likelihood fit or a confirmation that no background asymmetry is present in data. The uncertainties on the flavour tagging parameters will shrink with more data available in the calibration and cross-check channels, as well as a better understanding of the flavour tagging algorithms and new developments in the calibration procedure. Furthermore, the systematic uncertainty due to neglecting the decay width difference $\Delta\Gamma_d$ will become closer to the statistical uncertainty in Run II, such that the handling of $\Delta\Gamma_d$ has to be revisited [105].

To further improve the sensitivity on the measurement of $\sin(2\beta)$, additional decay modes will be explored. Based on the Run I dataset, the decay of the B^0 into the $J/\psi(\to e^+e^-)K^0_S$ final state is expected to contribute with a sensitivity of 0.1 [106]. Beyond that, higher charmonium resonances as in $B^0 \to \psi(2S)K^0_S$ will add sensitivity to the combined result. Preparatory studies have shown an expected sensitivity on $\sin(2\beta)$ of 0.09 in the combination of the $\psi(2S) \to J/\psi\pi\pi$ and the $\psi(2S) \to \mu^+\mu^-$ final states for Run I [107].

The biggest LHCb competitor will be the Belle II experiment. The collaboration plans to start data taking in 2018 with an expected instantaneous luminosity 50 times larger than its predecessor experiment Belle. With an assumption of 100 days of efficient data taking per year, an integrated luminosity of $8\,\text{ab}^{-1}$ will be recorded per year. If these expectations hold true, Belle II will be able to reduce the total uncertainty on $\sin(2\beta)$ to 0.010 on a short time scale with the uncertainty mainly being dominated by irreducible systematic uncertainties [108].

During the second long shut down of the LHC in 2018 the LHCb detector will be upgraded to cope with a higher instantaneous luminosity of $L = 2 \cdot 10^{33}\,\text{cm}^{-2}\,\text{s}^{-1}$ and an enhanced $b\bar{b}$-pair production rate of 10^6 per second [109]. The upgrade involves a new hybrid pixel-sensor vertex locator [110], new tracking stations based on silicon micro-strip and scintillating-fibre technology [111], enhancements of the ring-imaging Cherenkov detector systems, the calorimeters and the muon system [112], and a new software trigger concept capable of reading out the full detector at the nominal bunch crossing frequency of 40 MHz [113]. This will result in a large dataset corresponding to an expected integrated luminosity of $50\,\text{fb}^{-1}$ with the upgraded detector. Assuming unchanged data taking efficiencies and similar performance of the trigger, stripping, and flavour tagging, pseudo-experiment studies estimate a sensitivity on $\sin(2\beta)$ of around 0.007 [105] in the decay $B^0 \to J/\psi K^0_S$.

The presented measurement is competitive with the results from the B factories and LHCb will be able to provide the world's most accurate measurement of $\sin(2\beta)$ with more data available by the end of Run II. For measurements beyond that, contributions from higher-order loop processes will become important, such that the measurement of CP violation in $B^0_s \to J/\psi K^0_S$ will be an essential ingredient to further improve the precision on $\sin(2\beta)$ and to test the SM expectations.

A Supplementary material to the measurement of sin(2β)

A.1 Decay time resolution and acceptance

A.1.1 Resolution

For the DD candidates Tab. A.1 shows the fit results of the χ^2-fit of the decay time error estimate calibration parameters for a linear function and a parabolic function with offset parameter, while Tab. A.2 includes fit results for the LL subsample where a linear function and a parabolic function without offset parameter are fitted.

Table A.1 – Fit parameters of the decay time resolution calibration functions for the DD subsample.

Model	Parameter		narrow width ($i = 1$)	wider width ($i = 2$)
linear	b_i		0.89 ± 0.10	1.34 ± 0.29
	c_i	(ps)	0.008 ± 0.004	0.018 ± 0.011
parabolic	a_i	(ps^{-1})	-3 ± 6	-1 ± 17
	b_i		1.2 ± 0.5	1.4 ± 1.4
	c_i	(ps)	0.003 ± 0.010	0.016 ± 0.028

Table A.2 – Fit parameters of the decay time resolution calibration functions for the LL subsample.

Model	Parameter		narrow width ($i = 1$)	wider width ($i = 2$)
linear	b_i		1.10 ± 0.07	1.81 ± 0.26
	c_i	(ps)	0.0034 ± 0.0019	0.009 ± 0.008
parabolic	a_i	(ps^{-1})	-4.7 ± 2.1	-6 ± 8
	b_i		1.36 ± 0.07	2.27 ± 0.26

A.2 Measurement of *CP* violation

A.2.1 Tables of fixed parameters

Table A.3 – Fixed mass parameters.

Parameter	Fixed Value
$\alpha_{1,m}^{\mathrm{DD}}$	2.28
$\alpha_{1,m}^{\mathrm{LL}}$	2.1
$\alpha_{2,m}^{\mathrm{DD}}$	2.08
$\alpha_{2,m}^{\mathrm{LL}}$	2.43
$\lambda_{m}^{\mathrm{DD}}$	-2.8
$\lambda_{m}^{\mathrm{LL}}$	-3.6
ζ_{m}^{DD}	0.0
ζ_{m}^{LL}	0.0
n_{1}^{DD}	3.18
n_{1}^{LL}	3.2
n_{2}^{DD}	6.8
n_{2}^{LL}	4.1

Table A.4 – Fixed decay time error parameters of the (left) signal and (right) background parametrisation.

Parameter		Fixed Value
$f_{\sigma_t}^{\mathrm{DD,OS,AU}}$		0.069461
$f_{\sigma_t}^{\mathrm{DD,OS,EB}}$		0.09431
$f_{\sigma_t}^{\mathrm{DD,SS}}$		0.088404
$f_{\sigma_t}^{\mathrm{LL,OS}}$		0.55165
$M_1^{\mathrm{DD,OS,AU}}$	(ps)	0.037506
$M_1^{\mathrm{DD,OS,EB}}$	(ps)	0.034481
$M_1^{\mathrm{DD,SS}}$	(ps)	0.032577
$M_2^{\mathrm{DD,OS,AU}}$	(ps)	0.077666
$M_2^{\mathrm{DD,OS,EB}}$	(ps)	0.072158
$M_2^{\mathrm{DD,SS}}$	(ps)	0.059685
$M^{\mathrm{LL,OS}}$	(ps)	0.033253
$M^{\mathrm{LL,SS}}$	(ps)	0.029475
$k_1^{\mathrm{DD,OS,AU}}$		0.721
$k_1^{\mathrm{DD,OS,EB}}$		0.73243
$k_1^{\mathrm{DD,SS}}$		0.72851
$k_1^{\mathrm{LL,OS}}$		0.80445
$k_2^{\mathrm{DD,OS,AU}}$		0.73407
$k_2^{\mathrm{DD,OS,EB}}$		0.65444
$k_2^{\mathrm{DD,SS}}$		0.70283
$k_2^{\mathrm{LL,OS}}$		0.70335
$k^{\mathrm{LL,SS}}$		0.75457

Parameter		Fixed Value
$f_{\sigma_t}^{\mathrm{DD,!(OS,AU)}}$		0.11432
$f_{\sigma_t}^{\mathrm{DD,OS,AU}}$		0.29076
$f_{\sigma_t}^{\mathrm{LL,AU}}$		0.85159
$f_{\sigma_t}^{\mathrm{LL,EB}}$		0.93631
$M_1^{\mathrm{DD,!(OS,AU)}}$	(ps)	0.03674
$M_1^{\mathrm{DD,OS,AU}}$	(ps)	0.037739
$M_1^{\mathrm{LL,AU}}$	(ps)	0.042243
$M_1^{\mathrm{LL,EB}}$	(ps)	0.047283
$M_2^{\mathrm{DD,!(OS,AU)}}$	(ps)	0.072757
$M_2^{\mathrm{DD,OS,AU}}$	(ps)	0.064157
$M_2^{\mathrm{LL,AU}}$	(ps)	0.030178
$M_2^{\mathrm{LL,EB}}$	(ps)	0.029563
$k_1^{\mathrm{DD,!(OS,AU)}}$		0.73464
$k_1^{\mathrm{DD,OS,AU}}$		0.72987
$k_1^{\mathrm{LL,AU}}$		0.69218
$k_1^{\mathrm{LL,EB}}$		0.59111
$k_2^{\mathrm{DD,!(OS,AU)}}$		0.68463
$k_2^{\mathrm{DD,OS,AU}}$		0.67792
$k_2^{\mathrm{LL,AU}}$		0.77259
$k_2^{\mathrm{LL,EB}}$		0.78276

Table A.5 – Fixed OS mistag spline parameters for the (left) signal and (right) background parametrisation.

Parameter	Fixed Value
$u_{S,1}^{\mathrm{OS}}$	0.0
$u_{S,2}^{\mathrm{OS}}$	0.50758
$u_{S,3}^{\mathrm{OS}}$	3.0879
$u_{S,4}^{\mathrm{OS}}$	3.7690
$u_{S,5}^{\mathrm{OS}}$	12.776
$u_{S,6}^{\mathrm{OS}}$	9.2243
$u_{S,7}^{\mathrm{OS}}$	26.375
$u_{S,8}^{\mathrm{OS}}$	29.490
$u_{S,9}^{\mathrm{OS}}$	39.154
$u_{S,10}^{\mathrm{OS}}$	39.090
$u_{S,11}^{\mathrm{OS}}$	34.295

Parameter	Fixed Value
$u_{B,1}^{\mathrm{DD,OS}}$	0.0
$u_{B,2}^{\mathrm{DD,OS}}$	0.25646
$u_{B,3}^{\mathrm{DD,OS}}$	2.8381
$u_{B,4}^{\mathrm{DD,OS}}$	5.0101
$u_{B,5}^{\mathrm{DD,OS}}$	19.184
$u_{B,6}^{\mathrm{DD,OS}}$	12.047
$u_{B,7}^{\mathrm{DD,OS}}$	42.811
$u_{B,8}^{\mathrm{DD,OS}}$	53.376
$u_{B,9}^{\mathrm{DD,OS}}$	59.998
$u_{B,10}^{\mathrm{DD,OS}}$	67.425
$u_{B,11}^{\mathrm{DD,OS}}$	64.236
$u_{B,1}^{\mathrm{LL,OS}}$	0.0
$u_{B,2}^{\mathrm{LL,OS}}$	0.96109
$u_{B,3}^{\mathrm{LL,OS}}$	10.005
$u_{B,4}^{\mathrm{LL,OS}}$	13.055
$u_{B,5}^{\mathrm{LL,OS}}$	65.181
$u_{B,6}^{\mathrm{LL,OS}}$	33.077
$u_{B,7}^{\mathrm{LL,OS}}$	161.56
$u_{B,8}^{\mathrm{LL,OS}}$	163.82
$u_{B,9}^{\mathrm{LL,OS}}$	244.14
$u_{B,10}^{\mathrm{LL,OS}}$	238.57
$u_{B,11}^{\mathrm{LL,OS}}$	259.16

Table A.6 – Fixed SSπ mistag spline parameters for the (left) signal and (right) background parametrisation.

Parameter	Fixed Value
$u_{S,1}^{\mathrm{DD,SS}}$	0.0
$u_{S,2}^{\mathrm{DD,SS}}$	0.0
$u_{S,3}^{\mathrm{DD,SS}}$	0.0402
$u_{S,4}^{\mathrm{DD,SS}}$	0.2597
$u_{S,5}^{\mathrm{DD,SS}}$	0.4804
$u_{S,6}^{\mathrm{DD,SS}}$	0.6534
$u_{S,1}^{\mathrm{LL,SS}}$	0.0
$u_{S,2}^{\mathrm{LL,SS}}$	0.0
$u_{S,3}^{\mathrm{LL,SS}}$	0.013
$u_{S,4}^{\mathrm{LL,SS}}$	0.1183
$u_{S,5}^{\mathrm{LL,SS}}$	0.2695
$u_{S,6}^{\mathrm{LL,SS}}$	0.4455

Parameter	Fixed Value
$u_{B,1}^{\mathrm{DD,SS}}$	0.0
$u_{B,2}^{\mathrm{DD,SS}}$	0.0
$u_{B,3}^{\mathrm{DD,SS}}$	0.1498
$u_{B,4}^{\mathrm{DD,SS}}$	0.8688
$u_{B,5}^{\mathrm{DD,SS}}$	1.9698
$u_{B,6}^{\mathrm{DD,SS}}$	5.3155
$u_{B,1}^{\mathrm{LL,SS}}$	0.0
$u_{B,2}^{\mathrm{LL,SS}}$	0.0
$u_{B,3}^{\mathrm{LL,SS}}$	0.0022
$u_{B,4}^{\mathrm{LL,SS}}$	0.1173
$u_{B,5}^{\mathrm{LL,SS}}$	0.4442
$u_{B,6}^{\mathrm{LL,SS}}$	1.2042

Table A.7 – Fixed decay time resolution parameters

Parameter	Fixed Value
c_1^{DD}	0.0077
c_1^{LL}	0.0045
c_2^{DD}	0.019
c_2^{LL}	0.007
g_2^{DD}	0.251
g_2^{LL}	0.24
μ_t^{DD}	0.0
μ_t^{LL}	0.0
b_1^{DD}	0.88
b_1^{LL}	1.04
b_2^{DD}	1.33
b_2^{LL}	1.8
$\sigma_{\mathrm{PV}}^{\mathrm{DD}}$	1.6
$\sigma_{\mathrm{PV}}^{\mathrm{LL}}$	1.40
$f_{\mathrm{PV}}^{\mathrm{DD}}$	0.048
$f_{\mathrm{PV}}^{\mathrm{LL}}$	0.0488

Table A.8 – Fixed AU acceptance spline parameters for (left) AU and (right) EB candidates.

Parameter	Fixed Value
h_1^{AU}	0.93057
h_2^{AU}	0.93485
h_3^{AU}	0.96383
h_4^{AU}	0.96521
h_5^{AU}	0.99547
h_6^{AU}	0.97126
h_7^{AU}	0.96399
h_8^{AU}	0.9725
h_9^{AU}	0.98045
h_{10}^{AU}	0.97533

Parameter	Fixed Value
h_1^{EB}	0.1481
h_2^{EB}	0.27167
h_3^{EB}	0.29418
h_4^{EB}	0.35902
h_5^{EB}	0.40022
h_6^{EB}	0.4262
h_7^{EB}	0.44465
h_8^{EB}	0.47084
h_9^{EB}	0.49859
h_{10}^{EB}	0.52957

A.2.2 Fit results of subordinate parameters

Table A.9 – Results for the estimated signal and background candidate numbers from the nominal fit.

Sample				Parameter	Fitted Value
2011	DD	OS	AU	N_{Sig}	5134 ± 103
				N_{Bkg}	9352 ± 122
			EB	N_{Sig}	856 ± 39
				N_{Bkg}	1413 ± 46
		SS	AU	N_{Sig}	2028 ± 54
				N_{Bkg}	1251 ± 46
			EB	N_{Sig}	324 ± 20
				N_{Bkg}	153 ± 16
		BS	AU	N_{Sig}	941 ± 38
				N_{Bkg}	913 ± 38
			EB	N_{Sig}	138 ± 14
				N_{Bkg}	121 ± 13
	LL	OS	AU	N_{Sig}	2263 ± 54
				N_{Bkg}	1504 ± 47
			EB	N_{Sig}	333 ± 20
				N_{Bkg}	304 ± 19
		SS	AU	N_{Sig}	744 ± 29
				N_{Bkg}	119 ± 14
			EB	N_{Sig}	89 ± 9
				N_{Bkg}	13 ± 4
		BS	AU	N_{Sig}	321 ± 19
				N_{Bkg}	119 ± 13
			EB	N_{Sig}	46 ± 7
				N_{Bkg}	11 ± 4
2012	DD	OS	AU	N_{Sig}	10378 ± 156
				N_{Bkg}	20569 ± 185
			EB	N_{Sig}	2188 ± 66
				N_{Bkg}	4724 ± 83
		SS	AU	N_{Sig}	4246 ± 80
				N_{Bkg}	3199 ± 74
			EB	N_{Sig}	979 ± 35
				N_{Bkg}	468 ± 27
		BS	AU	N_{Sig}	1962 ± 57
				N_{Bkg}	2251 ± 59
			EB	N_{Sig}	403 ± 24
				N_{Bkg}	343 ± 23
	LL	OS	AU	N_{Sig}	4599 ± 79
				N_{Bkg}	3245 ± 70
			EB	N_{Sig}	971 ± 35
				N_{Bkg}	939 ± 35
		SS	AU	N_{Sig}	1550 ± 41
				N_{Bkg}	298 ± 22
			EB	N_{Sig}	281 ± 17
				N_{Bkg}	55 ± 9
		BS	AU	N_{Sig}	658 ± 27
				N_{Bkg}	177 ± 17
			EB	N_{Sig}	118 ± 11
				N_{Bkg}	34 ± 7

Table A.10 – Results for the mass parameters in the nominal fit

Parameter		Value
m^{DD}	(MeV/c^2)	5281.80 ± 0.28
σ_m^{DD}	(MeV/c^2)	9.9 ± 0.1
β_m^{DD}		-0.004 ± 0.004
α_m^{DD}	$((\mathrm{MeV}/c^2)^{-1})$	-0.00091 ± 0.00019
m^{LL}	(MeV/c^2)	5281.20 ± 0.30
σ_m^{LL}	(MeV/c^2)	8.33 ± 0.09
β_m^{LL}		-0.009 ± 0.005
α_m^{LL}	$((\mathrm{MeV}/c^2)^{-1})$	-0.0004 ± 0.0004

Table A.11 – Results for the background decay time parameters in the nominal fit

Parameter		Value
$f_{2,t}^{\mathrm{DD,OS}}$		0.34 ± 0.06
$f_{3,t}^{\mathrm{DD,OS}}$		0.049 ± 0.018
$\tau_1^{\mathrm{DD,OS}}$	(ps)	0.579 ± 0.028
$\tau_2^{\mathrm{DD,OS}}$	(ps)	1.41 ± 0.17
$\tau_3^{\mathrm{DD,OS}}$	(ps)	4.2 ± 0.7
$f_{2,t}^{\mathrm{DD,SS}}$		0.15 ± 0.06
$\tau_1^{\mathrm{DD,SS}}$	(ps)	0.703 ± 0.032
$\tau_2^{\mathrm{DD,SS}}$	(ps)	1.72 ± 0.23
$f_{2,t}^{\mathrm{LL}}$		0.48 ± 0.21
$f_{3,t}^{\mathrm{LL}}$		0.043 ± 0.027
τ_1^{LL}	(ps)	0.22 ± 0.04
τ_2^{LL}	(ps)	0.40 ± 0.07
τ_3^{LL}	(ps)	4.2 ± 0.5

A.3 Studies of systematic effects

Fit model

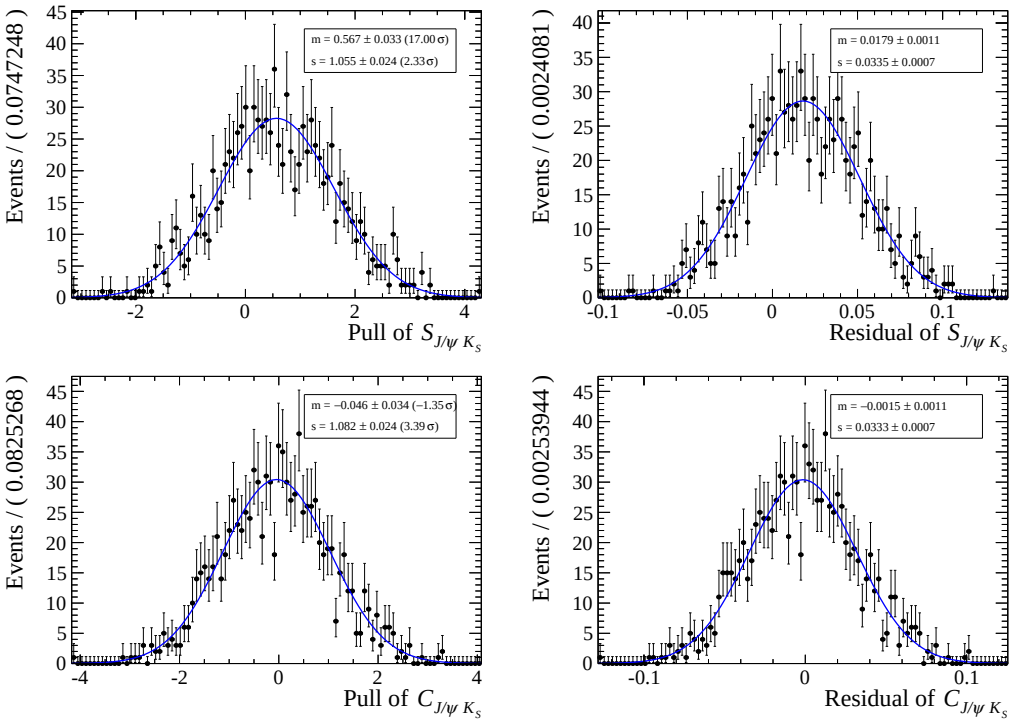

Figure A.1 – Shown are (left) pull and (right) residual distributions of the parameters (top) $S_{J/\psi K^0_S}$ and (bottom) $C_{J/\psi K^0_S}$ from a ToyMC study of the influence of an asymmetry in the background tagging estimates on the measurement of the CP parameters.

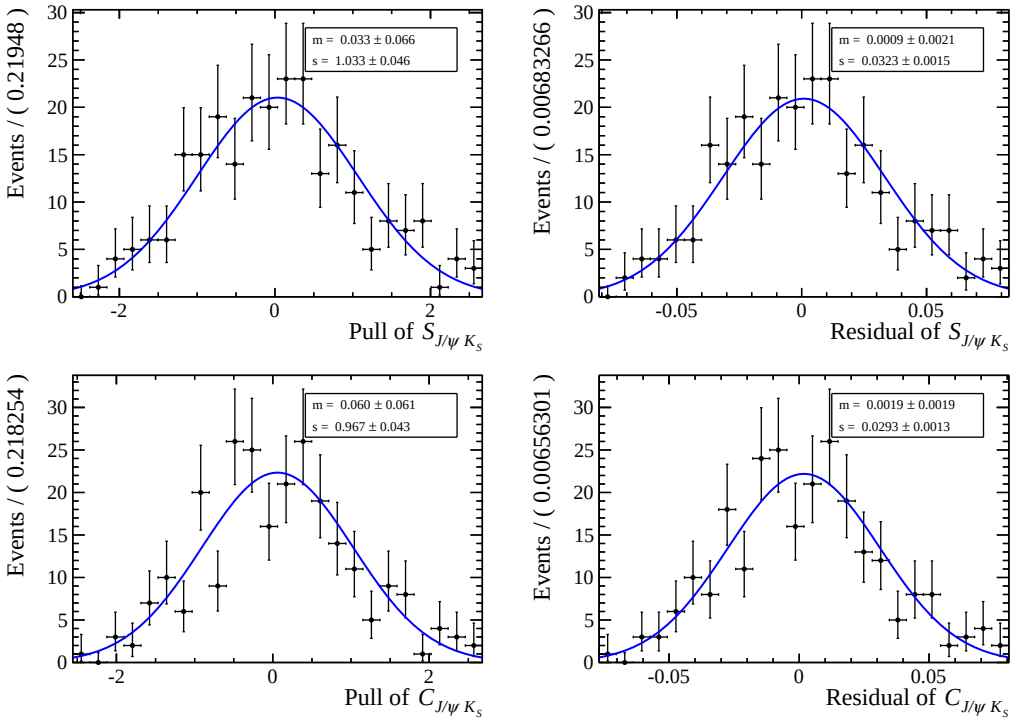

Figure A.2 – Shown are (left) pull and (right) residual distributions of the parameters (top) $S_{J/\psi K^0_S}$ and (bottom) $C_{J/\psi K^0_S}$ from a ToyMC study of the influence of a small mass and decay time correlation on the measurement of the CP parameters.

Flavour Tagging

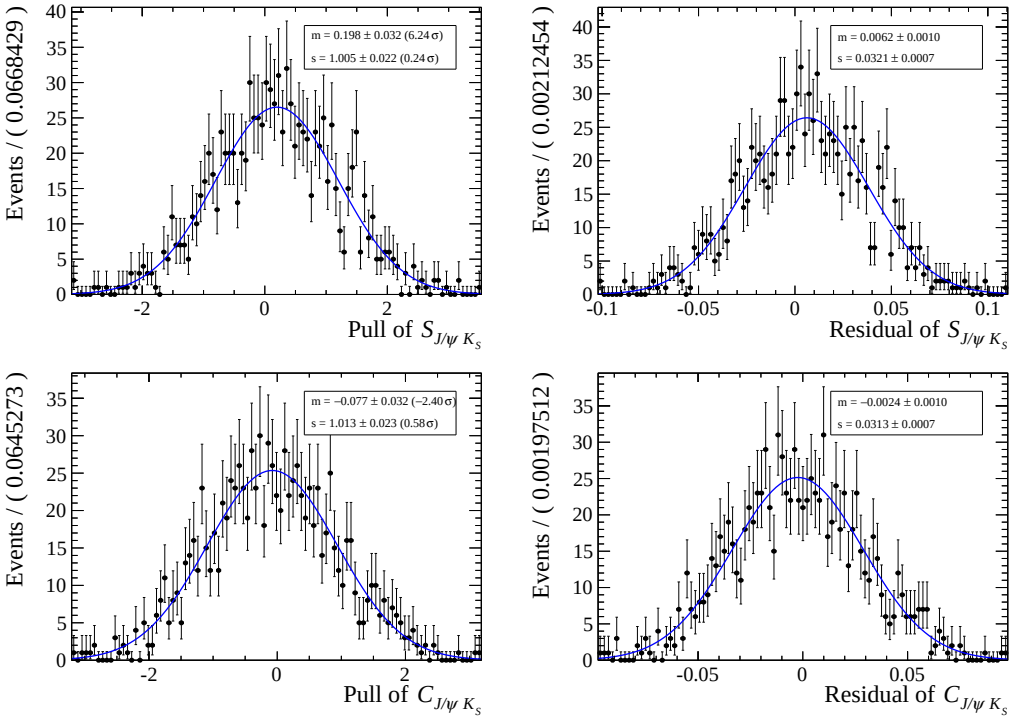

Figure A.3 – Shown are (left) pull and (right) residual distributions of the parameters (top) $S_{J/\psi K^0_S}$ and (bottom) $C_{J/\psi K^0_S}$ from a ToyMC study of the influence of the systematic uncertainties on the flavour tagging calibration parameters on the measurement of the CP parameters.

Decay time resolution

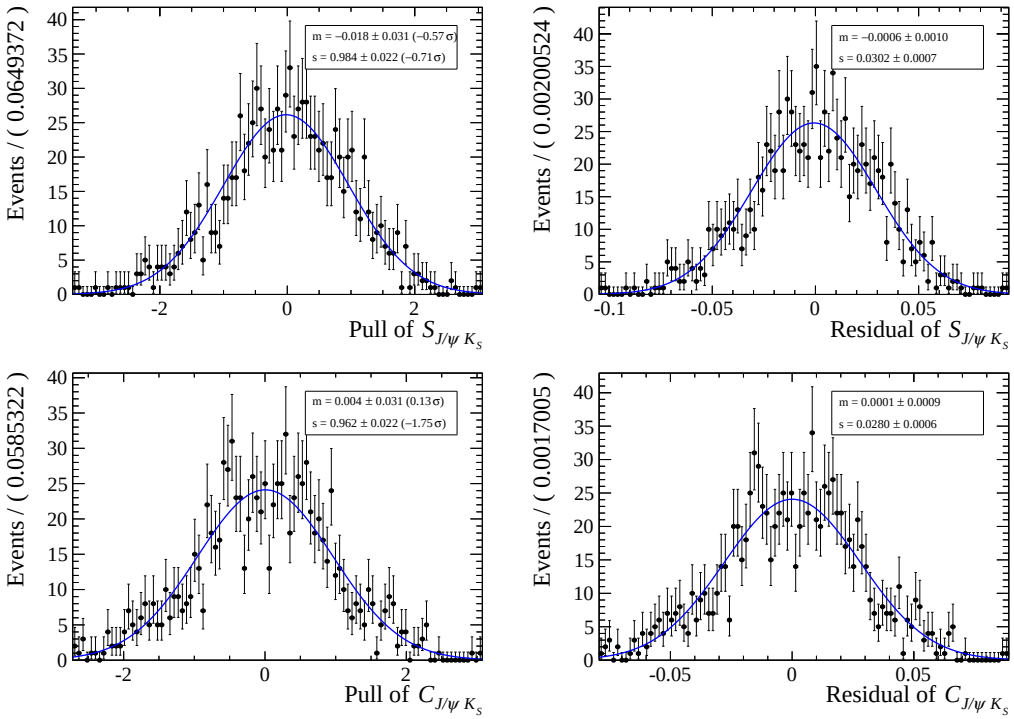

Figure A.4 – Shown are (left) pull and (right) residual distributions of the parameters (top) $S_{J/\psi K^0_S}$ and (bottom) $C_{J/\psi K^0_S}$ from a ToyMC study of the influence of the decay time resolution calibration model on the measurement of the *CP* parameters.

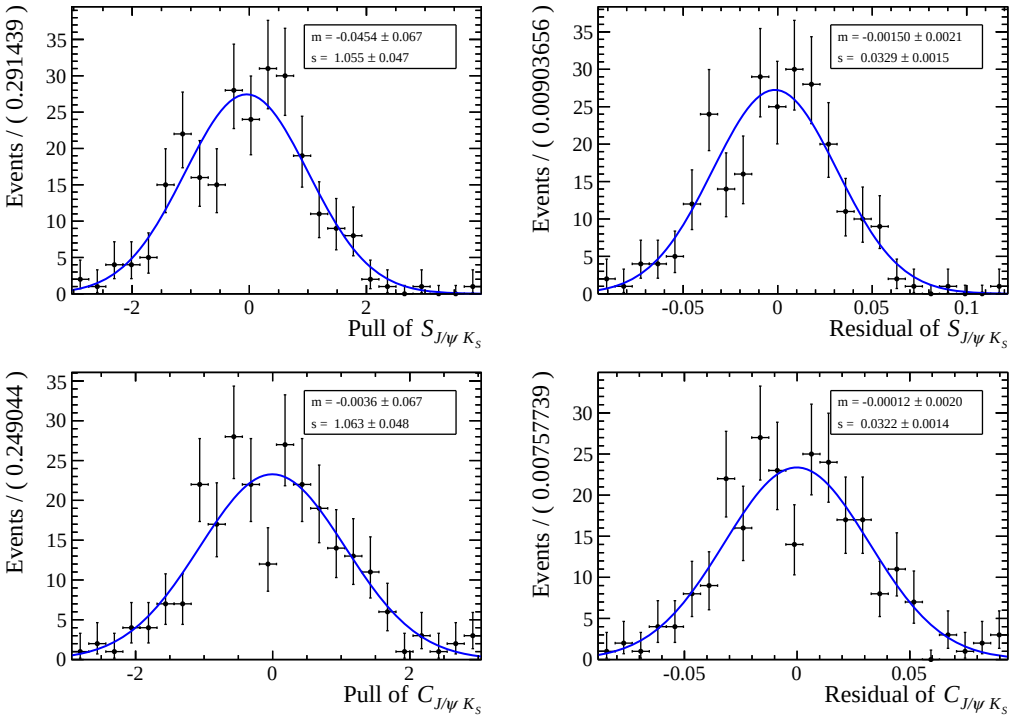

Figure A.5 – Shown are (left) pull and (right) residual distributions of the parameters (top) $S_{J/\psi K^0_S}$ and (bottom) $C_{J/\psi K^0_S}$ from a ToyMC study of the influence of neglecting a non-zero offset in the decay time resolution calibration model on the measurement of the CP parameters.

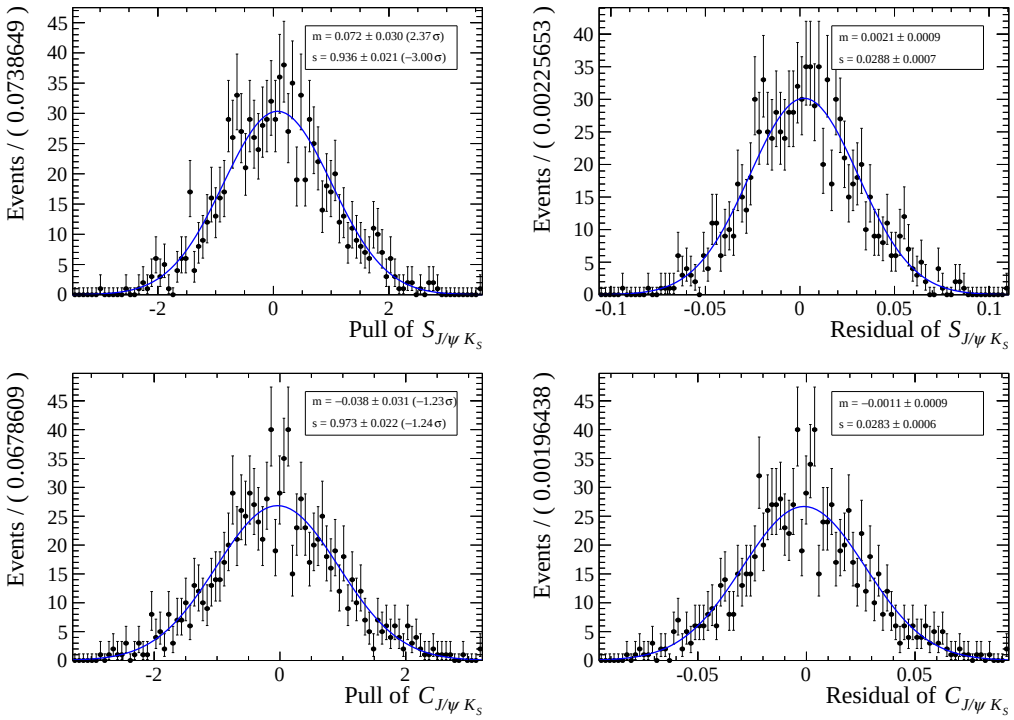

Figure A.6 – Shown are (left) pull and (right) residual distributions of the parameters (top) $S_{J/\psi K^0_S}$ and (bottom) $C_{J/\psi K^0_S}$ from a ToyMC study of the influence of the fraction of candidates with a wrong PV association on the measurement of the *CP* parameters.

Decay time acceptance

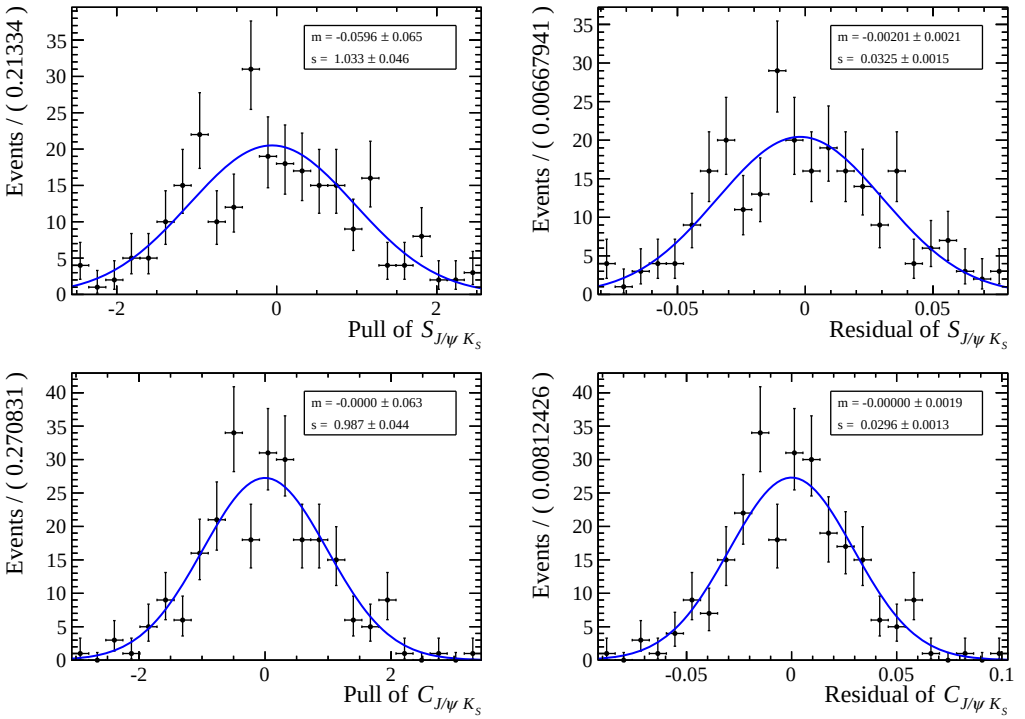

Figure A.7 – Shown are (left) pull and (right) residual distributions of the parameters (top) $S_{J/\psi K^0_S}$ and (bottom) $C_{J/\psi K^0_S}$ from a ToyMC study of the influence of the low decay time acceptance model on the measurement of the CP parameters.

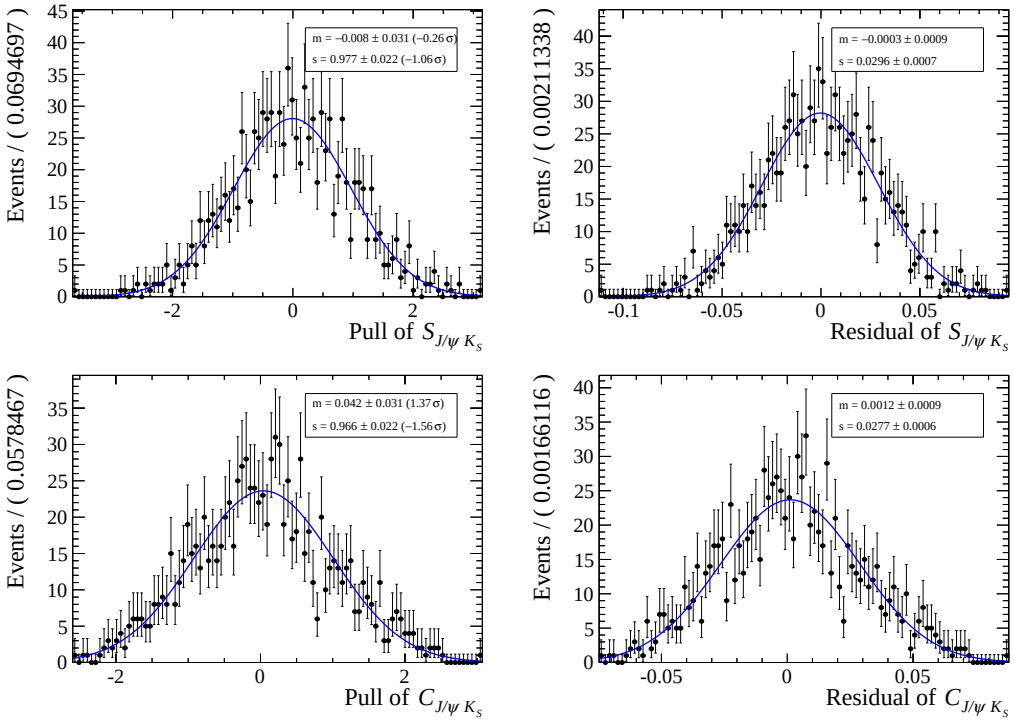

Figure A.8 – Shown are (left) pull and (right) residual distributions of the parameters (top) $S_{J/\psi K^0_S}$ and (bottom) $C_{J/\psi K^0_S}$ from a ToyMC study of the influence of the upper decay time acceptance correction function on the measurement of the CP parameters.

Production asymmetry, z-scale, Δm_d, and $\Delta\Gamma_d$

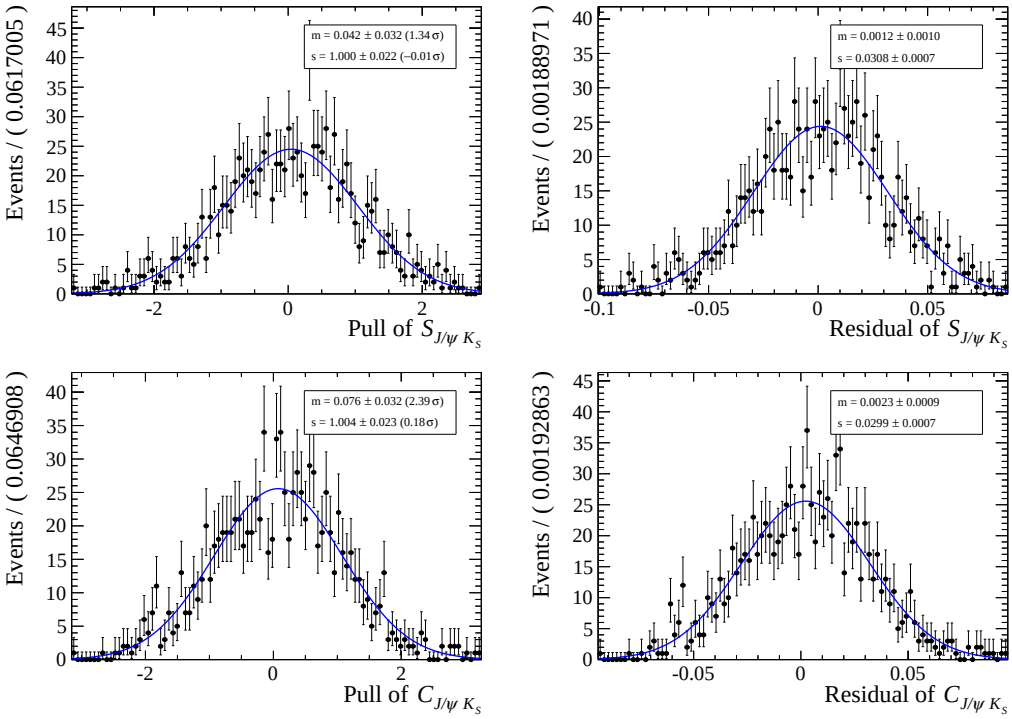

Figure A.9 – Shown are (left) pull and (right) residual distributions of the parameters (top) $S_{J/\psi K^0_S}$ and (bottom) $C_{J/\psi K^0_S}$ from a ToyMC study of the influence of the relative z-scale uncertainty on the measurement of the CP parameters.

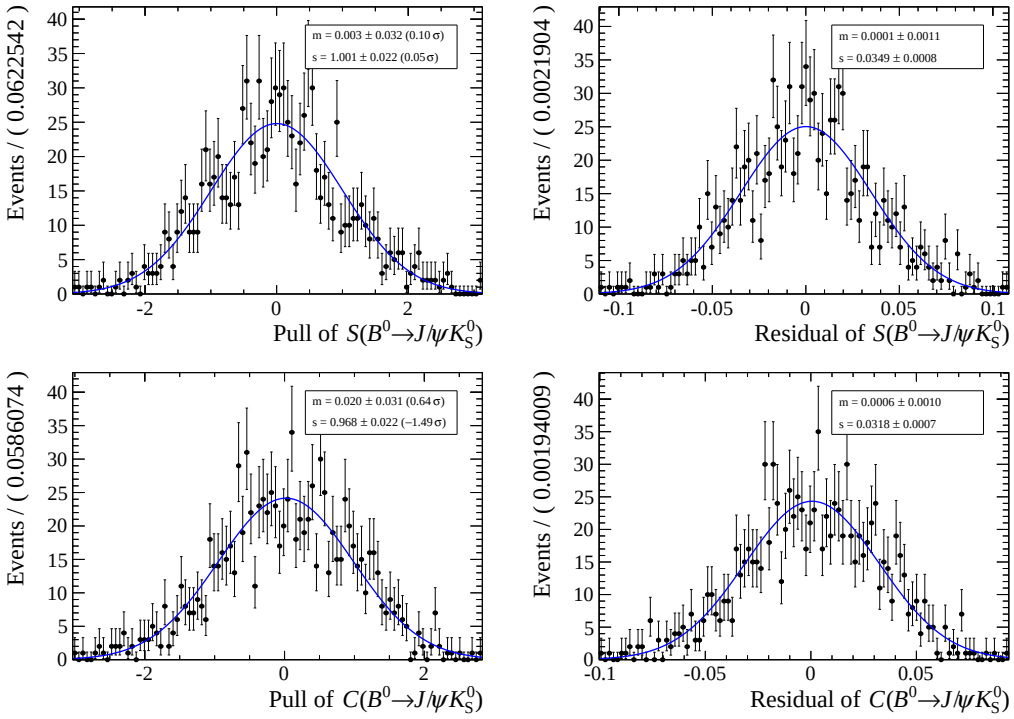

Figure A.10 – Shown are (left) pull and (right) residual distributions of the parameters (top) $S_{J/\psi K^0_S}$ and (bottom) $C_{J/\psi K^0_S}$ from a ToyMC study of the influence of an enlarged production asymmetry A_P^{11} on the measurement of the CP parameters.

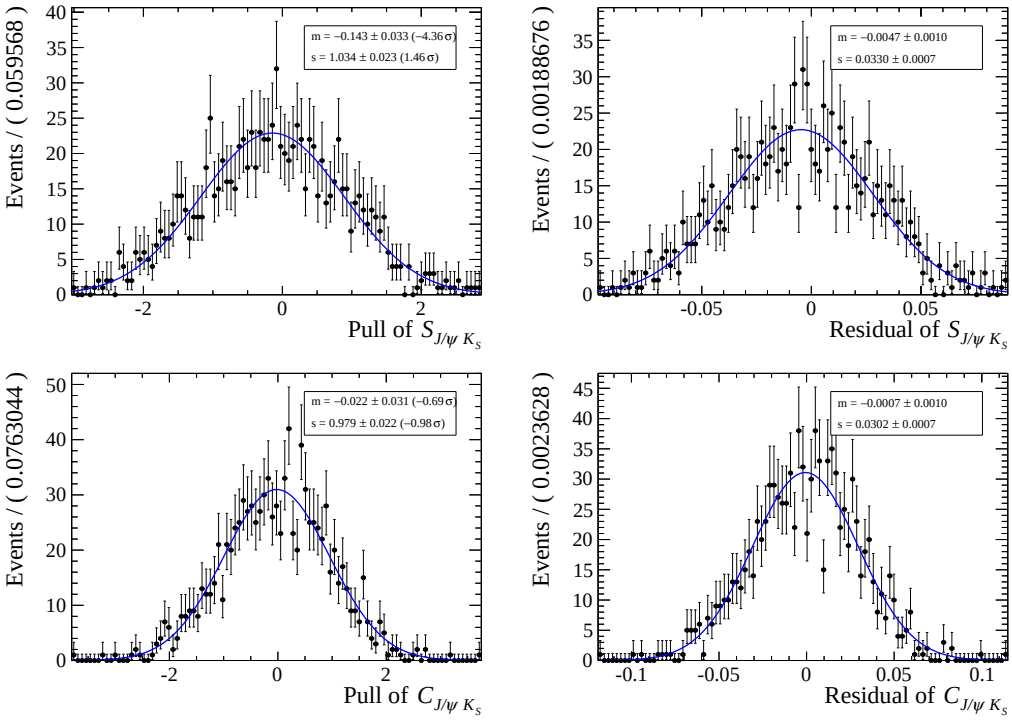

Figure A.11 – Shown are (left) pull and (right) residual distributions of the parameters (top) $S_{J/\psi K^0_S}$ and (bottom) $C_{J/\psi K^0_S}$ from a ToyMC study of the influence of a non-zero decay width difference $\Delta\Gamma_d$ on the measurement of the CP parameters.

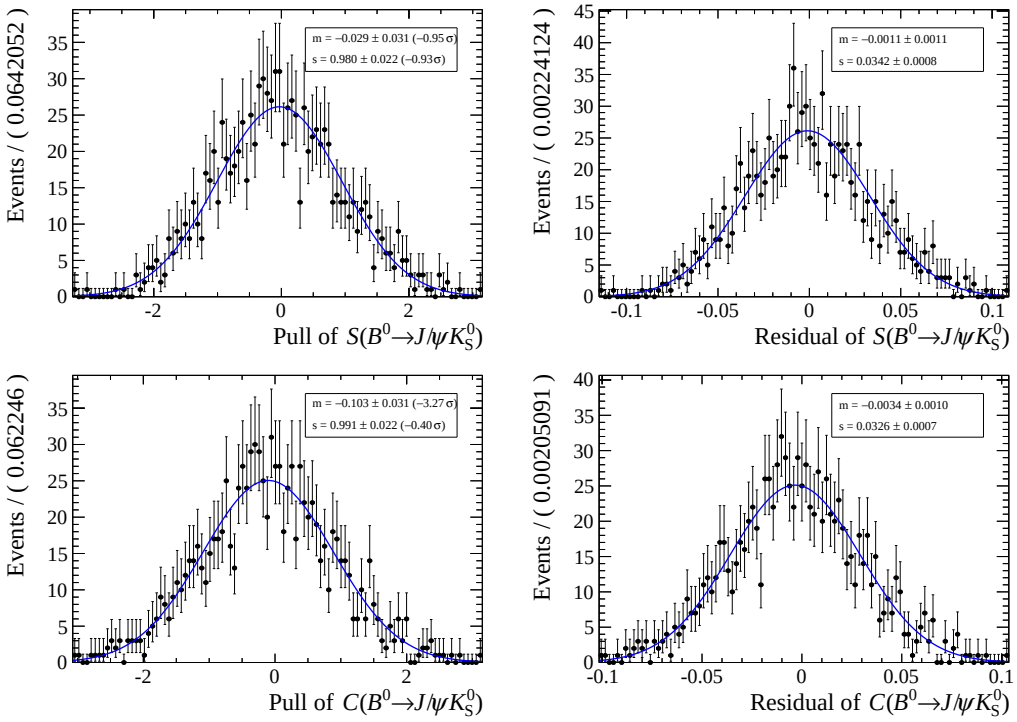

Figure A.12 – Shown are (left) pull and (right) residual distributions of the parameters (top) $S_{J/\psi K^0_S}$ and (bottom) $C_{J/\psi K^0_S}$ from a ToyMC study of the influence of an enlarged mass difference Δm_d on the measurement of the CP parameters.

Bibliography

[1] A. Sakharov, *Violation of CP Invariance, C Asymmetry, and Baryon Asymmetry of the Universe*, Pisma Zh. Eksp. Teor. Fiz. **5** (1967) 32–35, DOI: 10.1070/PU1991v034n05ABEH002497.

[2] G. 't Hooft, *Symmetry Breaking Through Bell-Jackiw Anomalies*, Phys. Rev. Lett. **37** (1976) 8–11, DOI: 10.1103/PhysRevLett.37.8.

[3] V. A. Rubakov and M. E. Shaposhnikov, *Electroweak baryon number non-conservation in the early universe and in high-energy collisions*, Usp. Fiz. Nauk **166** (1996), [Phys. Usp.39,461(1996)] 493–537, DOI: 10.1070/PU1996v039n05ABEH000145, arXiv:hep-ph/9603208 [hep-ph].

[4] G. Lüders, *On the equivalence of invariance under time reversal and under particle-antiparticle conjugation for relativistic field theories*, Det. Kong. Danske Videnskabernes Selskab Matematiske-fysiske Meddelelser **28**.5 (1954); W. Pauli and L. F. Curtiss, *Niels Bohr and the Development of Physics*, **24**, 1956 292, DOI: 10.1119/1.1934212.

[5] T. Lee and C.-N. Yang, *Question of Parity Conservation in Weak Interactions*, Phys. Rev. **104** (1956) 254–258, DOI: 10.1103/PhysRev.104.254.

[6] C. Wu *et al.*, *Experimental Test of Parity Conservation in Beta Decay*, Phys. Rev. **105** (1957) 1413–1414, DOI: 10.1103/PhysRev.105.1413.

[7] J. Christenson *et al.*, *Evidence for the* 2π *Decay of the* K_2^0 *Meson*, Phys. Rev. Lett. **13** (1964) 138–140, DOI: 10.1103/PhysRevLett.13.138.

[8] M. Kobayashi and T. Maskawa, *CP Violation in the Renormalizable Theory of Weak Interaction*, Prog. Theor. Phys. **49** (1973) 652–657, DOI: 10.1143/PTP.49.652.

[9] S. W. Herb *et al.*, *Observation of a Dimuon Resonance at 9.5 GeV in 400 GeV Proton-Nucleus Collisions*, Phys. Rev. Lett. **39** (1977) 252–255, DOI: 10.1103/PhysRevLett.39.252.

[10] A. Bevan *et al.*, *The Physics of the B Factories*, Eur. Phys. J. **C74**.11 (2014) 3026, DOI: 10.1140/epjc/s10052-014-3026-9, arXiv:1406.6311 [hep-ex].

[11] B. Aubert *et al.*, *Observation of CP violation in the* B^0 *meson system*, Phys. Rev. Lett. **87** (2001) 091801, DOI: 10.1103/PhysRevLett.87.091801, arXiv:hep-ex/0107013 [hep-ex].

[12] K. Abe *et al.*, *Observation of large CP violation in the neutral B meson system*, Phys. Rev. Lett. **87** (2001) 091802, DOI: 10.1103/PhysRevLett.87.091802, arXiv:hep-ex/0107061 [hep-ex].

[13] R. Aaij *et al.*, *Measurement of CP violation in $B^0 \to J/\psi K^0_S$ decays*, Phys. Rev. Lett. **115** (2015) 031601, DOI: 10.1103/PhysRevLett.115.031601, arXiv:1503.07089 [hep-ex].

[14] Y. Amhis *et al.*, *Averages of b-hadron, c-hadron, and τ-lepton properties as of summer 2014* (2014), arXiv:1412.7515 [hep-ex], updated results and plots available at: http://www.slac.stanford.edu/xorg/hfag/.

[15] J. Charles *et al.*, *Current status of the Standard Model CKM fit and constraints on $\Delta F = 2$ New Physics*, Phys. Rev. **D91**.7 (2015) 073007, DOI: 10.1103/PhysRevD.91.073007, arXiv:1501.05013 [hep-ph].

[16] R. Aaij *et al.*, *Measurement of the time-dependent CP asymmetries in $B^0_s \to J/\psi K^0_S$*, JHEP **2015**.6, 131 (2015), DOI: 10.1007/JHEP06(2015)131, arXiv:1503.07055 [hep-ex].

[17] R. Aaij *et al.*, *Measurement of indirect CP asymmetries in $D^0 \to K^-K^+$ and $D^0 \to \pi^-\pi^+$ decays using semileptonic B decays*, JHEP **1504** (2015) 043, DOI: 10.1007/JHEP04(2015)043, arXiv:1501.06777 [hep-ex].

[18] R. Aaij *et al.*, *Measurement of the CKM angle γ using $B^\pm \to DK^\pm$ with $D \to K^0_S\pi^+\pi^-, K^0_S K^+K^-$ decays*, JHEP **1410** (2014) 97, DOI: 10.1007/JHEP10(2014)097, arXiv:1408.2748 [hep-ex].

[19] R. Aaij *et al.*, *Measurement of CP asymmetry in $B^0_s \to D^\mp_s K^\pm$ decays*, JHEP **1411** (2014) 060, DOI: 10.1007/JHEP11(2014)060, arXiv:1407.6127 [hep-ex].

[20] R. Aaij *et al.*, *Measurement of the CP-violating phase ϕ_s in $\overline{B}^0_s \to J/\psi\pi^+\pi^-$ decays*, Phys. Lett. **B736** (2014) 186, DOI: 10.1016/j.physletb.2014.06.079, arXiv:1405.4140 [hep-ex].

[21] R. Aaij *et al.*, *Precision measurement of CP violation in $B^0_s \to J/\psi K^+K^-$ decays*, Phys. Rev. Lett. **114**.4 (2015) 041801, DOI: 10.1103/PhysRevLett.114.041801, arXiv:1411.3104 [hep-ex].

[22] R. Aaij *et al.*, *Measurement of CP violation in $B^0_s \to \phi\phi$ decays*, Phys. Rev. **D90**.5 (2014) 052011, DOI: 10.1103/PhysRevD.90.052011, arXiv:1407.2222 [hep-ex].

[23] V. Khachatryan *et al.*, *Observation of the rare $B^0_s \to \mu^+\mu^-$ decay from the combined analysis of CMS and LHCb data*, Nature **522** (2015) 68–72, DOI: 10.1038/nature14474, arXiv:1411.4413 [hep-ex].

[24] R. Aaij *et al.*, *Test of lepton universality using $B^+ \to K^+\ell^+\ell^-$ decays*, Phys. Rev. Lett. **113** (2014) 151601, DOI: 10.1103/PhysRevLett.113.151601, arXiv:1406.6482 [hep-ex].

[25] R. Aaij *et al.*, *Measurement of the ratio of branching fractions $\mathcal{B}(\overline{B}^0 \to D^{*+}\tau^-\overline{\nu}_\tau))/\mathcal{B}(\overline{B}^0 \to D^{*+}\mu^-\overline{\nu}_\mu)$* (2015), arXiv:1506.08614 [hep-ex].

[26] R. Aaij *et al.*, *Observation of two new Ξ_b^- baryon resonances*, Phys. Rev. Lett. **114** (2015) 062004, DOI: 10.1103/PhysRevLett.114.062004, arXiv:1411.4849 [hep-ex].

[27] R. Aaij *et al.*, *Observation of $J/\psi p$ resonances consistent with pentaquark states in $\Lambda_b^0 \to J/\psi K^- p$ decays*, Phys. Rev. Lett. **115** (2015) 072001, DOI: 10.1103/PhysRevLett.115.072001, arXiv:1507.03414 [hep-ex].

[28] R. Aaij *et al.*, *Measurement of the time-dependent CP asymmetry in $B^0 \to J/\psi K_S^0$ decays*, Phys. Lett. **B721** (2013) 24–31, DOI: 10.1016/j.physletb.2013.02.054, arXiv:1211.6093 [hep-ex].

[29] G. Aad *et al.*, *Combined Measurement of the Higgs Boson Mass in pp Collisions at $\sqrt{s} = 7$ and 8 TeV with the ATLAS and CMS Experiments*, Phys. Rev. Lett. **114** (2015) 191803, DOI: 10.1103/PhysRevLett.114.191803, arXiv:1503.07589 [hep-ex].

[30] S. Glashow, *Partial Symmetries of Weak Interactions*, Nucl. Phys. **22** (1961) 579–588, DOI: 10.1016/0029-5582(61)90469-2; S. Weinberg, *A Model of Leptons*, Phys. Rev. Lett. **19** (1967) 1264–1266, DOI: 10.1103/PhysRevLett.19.1264; A. Salam, *Weak and Electromagnetic Interactions*, 8th Nobel Symposium, *Elementary Particle Theory*, ed. by N. Svaratholm, **C68-05-19**, Lerum, Sweden, 1968.

[31] G. C. Branco, L. Lavoura, and J. P. Silva, *CP Violation*, Int. Ser. Monogr. Phys. **103** (1999).

[32] I. I. Bigi and A. Sanda, *CP violation*, Camb. Monogr. Part. Phys. Nucl. Phys. Cosmol. **9** (2000).

[33] K. Olive *et al.*, *Review of Particle Physics*, Chin. Phys. **C38** (2014) 090001, DOI: 10.1088/1674-1137/38/9/090001.

[34] P. W. Higgs, *Broken Symmetries and the Masses of Gauge Bosons*, Phys. Rev. Lett. **13** (1964) 508–509, DOI: 10.1103/PhysRevLett.13.508; F. Englert and R. Brout, *Broken Symmetry and the Mass of Gauge Vector Mesons*, Phys. Rev. Lett. **13** (1964) 321–323, DOI: 10.1103/PhysRevLett.13.321.

[35] N. Cabibbo, *Unitary Symmetry and Leptonic Decays*, Phys. Rev. Lett. **10** (1963) 531–533, DOI: 10.1103/PhysRevLett.10.531.

[36] L.-L. Chau and W.-Y. Keung, *Comments on the Parametrization of the Kobayashi-Maskawa Matrix*, Phys. Rev. Lett. **53** (1984) 1802, DOI: 10.1103/PhysRevLett.53.1802.

[37] L. Wolfenstein, *Parametrization of the Kobayashi-Maskawa Matrix*, Phys. Rev. Lett. **51** (1983) 1945, DOI: 10.1103/PhysRevLett.51.1945.

[38] J. Charles *et al.*, *CP violation and the CKM matrix: Assessing the impact of the asymmetric B factories*, Eur. Phys. J. **C41** (2005) 1–131, DOI: 10.1140/epjc/s2005-02169-1, arXiv:hep-ph/0406184 [hep-ph], updated results and plots available at: http://ckmfitter.in2p3.fr.

[39] M. Bona *et al.*, *The Unitarity Triangle Fit in the Standard Model and Hadronic Parameters from Lattice QCD: A Reappraisal after the Measurements of Δm_s and $\mathcal{B}(\to \tau\nu_\tau)$*, JHEP **0610** (2006) 081, DOI: 10.1088/1126-6708/2006/10/081, arXiv:hep-ph/0606167 [hep-ph], updated results and plots available at: http://www.utfit.org.

[40] V. Weisskopf and E. P. Wigner, *Calculation of the natural brightness of spectral lines on the basis of Dirac's theory*, Z. Phys. **63** (1930) 54–73, DOI: 10.1007/BF01336768.

[41] V. Weisskopf and E. Wigner, *Over the natural line width in the radiation of the harmonius oscillator*, Z. Phys. **65** (1930) 18–29, DOI: 10.1007/BF01397406.

[42] R. Aaij *et al.*, *Measurement of the semileptonic CP asymmetry in $B^0 - \overline{B}^0$ mixing*, Phys. Rev. Lett. **114** (2015) 041601, DOI: 10.1103/PhysRevLett.114.041601, arXiv:1409.8586 [hep-ex].

[43] J. T. Wishahi, *Measurement of CP Violation in $B^0 \to J/\psi K^0_S$ Decays with the LHCb Experiment*, Ph.D. thesis, TU Dortmund University, 2013, DOI: 10.17877/DE290R-13417.

[44] R. Fleischer, *Extracting γ from $B_{s(d)} \to J/\psi K^0_S$ and $B_{d(s)} \to D^+_{d(s)} D^-_{d(s)}$*, Eur. Phys. J. **C10** (1999) 299–306, DOI: 10.1007/s100529900099, arXiv:hep-ph/9903455 [hep-ph].

[45] K. De Bruyn and R. Fleischer, *A Roadmap to Control Penguin Effects in $B^0 \to J/\psi K^0_S$ and $B^0_s \to J/\psi\phi$*, JHEP **1503** (2015) 145, DOI: 10.1007/JHEP03(2015)145, arXiv:1412.6834 [hep-ph].

[46] P. Frings, U. Nierste, and M. Wiebusch, *Penguin contributions to CP phases in $B_{d,s}$ decays to charmonium* (2015), arXiv:1503.00859 [hep-ph].

[47] I. Adachi *et al.*, *Precise measurement of the CP violation parameter $\sin 2\phi_1$ in $B^0 \to (c\overline{c})K^0$ decays*, Phys. Rev. Lett. **108** (2012) 171802, DOI: 10.1103/PhysRevLett.108.171802, arXiv:1201.4643 [hep-ex].

[48] B. Aubert *et al.*, *Measurement of Time-Dependent CP Asymmetry in $B^0 \to c\overline{c}K^{(*)0}$ Decays*, Phys. Rev. **D79** (2009) 072009, DOI: 10.1103/PhysRevD.79.072009, arXiv:0902.1708 [hep-ex].

[49] L. Evans and P. Bryant, *LHC Machine*, JINST **3** (2008), ed. by L. Evans S08001, DOI: 10.1088/1748-0221/3/08/S08001.

[50] C. Lefèvre, *The CERN accelerator complex. Complexe des accélérateurs du CERN*, 2008, https://cds.cern.ch/record/1260465/files/0812015.pdf (visited on 2015-07-21).

[51] M. Lamont, *Status of the LHC*, J. Phys. Conf. Ser. **455** (2013) 012001, DOI: 10.1088/1742-6596/455/1/012001.

[52] K. Aamodt *et al.*, *The ALICE experiment at the CERN LHC*, JINST **3** (2008) S08002, DOI: 10.1088/1748-0221/3/08/S08002.

[53] G. Aad *et al.*, *The ATLAS Experiment at the CERN Large Hadron Collider*, JINST **3** (2008) S08003, DOI: 10.1088/1748-0221/3/08/S08003.

[54] S. Chatrchyan *et al.*, *The CMS experiment at the CERN LHC*, JINST **3** (2008) S08004, DOI: 10.1088/1748-0221/3/08/S08004.

[55] G. Anelli *et al.*, *The TOTEM experiment at the CERN Large Hadron Collider*, JINST **3** (2008) S08007, DOI: 10.1088/1748-0221/3/08/S08007.

[56] O. Adriani *et al.*, *The LHCf detector at the CERN Large Hadron Collider*, JINST **3** (2008) S08006, DOI: 10.1088/1748-0221/3/08/S08006.

[57] B. Acharya *et al.*, *The Physics Programme Of The MoEDAL Experiment At The LHC*, Int. J. Mod. Phys. **A29** (2014) 1430050, DOI: 10.1142/S0217751X14300506, arXiv:1405.7662 [hep-ph].

[58] J. Alves A. Augusto *et al.*, *The LHCb Detector at the LHC*, JINST **3** (2008) S08005, DOI: 10.1088/1748-0221/3/08/S08005.

[59] J. M. Campbell, J. Huston, and W. Stirling, *Hard Interactions of Quarks and Gluons: A Primer for LHC Physics*, Rept. Prog. Phys. **70** (2007) 89, DOI: 10.1088/0034-4885/70/1/R02, arXiv:hep-ph/0611148 [hep-ph].

[60] $b\bar{b}$ *production angle plots*, http://lhcb.web.cern.ch/lhcb/speakersbureau/html/bb_ProductionAngles.html (visited on 2015-07-21).

[61] M. Chaichian and A. Fridman, *On a possibility for measuring effects of CP violation at pp colliders*, Phys. Lett. **B298** (1993) 218–223, DOI: 10.1016/0370-2693(93)91733-4.

[62] E. Norrbin and T. Sjostrand, *Production and hadronization of heavy quarks*, Eur. Phys. J. **C17** (2000) 137–161, DOI: 10.1007/s100520000460, arXiv:hep-ph/0005110 [hep-ph].

[63] E. Norrbin and R. Vogt, *Bottom production asymmetries at the LHC* (2000), arXiv:hep-ph/0003056 [hep-ph].

[64] R. Aaij *et al.*, *Performance of the LHCb Vertex Locator*, JINST **9** (2014) P09007, DOI: 10.1088/1748-0221/9/09/P09007, arXiv:1405.7808 [physics.ins-det].

[65] R. Aaij *et al.*, *Measurement of the track reconstruction efficiency at LHCb*, JINST **10**.02 (2015) P02007, DOI: 10.1088/1748-0221/10/02/P02007, arXiv:1408.1251 [hep-ex].

[66] R. Aaij *et al.*, *LHCb Detector Performance*, Int. J. Mod. Phys. **A30** (2015) 1530022, DOI: 10.1142/S0217751X15300227, arXiv:1412.6352 [hep-ex].

[67] M. Adinolfi *et al.*, *Performance of the LHCb RICH detector at the LHC*, Eur. Phys. J. **C73** (2013) 2431, DOI: 10.1140/epjc/s10052-013-2431-9, arXiv:1211.6759 [physics.ins-det].

[68] F. Archilli *et al.*, *Performance of the Muon Identification at LHCb*, JINST **8** (2013) P10020, DOI: 10.1088/1748-0221/8/10/P10020, arXiv:1306.0249 [physics.ins-det].

[69] R. Aaij *et al.*, *The LHCb Trigger and its Performance in 2011*, JINST **8** (2013) P04022, DOI: 10.1088/1748-0221/8/04/P04022, arXiv:1211.3055 [hep-ex].

[70] J. Albrecht *et al.*, *Performance of the LHCb High Level Trigger in 2012*, J. Phys. Conf. Ser. **513** (2014) 012001, DOI: 10.1088/1742-6596/513/1/012001, arXiv:1310.8544 [hep-ex].

[71] *LHCb trigger schemes*, http://lhcb.web.cern.ch/lhcb/speakersbureau/html/TriggerScheme.html (visited on 2015-07-24).

[72] M. Frank *et al.*, *Deferred High Level Trigger in LHCb: A Boost to CPU Resource Utilization*, J. Phys. Conf. Ser. **513** (2014) 012006, DOI: 10.1088/1742-6596/513/1/012006.

[73] M. Clemencic *et al.*, *Recent developments in the LHCb software framework Gaudi*, *17th International Conference on Computing in High Energy and Nuclear Physics*, ed. by J. Gruntorad, **219**, 2010 042006, DOI: 10.1088/1742-6596/219/4/042006; G. Barrand *et al.*, *GAUDI - The software architecture and framework for building LHCb data processing applications*, Comput. Phys. Commun. **140**.1-2 (2001), ed. by M. Mazzucato 92–95.

[74] R. Aaij *et al.*, *The Brunel Project*, ed. by M. Cattaneo and R. Lambert, 2015, http://lhcb-release-area.web.cern.ch/LHCb-release-area/DOC/brunel/.

[75] R. Aaij *et al.*, *The Moore Project*, ed. by G. Raven, 2015, http://lhcb-release-area.web.cern.ch/LHCb-release-area/DOC/moore/.

[76] M. Clemencic *et al.*, *The LHCb simulation application, Gauss: Design, evolution and experience*, J. Phys. Conf. Ser. **331** (2011), ed. by S. C. Lin 032023, DOI: 10.1088/1742-6596/331/3/032023; I. Belyaev *et al.*, *Handling of the generation of primary events in Gauss, the LHCb simulation framework*, J. Phys. Conf. Ser. **331** (2011), ed. by S. C. Lin 032047, DOI: 10.1088/1742-6596/331/3/032047.

[77] T. Sjostrand, S. Mrenna, and P. Z. Skands, *PYTHIA 6.4 Physics and Manual*, JHEP **0605** (2006) 026, DOI: 10.1088/1126-6708/2006/05/026, arXiv:hep-ph/0603175 [hep-ph]; T. Sjöstrand *et al.*, *An Introduction to PYTHIA 8.2*, Comput. Phys. Commun. **191** (2015) 159–177, DOI: 10.1016/j.cpc.2015.01.024, arXiv:1410.3012 [hep-ph].

[78] D. Lange, *The EvtGen particle decay simulation package*, Nucl. Instrum. Meth. **A462** (2001) 152–155, DOI: 10.1016/S0168-9002(01)00089-4.

[79] P. Golonka and Z. Was, *PHOTOS Monte Carlo: A Precision tool for QED corrections in Z and W decays*, Eur. Phys. J. **C45** (2006) 97–107, DOI: 10.1140/epjc/s2005-02396-4, arXiv:hep-ph/0506026 [hep-ph]; N. Davidson, T. Przedzinski, and Z. Was, *PHOTOS Interface in C++: Technical and Physics Documentation* (2010), arXiv:1011.0937 [hep-ph].

[80] S. Agostinelli *et al.*, *GEANT4: A Simulation toolkit*, Nucl. Instrum. Meth. **A506** (2003) 250–303, DOI: 10.1016/S0168-9002(03)01368-8; J. Allison *et al.*, *Geant4 developments and applications*, IEEE Trans. Nucl. Sci. **53** (2006) 270, DOI: 10.1109/TNS.2006.869826.

[81] R. Aaij *et al.*, *The Boole Project*, ed. by M. Cattaneo, 2015, http://lhcb-release-area.web.cern.ch/LHCb-release-area/DOC/boole/.

[82] R. Aaij *et al.*, *The DaVinci Project*, ed. by E. Rodrigues, 2015, http://lhcb-release-area.web.cern.ch/LHCb-release-area/DOC/davinci/.

[83] *Delivered/recorded LHCb luminosities in Run I*, http://lhcb-operationsplots.web.cern.ch/lhcb-operationsplots/index.htm (visited on 2015-07-21).

[84] R. Aaij *et al.*, *Opposite-side flavour tagging of B mesons at the LHCb experiment*, Eur. Phys. J. **C72** (2012) 2022, DOI: 10.1140/epjc/s10052-012-2022-1, arXiv:1202.4979 [hep-ex].

[85] R. Aaij *et al.*, *Performance of the LHCb B flavour tagging in Run I* (2015), in preparation.

[86] M. Needham, *Clone track identification using the Kullback-Liebler distance* (2008), http://cds.cern.ch/record/1082460.

[87] M. Grabalosa, *Flavour Tagging developments within the LHCb experiment*, Ph.D. thesis, Universitat de Barcelona, 2012.

[88] R. Aaij *et al.*, *Neural-network-based kaon tagging: development of new same side and opposite side tagging algorithms* (2015), in preparation.

[89] M. Pivk and F. R. Le Diberder, *SPlot: A Statistical tool to unfold data distributions*, Nucl. Instrum. Meth. **A555** (2005) 356–369, DOI: 10.1016/j.nima.2005.08.106, arXiv:physics/0402083 [physics.data-an].

[90] R. Aaij *et al.*, *Measurement of the $B^0 - \overline{B}^0$ oscillation frequency Δm_d with the decays $B^0 \to D^- \pi^+$ and $B^0 \to J/\psi K^{*0}$*, Phys. Lett. **B719** (2013) 318–325, DOI: 10.1016/j.physletb.2013.01.019, arXiv:1210.6750 [hep-ex].

[91] D. Martínez Santos and F. Dupertuis, *Mass distributions marginalized over per-event errors*, Nucl. Instrum. Meth. **A764** (2014) 150–155, DOI: 10.1016/j.nima.2014.06.081, arXiv:1312.5000 [hep-ex].

[92] M. Oreglia, *A Study of the Reactions $\psi' \to \gamma\gamma\psi$*, Ph.D. thesis, Stanford University, 1980; J. Gaiser, *Charmonium Spectroscopy From Radiative Decays of the J/ψ and ψ'*, Ph.D. thesis, Stanford University, 1982; T. Skwarnicki, *A study of the radiative CASCADE transitions between the Upsilon-Prime and Upsilon resonances*, Ph.D. thesis, Cracow, INP, 1986.

[93] R. Aaij *et al.*, *B flavour tagging using charm decays at the LHCb experiment*, JINST **10**.10 (2015) P10005, DOI: 10.1088/1748-0221/10/10/P10005, arXiv:1507.07892 [hep-ex].

[94] W. D. Hulsbergen, *Decay chain fitting with a Kalman filter*, Nucl. Instrum. Meth. **A552** (2005) 566–575, DOI: 10.1016/j.nima.2005.06.078, arXiv:physics/0503191 [physics].

[95] P. Koppenburg, *Dealing with Multiple Candidates*, LHCb-INT-2011-009, 2011, https://cds.cern.ch/record/1340942, internal note.

[96] T. M. Karbach, G. Raven, and M. Schiller, *Decay time integrals in neutral meson mixing and their efficient evaluation* (2014), arXiv:1407.0748 [physics.data-an].

[97] W. Verkerke and D. P. Kirkby, *The RooFit toolkit for data modeling*, *Statistical problems in particle physics, astrophysics and cosmology*, ed. by L. Lyons and M. Karagoz, 2006 310, arXiv:physics/0306116 [physics].

[98] I. Antcheva *et al.*, *ROOT: A C++ framework for petabyte data storage, statistical analysis and visualization*, Comput. Phys. Commun. **182** (2011) 1384–1385, DOI: 10.1016/j.cpc.2011.02.008.

[99] O. Behnke *et al.*, *Data analysis in high energy physics*, ed. by O. Behnke, 2013, ISBN: 978-3-527-41058-3.

[100] J. Wishahi *et al.*, *cptoymc: A generator of pseudo-datasets of decays with time-dependent CP violation*, version 0.0, 2015, DOI: 10.5281/zenodo.20356.

[101] R. Aaij *et al.*, *Measurement of the $\overline{B}^0 - B^0$ and $\overline{B}^0_s - B^0_s$ production asymmetries in pp collisions at $\sqrt{s} = 7$ TeV*, Phys. Lett. **B739** (2014) 218–228, DOI: 10.1016/j.physletb.2014.10.005, arXiv:1408.0275 [hep-ex].

[102] W. Fetscher *et al.*, *Regeneration of arbitrary coherent neutral kaon states: A new method for measuring the $K^0 - \overline{K}^0$ forward scattering amplitude*, Z. Phys. **C72** (1996) 543–547, DOI: 10.1007/s002880050277; B. Ko *et al.*, *Effect of nuclear interactions of neutral kaons on CP asymmetry measurements*, Phys. Rev. **D84** (2011) 111501, DOI: 10.1103/PhysRevD.84.111501, arXiv:1006.1938 [hep-ex].

[103] R. Aaij *et al.*, *Measurement of CP asymmetry in $D^0 \to K^-K^+$ and $D^0 \to \pi^-\pi^+$ decays*, JHEP **1407** (2014) 041, DOI: 10.1007/JHEP07(2014)041, arXiv:1405.2797 [hep-ex].

[104] R. Barlow, *Systematic errors: Facts and fictions* (2002) 134–144, arXiv:hep-ex/0207026 [hep-ex].

[105] A. Mödden, *Sensitivitätsstudien für die Messung von sin(2β) im Zerfallskanal $B^0 \to J/\psi K^0_S$ am LHCb Experiment*, B.Sc. thesis, TU Dortmund University, 2015.

[106] R. Niet, Personal communication, 2015.

[107] V. Müller, *Messung der zeitabhängigen CP-Asymmetrie im Zerfall $B^0 \to \psi(2S)K^0_S$ mit dem LHCb Experiment*, M.Sc. thesis, TU Dortmund University, 2014.

[108] T. Aushev *et al.*, *Physics at Super B Factory* (2010), arXiv:1002.5012 [hep-ex].

[109] R. Aaij *et al.*, *Framework TDR for the LHCb Upgrade: Technical Design Report* (2012), http://cds.cern.ch/record/1443882.

[110] R. Aaij *et al.*, *LHCb VELO Upgrade Technical Design Report* (2013), http://cds.cern.ch/record/1624070.

[111] R. Aaij *et al.*, *LHCb Tracker Upgrade Technical Design Report* (2014), http://cds.cern.ch/record/1647400.

[112] R. Aaij *et al.*, *LHCb PID Upgrade Technical Design Report* (2013), http://cds.cern.ch/record/1624074.

[113] *LHCb Trigger and Online Upgrade Technical Design Report* (2014), http://cds.cern.ch/record/1701361.

Danksagung

Lieber Bernhard Spaan, ich möchte mich bei Ihnen nicht nur für Ihr in mich gesetztes Vertrauen und Ihre Unterstützung bedanken, sondern auch für die einmalige Gelegenheit in einem internationalen Umfeld mit vielen interessanten Menschen zu forschen und zu lernen.

Lieber Herr Kröninger, lieber Herr Kierfeld, lieber Johannes, vielen Dank für die Begutachtung meiner Arbeit und dass Sie sich die Zeit genommen haben meiner Prüfungskommission beizusitzen.

Lieber Joachim Stolze, es ist Ihnen vielleicht nicht so bewusst wie mir, aber Sie haben einen nicht unerheblichen Anteil am Gelingen dieser Arbeit getragen, dafür vielen Dank.

Lieber Julian, lieber Frank, vielen vielen Dank für eure Unterstützung und Zusammenarbeit, die diese Arbeit erst möglich gemacht haben. Ein großes Dankeschön auch an dich Florian, niemand anderes musste so oft herhalten und sich um meine Compiler-Probleme kümmern wie du.

I would also like to send a big thank you to the LHCb Flavour Tagging group, in particular to Alex, Tobi, Mirco, Uli, Julian and Stefania, for your great collaboration and a very enjoyable working environment.

Ich möchte mich ganz ausdrücklich bei meinen alten und neuen Bürokollegen Julian, Florian, Ramon, Tobi und Max bedanken: Das gemeinsame Arbeiten und Pausieren hat mir viel Spaß gemacht und mich immer wieder aufs Neue motiviert.

Ich danke der fantastischen Dortmunder Arbeitsgruppe: Johannes, Alex, Mirco, Moritz, Matthias, Kevin & Kevin, Melanie, Marion, Uli, Robert, Laura, Ayse, Nina, Florian, Juliane, Frank, Janine, Vanessa, Margarete, Max, Timon, Konstantin, Holger & Holger, Bernhard Spaan, Britta, Tobias, Klaus, Julian und allen Ehemaligen und nicht persönlich genannten! Vielen Dank euch allen, ich werde euch vermissen!

Ich möchte allen meinen Freunden danken: natürlich der Teilmenge der oben genannten Personen, aber auch denen die mich deutlich weniger zu Gesicht bekommen haben. Ich verspreche baldige Besserung!

Vielen Dank meiner Familie, meinen Eltern und meinem Bruder, ihr habt mich – auch wenn Vieles für euch schleierhaft blieb – immer unterstützt und nur selten nachgefragt, ob aus dem Jungen noch was Ordentliches wird.

Danke Eva für deinen Rückhalt, dein Verständnis für lange Arbeitstage und entgangene Wochenenden, deine stetige Motivation, dafür, dass du mich aufgefangen hast, wenn es schwierig wurde und dich mit mir über die Erfolge gefreut hast. Danke, dass du immer an meiner Seite bist!